

The Development of Reflection Anisotropy Spectroscopy Instrumentation for the study of dynamic surface properties

A thesis submitted in accordance with the requirements of the
University of Liverpool for the degree of Doctor in Philosophy

Paul Harrison



U N I V E R S I T Y O F
L I V E R P O O L

Department of Physics
University of Liverpool
UK

February 2019

The Development of Reflection Anisotropy Spectroscopy
Instrumentation for the study of dynamic surface properties
by Paul Harrison.

Abstract

This thesis develops a detailed analysis of the Reflection Anisotropy Spectroscopy (RAS) technique and provides a clear understanding of how the complex RAS output relates to the anisotropic reflectivity of the sample. A full analysis of the output of the instrument is carried out for any sample orientation that goes beyond the standard procedure of fixing the orientation of the sample. This analysis enables the understanding of how the instrument outputs relate to sample properties.

The theoretical analysis of the output of the RAS instrument is complemented by the development of a simulation program in which the optical and electronic components are individually modelled. This makes it possible to predict the output of the instrument as the components are configured in a number of different ways and makes it possible to check for mistakes in the extensive algebra required by the analytical treatment.

In order to understand the output obtained by rotating the sample, a novel means of displaying the data is presented. This demonstrates that an assumption that is implicit in the usual analysis of the output of the standard RAS instrument needs careful consideration.

The second half of the thesis deals with the development of a fast RAS instrument. The need for a fast instrument arose when studying fast reactions following step potential changes in an electrochemical cell. This has potential applications in the study of protein conformational change. In all, three generations of the design of fast RAS instruments were built, which could form the basis of a commercial instrument.

Contents

Abstract	2
Contents	3
Acknowledgments	8
List of abbreviations	9
Chapter 1: Introduction	10
1.1 Introduction	11
1.2 Thesis Aims	15
1.3 Thesis Structure	15
1.3.1 Chapter 2: RAS instrumentation	15
1.3.2 Chapter 3: RAS theory, instrumentation and analysis	16
1.3.3 Chapter 4: Simulation of PEM-based RAS instrument	16
1.3.4 Chapter 5: Displaying ADRAS data	16
1.3.5 Chapter 6: Development of a fast RAS instrument	16
1.3.6 Chapter 7: Improved 32 channel fast RAS version 3	16
1.3.7 Chapter 8: Conclusion and further developments	17
Chapter 2: RAS instrumentation	18
2.1 Introduction	19
2.2 Rotating-sample RAS	19
2.2.1 Principle of operation	19
2.3 PEM-based RAS	21
2.3.1 Photo-elastic modulator (PEM)	21
2.3.2 Description of the PEM-based RAS instrument	23
2.3.3 Interpreting the output of the PEM-based RAS instrument	25
2.4 Optical components of a RAS instrument	26
2.4.1 Lamp	26
2.4.2 Polariser	27
2.4.3 Sample	28
2.4.4 PEM optical head	28
2.4.5 Analyser	28
2.4.6 Monochromator	28
2.4.7 Detector	29
2.5 Electronic components of a RAS instrument	29

2.5.1 PEM control unit	29
2.5.2 Monochromator control unit	30
2.5.3 Detector readout and control	30
2.5.4 Lock-in amplifier.	30
2.5.5 Analogue to digital converter (ADC).	31
2.5.6 Digital-to-analog converter (DAC).	31
2.5.7 Personal computer.	31
Chapter 3: RAS theory, instrumentation and analysis	32
3.1 Introduction	33
3.2 Light penetration into a solid	33
3.3 RAS definition and analysis	35
3.3.1 Applying approximations	38
3.4 Instrumentation analysis	41
3.4.1 Rotating-sample RAS (non PEM)	41
3.4.2 PEM-based RAS instrument analysis (with rotating-sample)	42
3.4.3 Using Jones matrix formalisation	43
3.4.4 Detector output	46
3.4.5 Detector output as function of PEM frequency ω	46
3.4.6 Jacobi–Anger expansion	47
3.4.7 Linking experimental measurable quantities, to sample anisotropy	48
3.5 Reflection in terms of complex refractive index	52
3.6 Sample rotation angle	53
3.7 Exploiting sample rotation	55
3.8 Determining optimum retardation	55
Chapter 4: Simulation of PEM-based RAS instrumen	57
4.1 Simulation of PEM-based RAS instrument	58
4.1.1 Simulation using Jones matrix formalisation	58
4.1.2 Simulation of multiple stage system	60
4.1.3 Simulation over one PEM cycle	61
4.1.4 Simulation of lock-in amplifier	62
4.1.5 Basic overall code for a single rotation of the sample	64
4.2 Checking simulation against analytical expression	66
4.3 Detector output as function of sample properties for $\theta = 0.25 \pi$ rad	68
4.3.1 Case 1: $\varphi_1 = \varphi_2, r_1 \neq r_2 $	69
4.3.2 Case 2: $\varphi_1 \neq \varphi_2, r_1 = r_2 = 1$	71
4.3.3 Case 3: $\varphi_1 \neq \varphi_2, r_1 \neq r_2 $	73

4.4 Re($\Delta r/r$) and Im($\Delta r/r$) compared to simulated RAS1 and RAS2	73
4.4.1 Re($\Delta r/r$) compared to simulated RAS2 from RAS instrument	73
4.4.2 Im($\Delta r/r$) compared to simulated RAS1 from RAS instrument	75
4.5 Detector output as function of rotating sample	76
4.5.1 RAS instrument rotation waveform component I_{DC}	77
4.5.2 RAS instrument rotation waveform component	78
4.5.3 RAS instrument rotation waveform components	80
4.5.4 RAS instrument ADRAS simulation	80
4.6 Conclusion	84
 Chapter 5: Displaying ADRAS data	 86
5.1 Displaying ADRAS data	87
5.1.1 Argand-type diagram	89
5.2 ADRAS of Ag(110)	90
5.2.1 Surface plots of Ag(110) ADRAS data	93
5.2.2 Ag(110) rotation data as a locus on an Argand-type diagram	94
5.2.3 Ag(110) aligning phase with sample anisotropy	96
5.2.4 Plotting ADRAS2 spectrum of Ag(110) as orthogonal components	97
5.3 Summary of Ag(110) ADRAS results	98
5.4 ADRAS of Au(110)	99
5.4.1 Au(110) rotation data as a locus on an Argand-type diagram	100
5.4.2 Plotting ADRAS2 spectrum of Au(110) as orthogonal components	103
5.5 Summary of Au(110) (1×1, (1×2) and (1×3) ADRAS2 results	107
5.6 Conclusion	108
 Chapter 6: Development of a fast RAS instrument	 109
6.1 Review of fast RAS instrumentation	110
6.1.1 Multiplexed single lock-in design by Núñez-Olvera <i>et al</i>	110
6.1.2 Multi-channel lock-in design by Kaspari <i>et al</i>	111
6.1.3 Rotating compensator CCD readout design by Hu <i>et al</i>	112
6.2 Liverpool 16 channel fast RAS instrument version 1 (FRASv1)	113
6.2.1 Optical description	113
6.2.2 Electronic overview	114
6.2.3 Photo diode array and pre-amplification	115
6.2.4 Noise filtering	117
6.2.5 DC (r) section	118
6.2.6 AC (Δr) section	118
6.2.7 PC interface	119

6.2.8 Timing unit (AC path)	119
6.2.9 Multiplexer	120
6.2.10 AC calibration procedure	121
6.2.11 PEM retardation	121
6.2.12 Determination of retardation over spectral range	121
6.2.13 Wavelength Calibration	124
6.2.14 Electronic test and calibration	124
6.3 Experimental use of the FRASv1 16 channel fast RAS instrument	125
6.4 FRASv2 32 channel enhanced UV upgrade	126
6.4.1 Enhanced photodiode array	126
6.4.2 Read-out electronics	127
6.5 Experimental use of the Liverpool FRASv2 32 instrument	128
6.6 Summary	129
Chapter 7: Improved 32 channel fast RAS version 3 (FRASv3)	131
7.1 Review of FRASv1 and FRASv2 instruments	132
7.2 Dynamic range	132
7.3 Synchronisation stability	134
7.3.1 Synchronisation using linear interpolation	136
7.3.2 Synchronisation using binning	137
7.4 Data acquisition	138
7.4.1 Input set-up	139
7.4.2 Sample clock configuration	140
7.4.3 Time stamping each sample clock pulse	141
7.5 Data processing	143
7.6 Noise reduction by averaging	143
7.7 Noise reduction by fitting exponentials	144
7.7.1 Equation of total fit to step change	149
7.8 Experimental application of the FRASv3 instrument	149
7.8.1 Au(110) response to potential switch from 0.3 V to 0.6 V	150
7.8.2 Au(110) response to potential switch from 0.3 V to -0.6 V	152
7.8.3 Summary of experimental application	153
Chapter 8: Conclusion and further developments	155
8.1 RAS theory, instrumentation and analysis	156
8.2 Chapter 4 Simulation of PEM-based RAS instrument	157

8.3 Displaying ADRAS data	157
8.4 Development of a Fast RAS instrument	158
8.5 Improved 32 channel fast RAS version 3 (FRASv3)	158
8.6 Combined rotation and Fast ADRAS	159
8.7 Future work - CD instrument	159
8.7.1 Calibration	160
Publications by the author	162
References	164

Acknowledgments

I would like to thank Peter Weightman, not only for the interest, guidance and support he has given me, but also for his excitement and depth of knowledge in science that I have found so inspiring. I also wish to thank David Joss and Tim Veal for their invaluable support and advice.

I would like to give special thanks to my colleague Caroline Smith who, apart from her professional expertise, can always be relied on to provide wisdom and reassurance over a cup of tea or two. Warm thanks too go to Trevor Farrell for sharing his wide knowledge, experience and interests.

It is a great pleasure to work with colleagues Steve Barrett, Michele Siggel-King and Paul Unsworth, and I thank them for their friendship, patience and support. I would also like to thank Marj Robson for her invaluable assistance.

I would like to thank present and many previous PhD students whose company and stimulating conversation have made work and study such a pleasure.

To Thomas and Ellen, of whom I am so proud, thanks for keeping my feet on the ground. Finally to my wonderful wife Janet thank you for your love, patience and constant support.

List of abbreviations

AC	Alternating Current
ADRAS	Azimuthal Dependant Reflection Anisotropy Spectroscopy
CSA	Camphorsulphonic acid
CVD	Chemical Vapour Deposition
DAC	Digital-to-analogue Converter
DC	Direct Current
DSP	Digital Signal Processor
FCC	Face Centred Cubic
FRAS	Fast Reflection Anisotropy Spectroscopy
FOR	Frame of Reference
MBE	Molecular Beam Epitaxy
MOVPE	Metalorganic Vapour Phase Epitaxy
NI	National Instruments
NRSE	Non-Referenced Single-Ended
PCB	Printed Circuit Board
PEM	Photo Elastic Modulator
PMT	Photo Multiplier Tube
PSD	Phase Sensitive Detector
RAS	Reflection Anisotropy Spectroscopy
RC	Rotating Compensator
RDS	Reflectance Difference Spectroscopy
RHEED	Reflection High Energy Electron Diffraction
UHV	Ultra High Vacuum
VI	Virtual Instrument

Chapter 1: Introduction

1.1 Introduction	11
1.2 Thesis Aims	15
1.3 Thesis Structure	15
1.3.1 Chapter 2: RAS instrumentation	15
1.3.2 Chapter 3: RAS theory, instrumentation and analysis	16
1.3.3 Chapter 4: Simulation of PEM-based RAS instrument	16
1.3.4 Chapter 5: Displaying ADRAS data	16
1.3.5 Chapter 6: Development of a fast RAS instrument	16
1.3.6 Chapter 7: Improved 32 channel fast RAS version 3	16
1.3.7 Chapter 8: Conclusion and further developments	17

1.1 Introduction

The investigation of the properties of solid surfaces in gaseous or liquid environments usually necessitates using an optical probe, as the use of free electrons to excite and/or observe surface properties require vacuum conditions. Unfortunately the development of an optical probe of surfaces has to overcome the basic problem that light penetrates significantly into the bulk of a material before being reflected. Thus the probe will sample the bulk properties rather than the surface properties. For gold this results in a $1/e$ penetration depth of approximately 16nm, or 39 lattice layers, for a wavelength of 413 nm. Hence the contribution of the surface to the reflected optical signal will be very small (2.5% in this case) compared to the signal from the bulk. This calculation is shown in chapter 3.

A number of experimental approaches have been adopted to get round this problem, such as: Raman Spectroscopy [1], Spectroscopic Ellipsometry [2] and Surface Plasmon Resonance [3]. All have been used to probe surfaces and adsorbates on surfaces.

This thesis is concerned with the technique of Reflection Anisotropy Spectroscopy (RAS) [4]. RAS is the difference in reflection (Δr) between orthogonal linearly polarised light (r_1 and r_2) normally incident on a surface plane, normalised to the mean reflectivity (r):

$$\frac{\Delta r}{r} = \frac{2(r_1 - r_2)}{r_1 + r_2} \quad (1.1)$$

A full analysis of the RAS definition is carried out in chapter 3.

RAS has the characteristic that if the sample bulk is isotropic with an anisotropic surface, then it becomes a very surface sensitive probe. This is the case with a (110) surface on a face centred cubic (FCC) material. For this reason the most common use of RAS is for measuring the difference in reflection between the $[1\bar{1}0]$ and $[001]$ directions on a (110) FCC crystal surface, typically Au. In this case it has become

convention [5] to regard the reflectivity in the $[1\bar{1}0]$ direction as r_1 in equation 1.1 and the reflectivity in the $[001]$ direction as r_2 .

Figure 1.1a shows an illustration of a FCC crystal lattice which indicates the atom locations within a unit cell, and the position of the (110) surface (shaded). Figure 1.1b shows a cut-away unit cell which demonstrates that each unit cell contains 4 atoms. The 3 dimensional 90 degree rotational symmetry ensures that the bulk exhibits no optical anisotropy, however this is not true of the $\langle 110 \rangle$ surfaces. This is illustrated in figures 1.2a - 1.2f, which show the (110)-(1×1) surface, the (110)-(1×2) surface reconstruction and the (110)-(1×3) surface reconstruction. Each type of surface is illustrated with the (110) surface viewed from the side and from above. The views from above have a surface unit cell marked in blue, thus illustrating the surface anisotropy.

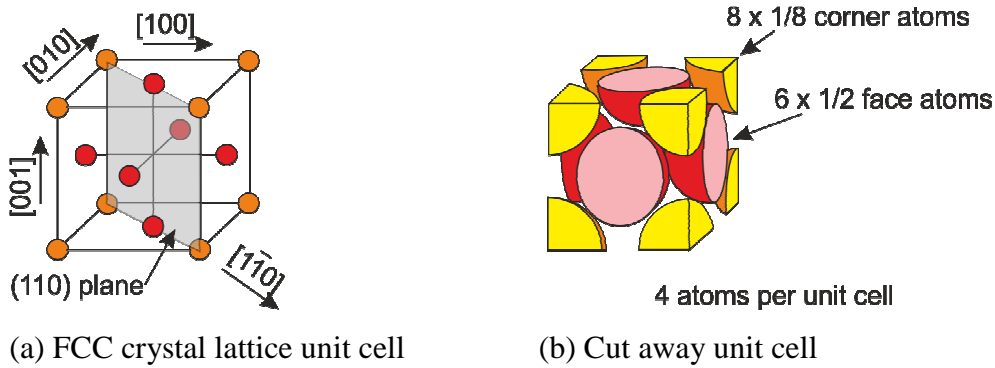


Figure 1.1 The FCC unit cell (a) showing the atom locations, the $[1\bar{1}0]$ plane and the reciprocal lattice vectors. The cut away unit cell (b) shows that each unit cell contains 4 atoms.

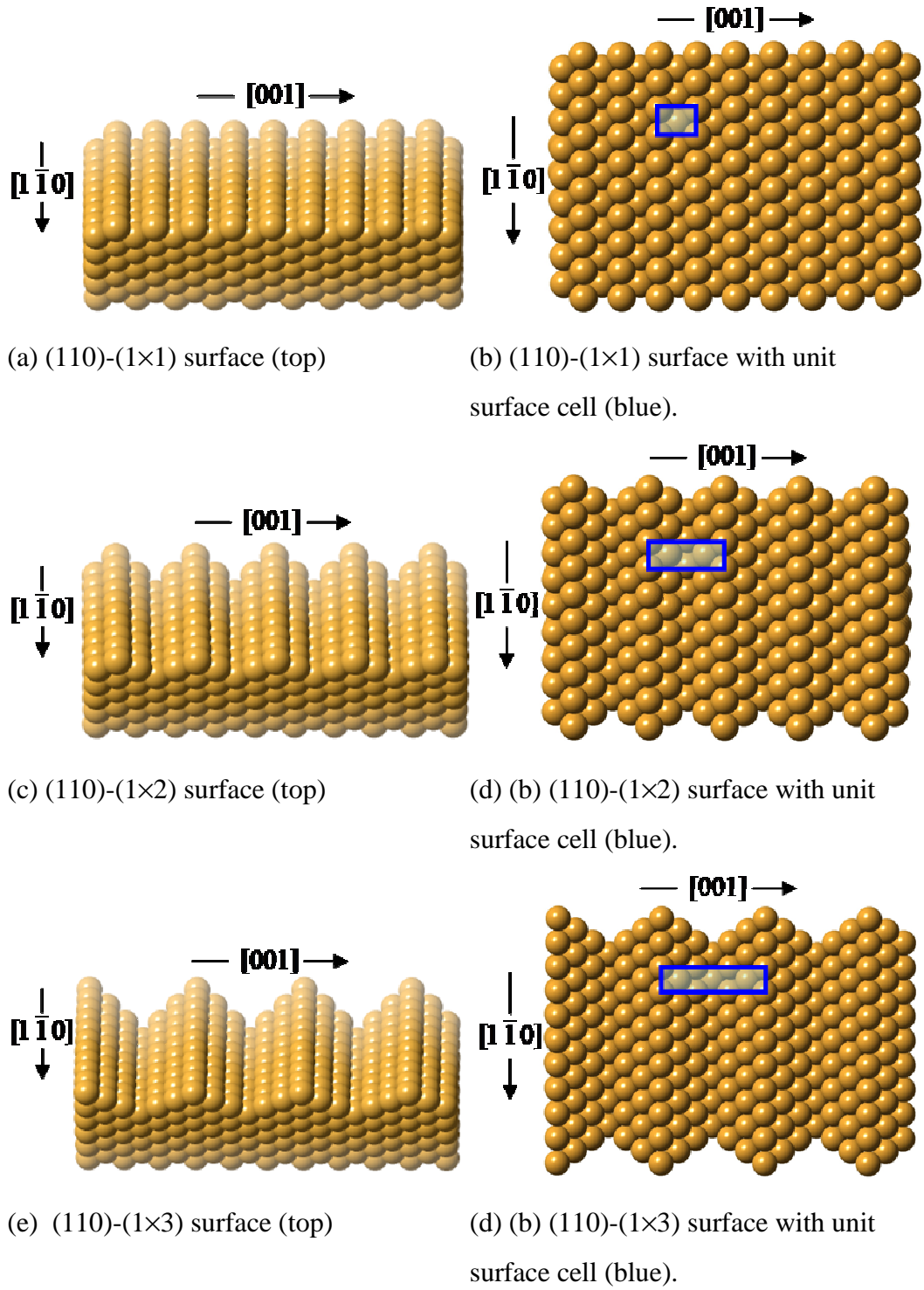


Figure 1.2 Crystal structure of an FCC crystal. (a) and (b) are the respective side view and top view of the (110)-(1×1) surface. Similarly (c) and (d) are side and top view of (110)-(1×2) reconstructed surface. (e) and (f) are side and top view of (110)-(1×3) reconstructed surface.

RAS was developed primarily by David Aspnes in the 1980s as a way of monitoring molecular beam epitaxy (MBE) semi-conductor growth in ambient conditions. It had previously been demonstrated that monitoring MBE semi-conductor growth in ultra high vacuum (UHV) using Reflection High Energy Electron Diffraction (RHEED) [6] made it possible to obtain control of semi-conductor structures on an atomic scale. However the development of metalorganic vapour phase epitaxy (MOVPE) [7] and chemical vapour deposition (CVD) [8] approaches to semi-conductor growth require a gaseous ambient environment at normal pressures and consequently it was not possible to monitor and control the growth process using RHEED. This was the problem that Aspnes was seeking to overcome by developing RAS.

The ability for RAS to operate in solution (provided it is not opaque) enables it to be used in electro-analytical experiments [9], [10], [11], [5], . Potentials applied in electrochemical cells can stimulate surface reconstruction and prompt the movement of adsorbate molecules on the sample electrode surface. RAS can non-invasively monitor the dynamics of this activity.

The substrate most often used for in-solution RAS experiments is Au(110) because it is inert and easy to prepare with clean surfaces by flame annealing [12], [13]. Understanding the behaviour of Au(110) thus becomes important in order to distinguish it from the adsorbate signal. Unfortunately when studying adsorbates on Au(110) in an electrochemical cell, the Au(110) surface is likely to change with the applied potential [9], this will both directly affect the RAS as well disturb the adsorbates under investigation.

This thesis will report advances in the development of RAS instrumentation and studies of dipole orientation and dynamic surface properties. The use of Au(110) as a substrate in RAS electrochemical experiments, makes it important to understand the behaviour of the Au(110) surface under dynamic electrochemical conditions. With the ability to orientate biological molecules onto surfaces the hope would be that this work could provide a basis for instrumentation that could obtain useful information in such areas as protein conformational change [14], [15], [16], [17], [18], [19].

RAS detects anisotropy by utilising polarised light. The amplitude and polarisation of light reflected from an anisotropic sample will depend on both the incident polarisation state of the light and the orientation of the sample. RAS instruments determine the sample anisotropy by observing this change in amplitude and polarisation. If the polarisation or sample orientation is modulated, the anisotropy also gives rise to a modulation of the reflected light signal. Low-noise techniques, such as lock-in amplifiers, allow RAS to be very sensitive, typically capable of measuring surface anisotropies to 1 part in 10^5 [4].

In this thesis RAS is referred to as Reflection Anisotropy Spectroscopy. RAS is also known as Reflectance Anisotropy Spectroscopy [20], and Reflectance Difference Spectroscopy (RDS) [21]. Reflectance is a measure of the total power (or flux) reflected divided by the total incident power [22] and as such is a scalar quantity that is equal to the square of the magnitude of the complex Fresnel coefficient [2]. As RAS is a complex quantity, in this thesis RAS is always assumed to refer to *Reflection* Anisotropy Spectroscopy.

1.2 Thesis Aims

To improve the understanding of the RAS technique and provide a comprehensive analysis of the instrument to better realise its potentials and limitations.

To study azimuthal dependant RAS (ADRAS), particularly for identifying dipole orientation.

To improve the speed of RAS instrumentation, in order to follow dynamic surface actions.

1.3 Thesis Structure

1.3.1 Chapter 2: RAS instrumentation

This chapter reviews the development of the RAS technique and outlines the principle of operation. Typical components are explained that comprise a standard RAS instrument.

1.3.2 Chapter 3: RAS theory, instrumentation and analysis

This chapter analyses in detail the RAS definition before describing a mathematical model of an ideal Aspnes RAS instrument. This is an extension of the model used previously in that it expresses the output as a function which includes sample orientation as an argument.

1.3.3 Chapter 4: Simulation of PEM-based RAS instrument

This chapter complementing chapter 3 by modelling the RAS instrument using a computer simulation. The simulation is carried out by breaking down the instrument into small units or modules for which each has an output that can be easily defined as a function of its inputs. By linking these modules together a complex system can be simulated which does not have the approximations and limitations typical of a mathematical analysis.

The simulation is used to check the analysis in chapter 3 and to explore how the output of the RAS instrument varies with sample properties and orientation.

1.3.4 Chapter 5: Displaying ADRAS data

Using the ADRAS technique generates a lot of data which is difficult to understand when displayed as a series of overlaid spectra and/or a series of overlaid temporal profiles. This chapter seeks to present the ADRAS data in a way that better displays the features of the sample under investigation, particularly dipole orientation.

1.3.5 Chapter 6: Development of a fast RAS instrument

This chapter reviews fast RAS instrumentation and introduces a design based on the use of a 16 channel photodiode array. The design is improved by incorporating a 32 channel photodiode. Examples of published experiments carried out by both the 16 channel and the 32 channel versions are given.

1.3.6 Chapter 7: Improved 32 channel fast RAS version 3

This chapter shows the development of the fast RAS from version 2 in chapter 6 to version 3. The optics, photodiode array and pre-amplifier front end electronics are kept from version 2 but the data digitisation and acquisition is radically changed. Noise reduction of transient signals is studied by using the fitting of a series of

exponentials. Dynamic experimental use of the instrument from published and unpublished data is given as an example of its use.

1.3.7 Chapter 8: Conclusion and further developments

This summarises each chapter and discusses current and possible further developments on, or based on, RAS instrumentation.

Chapter 2: RAS instrumentation

2.1 Introduction	19
2.2 Rotating-sample RAS	19
2.2.1 Principle of operation	19
2.3 PEM-based RAS	21
2.3.1 Photo-elastic modulator (PEM)	21
2.3.2 Description of the PEM-based RAS instrument	23
2.3.3 Interpreting the output of the PEM-based RAS instrument	25
2.4 Optical components of a RAS instrument	26
2.4.1 Lamp	26
2.4.2 Polariser	27
2.4.3 Sample	28
2.4.4 PEM optical head	28
2.4.5 Analyser	28
2.4.6 Monochromator	28
2.4.7 Detector	29
2.5 Electronic components of a RAS instrument	29
2.5.1 PEM control unit	29
2.5.2 Monochromator control unit	30
2.5.3 Detector readout and control	30
2.5.4 Lock-in amplifier.	30
2.5.5 Analogue to digital converter (ADC).	31
2.5.6 Digital-to-analog converter (DAC).	31
2.5.7 Personal computer.	31

2.1 Introduction

This chapter deals with the Reflection Anisotropy Spectroscopy (RAS) instruments developed by Aspnes, the rotating-sample RAS instrument [23] and the photo-elastic modulator (PEM) based RAS instrument [24]. Both instruments are dealt with respectively in section 2.4 and 2.5 below, where the typical optical and electronic arrangements are shown together with the component parts. A full analysis of both these instruments is given in chapter 3 but here a general description is given which includes typical basic components both optical and electronic.

2.2 Rotating-sample RAS

Initially Aspnes measured reflection difference by rotating the sample in a linearly polarised light beam [23]. This is illustrated in figure 2.1 which shows the lamp, polariser, sample and detector arrangement. Referring to figure 2.1, collimated light from the lamp is polarised and shone onto the sample surface at near normal incidence. The reflected light from the surface then passes through a monochromator, which selects a narrow wavelength band to pass onto the detector. The sample can be rotated along an axis perpendicular to its surface and centred at the point of illumination. Figure 2.2 shows an electronic system diagram in which the sample is rotated by a motor. A reference signal from the motor control is used to phase lock the lock-in amplifier. The output of the lock-in is read into a PC that is used to step the monochromator.

2.2.1 Principle of operation

The detector output is sensitive to the power level of the reflected light. As the sample is rotated, the output of the detector will vary between a maximum and a minimum value. A maximum occurs when one of the eigenvectors of the reflection anisotropy is aligned with the polarised light. A minimum occurs when the other eigenvector is aligned with the polarisation. Thus the difference in reflectance, ΔR , between these maximum and minimum values normalised to the average reflectance, R , give one measure of RAS, *i.e.*

$$\frac{\Delta R}{R} = \frac{2(P_1 - P_2)}{(P_1 + P_2)} \quad (2.1)$$

where, P_1 and P_2 represent the minimum and maximum respective signal power levels at the detector.

Thus a sample rotation configuration instrument provides only a scalar value that represents the difference in reflected light power level, between the eigenvector directions of the anisotropy, normalised to the overall reflected light energy. The practical limitations of this method involve the errors introduced by the sampled area not being at the centre of rotation and the sample plane not being aligned with the axis of rotation. For these reasons the rotating-sample RAS has been superseded by the PEM-based instrument.

It may seem that rotating the polariser, instead of the sample, would be an option, however this would involve the detector being subject to the full rotation of the polarisation. In which, case any small anisotropy in the detector would create a signal on the output.

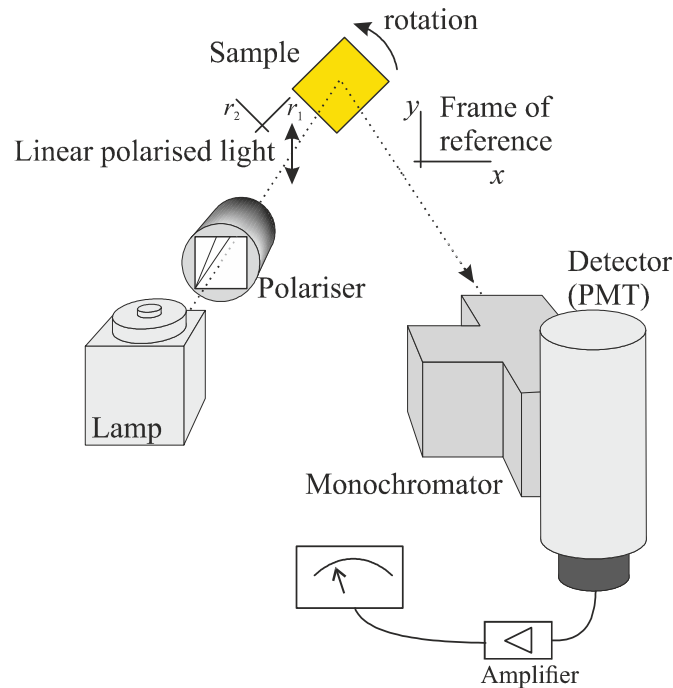


Figure 2.1 Rotating-sample RAS optical configuration. Polarised light is shone onto a rotating sample. If the sample is anisotropic the detector's output will vary as the sample is rotated.

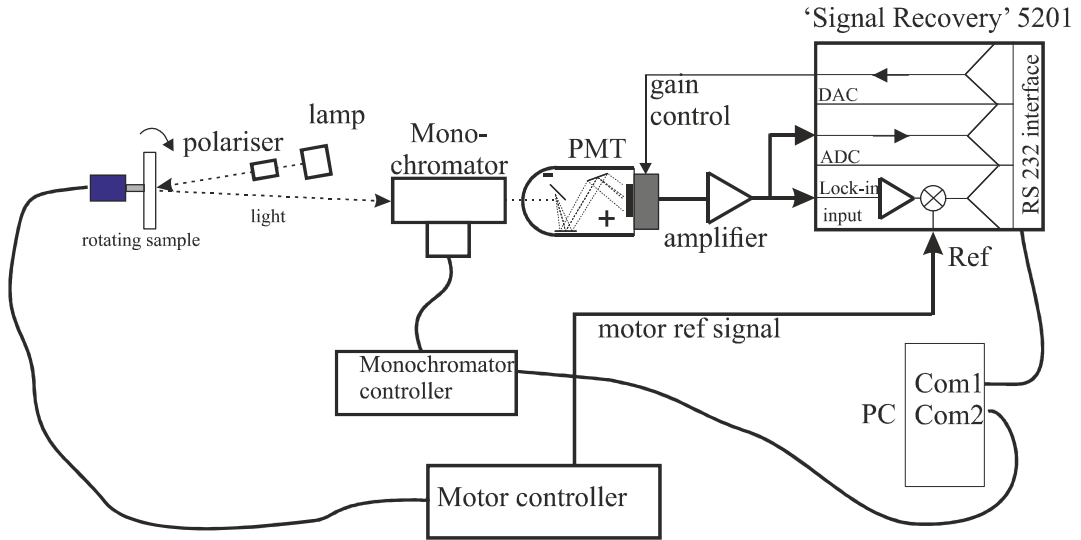


Figure 2.2 Rotating-sample RAS. Electronics system diagram.

2.3 PEM-based RAS

Later Aspnes described an improved instrument [24] based on a PEM, which has become the standard RAS instrument, the optical layout of which is illustrated in figure 2.3. The electronic system diagram is shown in figure 2.5. This design has major advantages over the rotating-sample instrument: it is faster, does not suffer from mechanically induced noise and has the ability to resolve both the real and imaginary components of the reflection anisotropy.

2.3.1 Photo-elastic modulator (PEM)

Before describing the Aspnes PEM-based RAS instrument it is useful to explain the basic principle of a PEM. In a PEM the birefringence is induced in a photoelastic material by joining it to a piezoelectric transducer. Driving the transducer from a voltage source thus creates strain in the photoelastic material, thereby inducing birefringence. Thus modulating this voltage modulates the birefringence, and hence the polarisation. This is illustrated in figure 2.4. In a birefringent material the refractive index is dependent on the polarisation state of the light. Hence light linearly polarised in a special direction would propagate at one speed but light linearly polarised in an orthogonal direction to this would propagate at another speed. These directions are termed the fast and slow axes of the birefringence. In the PEM the modulated strain causes the fast and slow axes to alternate. The propagation delay of the light between the fast and slow axes produces a phase delay which can be expressed as an angle, δ in figure 2.4, called the retardation. When expressed as a

phase angle, δ will be wavelength dependent. When driven from a sinusoidal source the retardation is expressed as:

$$\delta = A \sin \omega t \quad (2.2)$$

where A is termed the maximum retardation, ω is the angular frequency of the PEM and t is time.

Light that has components in both the fast and slow axes will experience a change in polarisation, from say linear to elliptical, as it passes through the birefringent material. Light which is linearly polarised in only the fast or slow axes will not experience a change in polarisation.

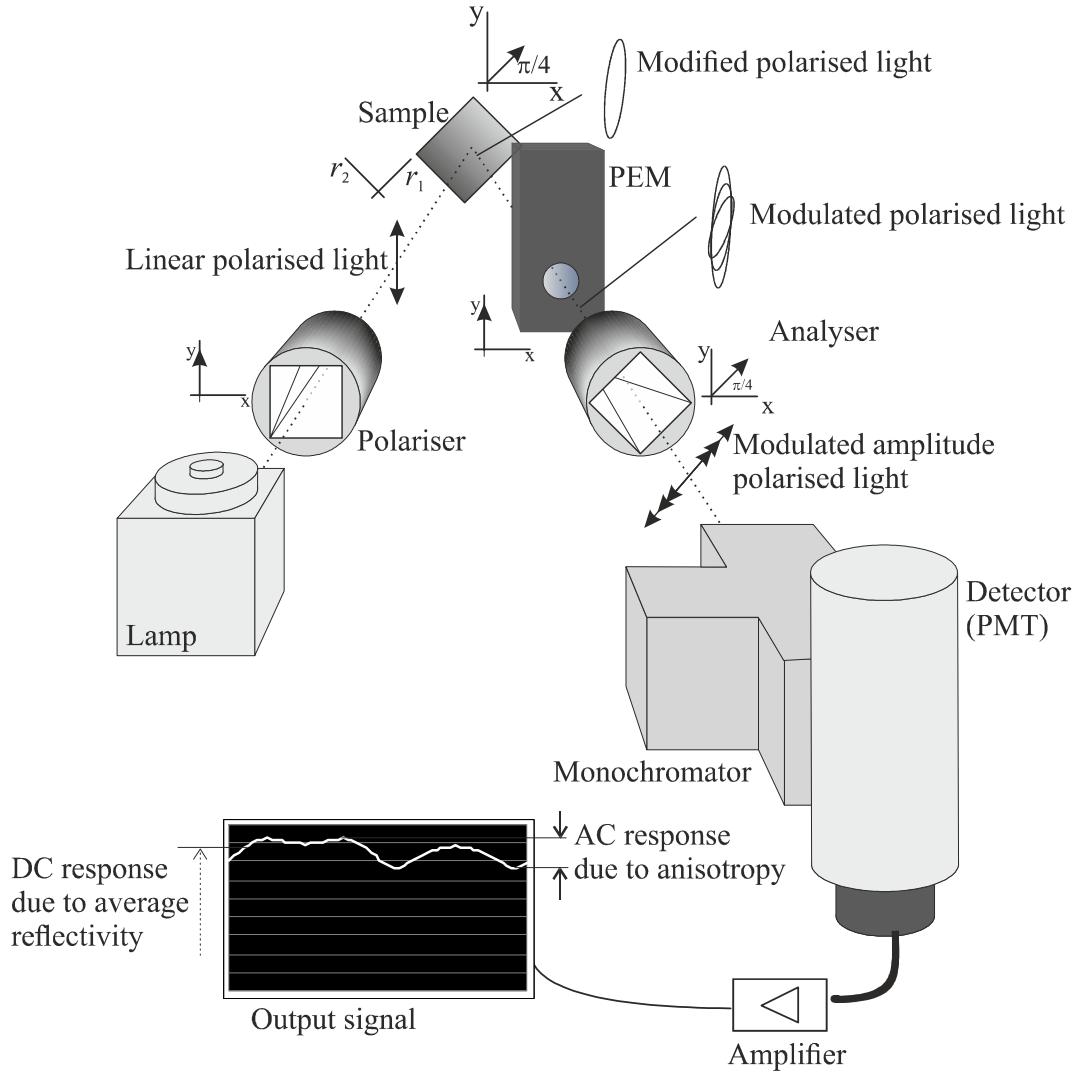


Figure 2.3 Optical layout of PEM-based RAS instrument.

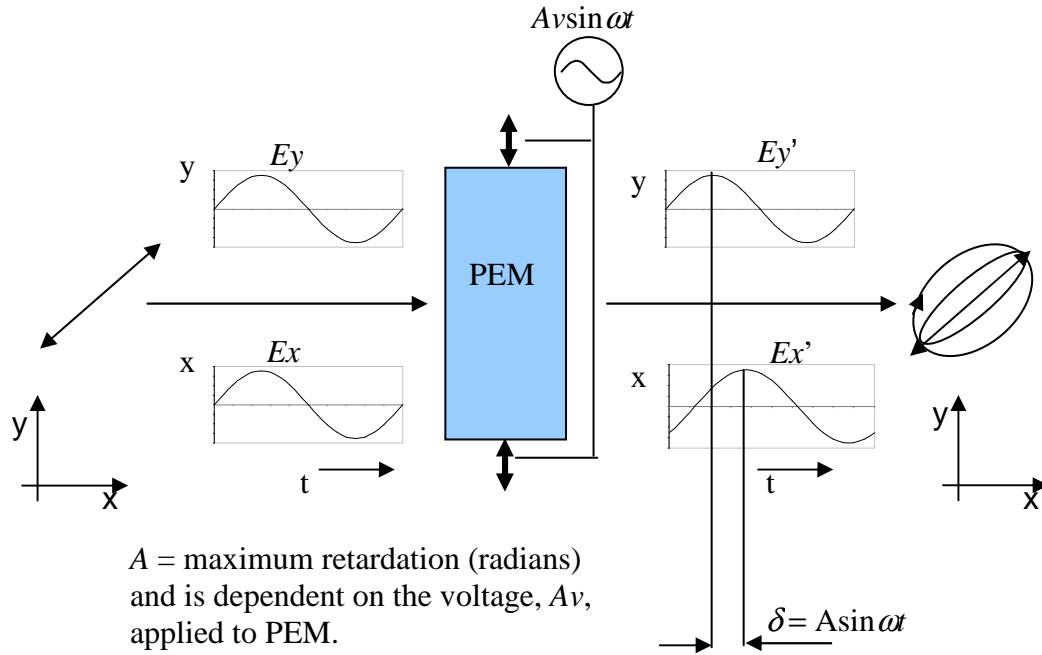


Figure 2.4 This illustrates the action of a PEM. When stressed the PEM element becomes birefringent thus changing the polarisation of the light passing through the element. Modulating the stress on the PEM element modulates the polarisation.

2.3.2 Description of the PEM-based RAS instrument

The optical layout in figure 2.3 shows the PEM is orientated so that the modulated birefringent axes are vertical and horizontal. This results in a phase change between the vertical and horizontal components of the light on exit from the PEM. Thus purely vertical or horizontal polarised light does not have its polarisation changed by the PEM. We can see from figure 2.3 that if the sample is isotropic the polarisation remains vertical and un-modulated. Only when the sample is anisotropic can the light leaving the sample have a horizontal component and thus be modulated by the PEM.

Referring again to figure 2.3, with vertical polarisation of the light incident on the sample and the sample principal axes at $\pi/4$ radians to the vertical, any anisotropy of the sample will manifest itself as a change in polarisation of the beam reflected from the sample. If we represent the optical anisotropic characteristics of the sample with Fresnel complex reflection coefficients r_1 and r_2 , then we can see how a change in

magnitude between r_1 and r_2 would result in the polarisation changing on reflection. A change in the phase angle between r_1 and r_2 would result in the polarisation becoming elliptical. A change in the real values of r_1 and r_2 would cause the polarisation to rotate and/or change in magnitude. (In figure 2.3 both phase and magnitude differences are illustrated.)

After reflecting off the sample surface the light enters the PEM. The vertical orientation of the PEM causes the eigenvectors of its optical components to act vertically and horizontally, thus the polarisation of the light will always be modulated unless it is entirely linearly polarised along one or other of these eigenvector directions. The fundamental frequency of this modulation is the PEM modulation frequency, typically 50 kHz. For an isotropic sample the light reflected from the sample remains vertically polarised and is thus not modulated by the PEM. Also in the case of an anisotropic sample which is orientated such that one of its principal axes of anisotropy is vertical, the polarisation remains vertical and so, as with the isotropic sample, the polarisation modulation, and hence the signal from the RAS instrument is zero. The angle of this orientation can be different for different wavelengths, which can give information on dipole orientations. In chapter 3 a detailed study of the PEM RAS instrument is given as a function of sample rotation angle.

After the light has passed through the PEM, an analyser is used to extract the linear component of the polarisation acting at 45 degrees, as shown in figure 2.3. Fixing the polarisation that hits the detector prevents optical anisotropy in the detector from corrupting the signal. Thus the sample anisotropy is translated into an intensity modulation at the detector.

Figure 2.5 shows a typical electronic system diagram for the PEM-based RAS instrument. The PC controls the monochromator, PEM and lock-in amplifier. The PC sets the monochromator to the current point in the spectrum, the PEM controller is set to the same wavelength, and this ensures the PEM angular retardation (denoted A in figure 2.4, and equation 2.2) remains constant over the spectrum.

Typically a photomultiplier tube (PMT) is used as the detector, with its gain control set by the PC via an auxiliary digital-to-analogue converter (DAC) output from the

lock-in amplifier instrument. The PMT gain control is set by the PC firstly reading the DC level via the ancillary analogue to digital converter (ADC) input on the lock-in amplifier. If this level is out of range then the DAC output of the lock-in amplifier is adjusted which controls the voltage applied to the PMT gain control. The AC output of the PMT is read by the main input of the lock-in amplifier which is phase locked to the PEM, via the lock-in amplifier's reference channel. For full operation of the instrument it is important to be able to detect both the 1st harmonic (fundamental) and 2nd harmonic of the output of the PMT. This can be achieved by setting the reference frequency to respectively 1× or 2× the PEM frequency. A '1F' and a '2F' output may be available on the PEM controller, for this purpose, or alternatively the lock-in amplifier may include a 2× reference option.

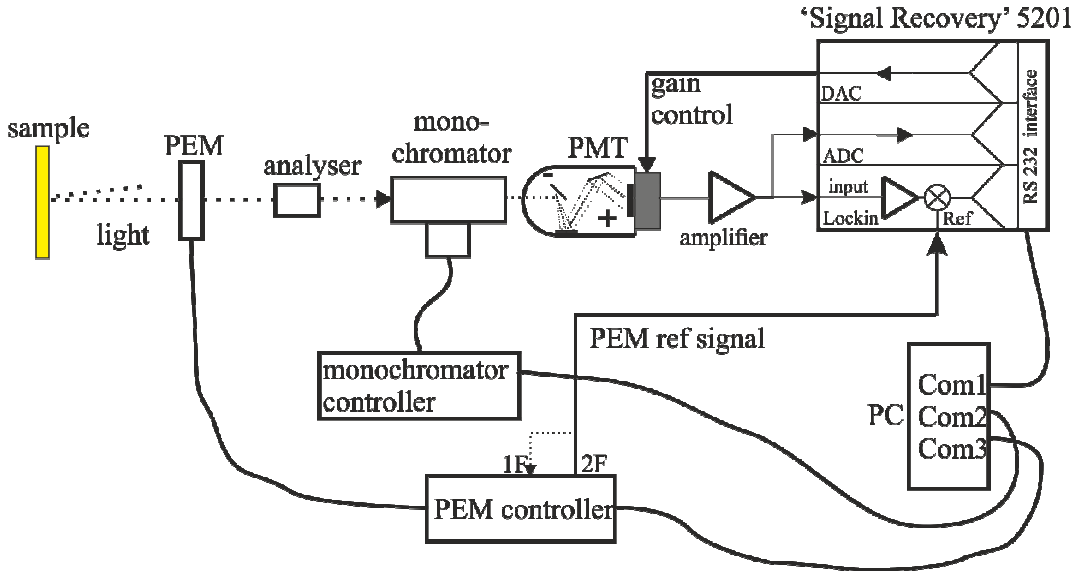


Figure 2.5 Typical electronic components of PEM-based RAS instrument

2.3.3 Interpreting the output of the PEM-based RAS instrument

Aspnes was able to determine for low sample anisotropy [18], and $\pi/4$ radian sample orientation, the time dependent expression for the detected light intensity (denoted here as $\Delta I(t)$) normalised to the mean intensity (denoted here as I_{DC}) as a function of the complex RAS signal $\Delta r/r$, shown without the window strain parameters, was:

$$\frac{\Delta I(t)}{I_{DC}} = 2J_2 \cos(2\omega t) \cdot \text{Re}\left(\frac{\Delta r}{r}\right) - 2J_1 \sin(\omega t) \cdot \text{Im}\left(\frac{\Delta r}{r}\right) \quad (2.3)$$

where J_1 , J_2 are Bessel functions of order 1 and 2 respectively and are functions of the maximum retardation, δ , of the PEM. This is explained later in sections 3.4.5 and 3.4.6.

The $\sin(\omega t)$ and $\cos(2\omega t)$ components of $\Delta I(t)$, denoted respectively, $I_{1\omega}$ $I_{2\omega}$ can be extracted separately by a phase sensitive data acquisition system, for example a lock-in amplifier (as shown above) or a Fourier transform of the captured waveform, and hence both the real and imaginary parts of the RAS signal, $\Delta r/r$, can be determined, i.e.

$$\text{Re}\left(\frac{\Delta r}{r}\right) \cong \frac{1}{2J_2} \frac{I_{2\omega}}{I_{DC}} \quad (2.4)$$

$$\text{Im}\left(\frac{\Delta r}{r}\right) \cong -\frac{1}{2J_1} \frac{I_{1\omega}}{I_{DC}} \quad (2.5)$$

[Note approximations are used as Aspnes' analysis is for low sample anisotropy]

2.4 Optical components of a RAS instrument

The typical optical components of both the rotating-sample (figure 2.1) and the PEM-based RAS (figure 2.3) are listed below.

2.4.1 Lamp

This is usually a xenon arc lamp, which has a spectral range of approximately 185 – 2000 nm (6.7 – 0.6 eV) [26]. This range will not be maintained throughout the life of the lamp and careful reference to the manufacturer's specifications should be made together with periodic monitoring of the spectral output. For use in extended UV operation a deuterium lamp with a MgF₂ window can operate over a range of 115 – 400 nm (10.8 – 3.1 eV).

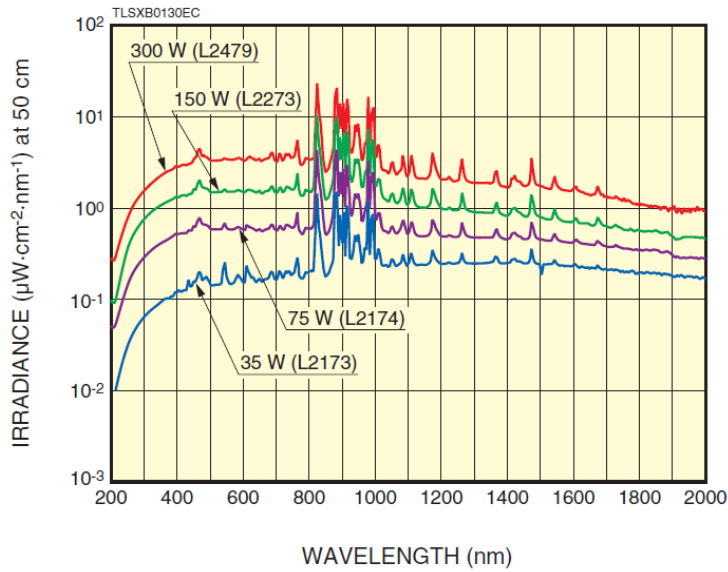


Figure 2.6 Spectral output of a Hamamatsu ‘Super-Quiet Xenon Lamp’ [26]. The 200 to 2000 nm range represents a photon energy range from approx 6.2 to 0.62 eV.

2.4.2 Polariser

Generally this is of the prism type made from a birefringent material. A range of materials can be used, depending on the operational wavelength range required, these include: alpha barium borate (a-BBO): 190-3500 nm; Calcite (CaCO_3): 350 - 2300 nm; Magnesium Fluoride MgF_2 : 130 – 4000 nm; Quartz (SiO_2): 200 - 2300 nm; and Yttrium Orthovanadate (YVO_4): 400 - 4000 nm. Figure 2.7 shows a popular range of configurations for prism polarisers, Rochon, Wollaston, Glan Thompson and Glan Taylor.

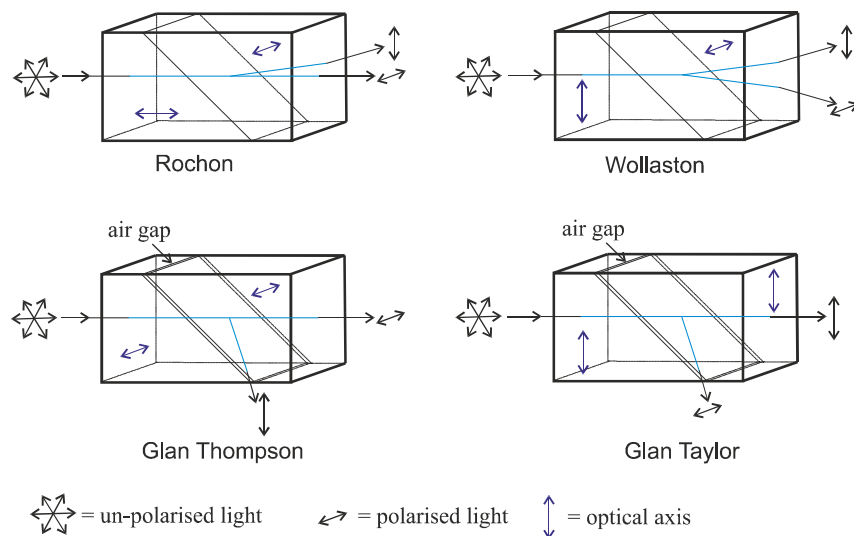


Figure 2.7 Popular types of prism polariser.

The different polariser configurations have advantages and disadvantages. Both the Glan polarisers have the advantage that they only emit one beam, but have the disadvantage of a smaller operating wavelength range. Wollaston and Rochon polarisers have a wide range, but emit both polarised beams. Wollaston has the advantage of a wider deviation than a Rochon, but a Rochon has advantage for some uses in that one of the beams is inline with the incident beam.

2.4.3 Sample

In applications where material is adsorbed onto a substrate, it is very important that the substrate is properly prepared and aligned so as to provide accurate and comparable data. Samples or substrates with bulk isotropy, such as FCC single crystal materials with a (110) surface, make the technique surface sensitive (see chapter 1 section 1.1). A Au(110) surface is often used as it is possible to obtain a clean (110) surface [27], [12].

2.4.4 PEM optical head

The PEM optical head is made from an isotropic material that becomes birefringent when mechanically stressed by a transducer. See 2.3.1 Photo-elastic modulator (PEM) above.

An example of a PEM optical head is the Hinds series I optical head for use with their PEM 100 system [28] which employs a transducer operating at 50 kHz

2.4.5 Analyser

The analyser terminates the range of the polarised region of the instrument, and makes it easier to characterise. After the analyser only the light intensity is measured, this makes the instrument less susceptible to any anisotropy in the monochromator and detector. The analyser may be similar to the polariser, although the extinction coefficient and orientation, is less demanding than that of the polariser. A more detailed analysis of the analyser is presented in chapter 3 of this thesis.

2.4.6 Monochromator

The monochromator filters the light into a variable narrow wavelength range. This is determined by the width of the entrance and exit slits. For a compact

monochromator, such as the Horiba Jobin Yvon H10 [29], that uses a grating of 1200 grooves per mm as the dispersive element, the linear dispersion is 8nm per mm of slit width. Standard slits from 0.5 to 2.0 mm give this monochromator a bandpass of 4 to 16 nm respectively.

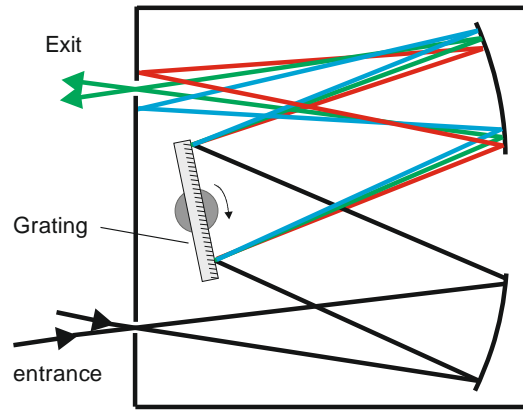


Figure 2.10 Illustration of Czerny-Turner design monochromator

2.4.7 Detector

This is typically a photomultiplier tube [30], but may also be a photo-diode or other light-sensitive device. It should have a large linear (or calibrated) dynamic range because it needs to detect the overall light intensity, as well as the modulated intensity. Modern PMTs may have a wide dynamic range of up to 8 orders of magnitude [31]. Non-linearities in either the frequency response or the amplitude response of the detector need to be calibrated out if necessary to give an accurate value of the RAS.

2.5 Electronic components of a RAS instrument

The typical electronic components of both the Rotating-sample (figure 2.2) and the PEM-based RAS (figure 2.5) are listed below.

2.5.1 PEM control unit

The maximum retardation, A in figure 2.4 of the PEM, is dependent on wavelength being studied. To maintain a constant retardation across the spectrum the stress on the PEM optical element, provided by a quartz oscillator, needs to be adjusted for the wavelength required. This adjustment is carried out by the PEM controller when a new wavelength command is issued by the PC. An example of a PEM controller is

the Hinds PEM 100 [28] for use with the Hinds series I optical head. The material for the optical element depends on the wavelength range required. Table 2.1 shows a list of common element materials [32]

Spectral Region	Series	Material
Vacuum UV, UV	I	Lithium Fluoride
Vacuum UV to mid-IR I,	II	Calcium Fluoride
Vacuum UV to near-IR	I, II	Fused Silica
Mid-visible to mid-IR	II	Zinc Selenide
Near to mid and far-IR	II	Silicon

Table 2.1 Commonly available PEM optical element materials

2.5.2 Monochromator control unit

The monochromator wavelength is set by a command to the controller from the PC. The monochromator controller tells the PC when the new wavelength is set, and data acquisition can proceed.

2.5.3 Detector readout and control

If a photomultiplier tube (PMT) is used its gain needs to be controlled to provide adequate signal, without saturation across the spectrum. This is done under PC control. In the case for photomultiplier tubes (PMT) and Si photodiode detectors, the current output from the detector is usually proportional to the input light intensity. In these cases a current-to-voltage trans-impedance amplifier is used to obtain a voltage that is proportional to the light intensity.

The detectors are required to be linear (inherently or through calibration) as both a ‘DC’ signal is present together with a small ‘AC’ modulation, both of which vary greatly over the spectrum. Thus as the RAS value is determined by the ratio of AC/DC, good linearity is required over the whole frequency range of the instrument.

2.5.4 Lock-in amplifier. This is used to measure- the ‘AC’ part of the signal. The ‘AC’ part carries the information about Δr . Depending on the amplitude, phase and noise of the signal, the lock-in amplifier needs to have correct settings for the respectively gain, reference phase and integrating time constant. An example of a lock-in amplifier is the Model 5210 from Ametek [33]

2.5.5 Analogue to digital converter (ADC). This is used to read in the 'DC' which is proportional to the mean intensity of the light reflected from the sample over a whole number of PEM cycles. A suitable ADC is often incorporated into the lock-in amplifier instrument, such as the Ametek 5210.

2.5.6 Digital-to-analog converter (DAC). This is used to control the gain of the PMT. A suitable DAC is often incorporated into the lock-in amplifier instrument, such as the Ametek 5210.

2.5.7 Personal computer. This runs software to control the above modules, collect, process, display and store data.

Chapter 3: RAS theory, instrumentation and analysis

3.1 Introduction	33
3.2 Light penetration into a solid	33
3.3 RAS definition and analysis	35
3.3.1 Applying approximations	38
3.4 Instrumentation analysis	41
3.4.1 Rotating-sample RAS (non PEM)	41
3.4.2 PEM-based RAS instrument analysis (with rotating-sample)	42
3.4.3 Using Jones matrix formalisation	43
3.4.4 Detector output	46
3.4.5 Detector output as function of PEM frequency ωt	46
3.4.6 Jacobi–Anger expansion	47
3.4.7 Linking experimental measurable quantities, to sample anisotropy	48
3.5 Reflection in terms of complex refractive index	52
3.6 Sample rotation angle	53
3.7 Exploiting sample rotation	55
3.8 Determining optimum retardation	55

3.1 Introduction

This chapter looks at the need for reflection anisotropy spectroscopy (RAS) by examining the way light penetrates into a solid, a consequence of which makes simple reflection a poor surface probe. The definition of RAS is introduced before expanding it into real and imaginary parts and applying some approximations to simplify the expressions and give insight into physical interpretations. Two types of RAS instruments developed by Aspnes are then explained, the Rotating-sample instrument [21] and the PEM-based instrument [34]. Finally the output of the PEM-based instrument is analysed as a function of the sample's azimuthal orientation, θ , the axis of which is along the light beam. The azimuthal dependent output of the RAS instrument is denoted ADRAS (azimuthal dependent reflection anisotropic spectroscopy) to distinguish it from normal RAS which is defined as a property of the sample not its orientation. Here ADRAS is defined as the output of an ideal Aspnes PEM-based RAS instrument when the sample is rotated. As with a standard RAS instrument there are two outputs, one that is derived from the fundamental frequency of the detector output and the other which is derived from the 2nd harmonic of the detector output, these are called respectively *ADRAS1* and *ADRAS2*. This is the same definition implied in previous publications [35] [36]. To summarise, RAS, as defined in equation 3.4, is independent of any measuring device, *i.e.* a RAS instrument, but ADRAS is defined as the output of a particular instrument, *i.e.* an ideal Aspnes PEM based RAS instrument.

Before examining RAS instrumentation, we look at how light is reflected from a metal and the contribution from the top surface layer. Then starting from the definition of RAS, we study in detail how this relates to the complex surface reflection coefficients of the sample. The RAS instrumentation output is also analysed with respect to the Fresnel reflection coefficients of the sample. This enables the RAS instrumentation output to be compared to the RAS definition.

3.2 Light penetration into a solid

As mentioned in the introduction, the use of light as a surface probe is seriously constrained by the penetration depth. To illustrate this, the calculation shown below shows the $1/e$ penetration depth for gold by light at a photon energy of 3 eV.

From the Beer-Lambert law [37], and referring to figure 3.1 we get:

$$I(z) = I(0)e^{-\alpha z} \quad (3.1)$$

where $I(z)$ is the light intensity at depth z , $I(0)$ is the light intensity incident at the surface and α is the absorption coefficient.

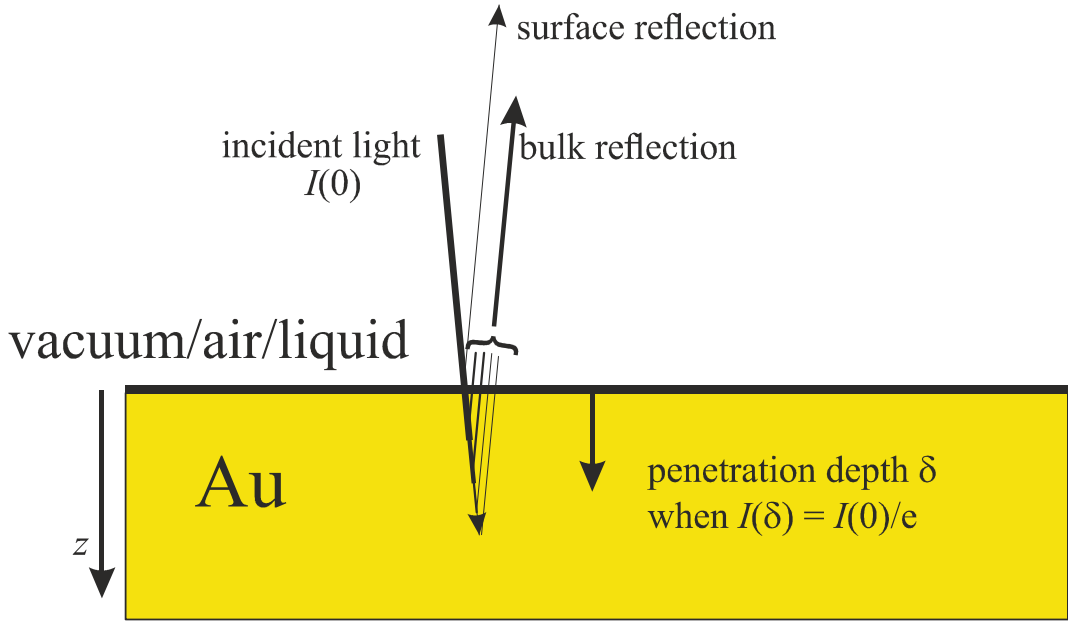


Figure 3.1 Illustration of how reflected light penetrates surface

We define penetration depth, δ , when:

$$I(\delta) = I(0)/e \quad (3.2)$$

this condition is met when $z = \delta = 1/\alpha$ in equation 3.1. The absorption coefficient, α , is related to the imaginary part of the refractive index, k , thus:

$$\alpha = \frac{4\pi k}{\lambda_0} \quad (3.3)$$

where k is the imaginary part of the refractive index and λ_0 is the wavelength in vacuum. For 3 eV radiation,

$$\lambda_0 = 413 \text{ nm}$$

For Au, at optical wavelengths, $k \sim 2$ [38]

$$\delta = \frac{\lambda_0}{4\pi k} = \left(\frac{413}{4\pi \cdot 2} \right) = 16 \text{ nm}$$

For Au (lattice constant = 0.408 nm):

$$\delta = 39 \text{ lattice units}$$

Normalising $I(0) = 1$, the absorption, I_s , due to a depth of 1 lattice unit at the surface gives:

$$I_s = 1 - I(0.408) = 1 - e^{-0.408/16} = 0.025$$

i.e. only 2.5% of light is from top lattice layer.

3.3 RAS definition and analysis

RAS is defined [4] as the difference in reflectivity, (Δr) , in orthogonal directions of a surface with normal incident plane polarised light, normalised to the overall reflectivity (r):

$$\frac{\Delta r}{r} = \frac{2(r_1 - r_2)}{r_1 + r_2} \quad (3.4)$$

where r_1 and r_2 are the complex eigenvalues of the Fresnel reflection coefficient tensor that represents the optical anisotropy of the sample surface. The eigenvectors of r_1 and r_2 , which we respectively denote v_1 and v_2 , act in orthogonal directions on

the sample surface in the physical frame of reference. RAS is thus a property of a surface not its orientation, however to measure it v_1 and v_2 must be determined. The output of the Aspnes PEM-based RAS instrument as a function of sample orientation is useful, and will be dealt with later in this chapter.

Firstly we consider the sample and the definition of RAS as a property of the sample, without regard to instrumentation or frames of reference. Representing r_1 and r_2 in rectangular form, we can define the following:

$$r_1 \equiv a + jb \quad (3.5)$$

$$r_2 \equiv c + jd \quad (3.6)$$

where a and b are the respective real and imaginary components of the complex eigenvalues of the Fresnel reflection coefficient in the v_1 direction and where $j = \sqrt{-1}$. Similarly c and d are the components in the orthogonal v_2 direction. Using definitions 3.5 and 3.6, equation 3.4 can be written as:

$$\frac{\Delta r}{r} = 2 \frac{(a - c) + j(b - d)}{(a + c) + j(b + d)} \quad (3.7)$$

Multiplying numerator and denominator by complex conjugate of denominator, ie,

$$[(a + c) + j(b + d)]^* = (a + c) - j(b + d) \quad (3.8)$$

and separating into real and imaginary parts gives:

$$\text{Re}\left(\frac{\Delta r}{r}\right) = 2 \frac{a^2 + b^2 - c^2 - d^2}{(a + c)^2 + (b + d)^2} \quad (3.9)$$

$$\text{Im}\left(\frac{\Delta r}{r}\right) = -\frac{4(ad - bc)}{(a + c)^2 + (b + d)^2} \quad (3.10)$$

we note that the denominator is the magnitude squared of the reflectivity, *i.e.*

$$rr^* = |r|^2 = (a + c)^2 + (b + d)^2 \quad (3.11)$$

We see from equations 3.5 and 3.6 that in the numerator of equation 3.9 we have $|r_1|^2 - |r_2|^2$ and that in the denominator of both equations 3.9 and 3.10 are the magnitude of the vector sum of r_1 and r_2 squared, *i.e.*

$$a^2 + b^2 - c^2 - d^2 = |r_1|^2 - |r_2|^2 \quad (3.12)$$

&

$$(a + c)^2 + (b + d)^2 = |r_1 + r_2|^2 \quad (3.13)$$

by using equations 3.12 and 3.13, equations 3.9 and 3.10 can be rewritten:

$$\operatorname{Re}\left(\frac{\Delta r}{r}\right) = 2 \frac{|r_1|^2 - |r_2|^2}{|r_1 + r_2|^2} \quad (3.14)$$

&

$$\operatorname{Im}\left(\frac{\Delta r}{r}\right) = -\frac{4(ad - bc)}{|r_1 + r_2|^2} \quad (3.15)$$

Equation 3.15 for $\operatorname{Im}(\Delta r/r)$ can be further simplified in what follows. Figure 3.2 shows the Fresnel reflection coefficient eigenvalues, r_1 and r_2 , of an anisotropic surface and illustrates parameters φ_1 , φ_2 , φ_Δ and $|\Delta r|$. Where φ_1 and φ_2 are the respective complex arguments of r_1 and r_2 ,

$$\varphi_\Delta = \varphi_2 - \varphi_1 \quad (3.16)$$

and

$$\Delta r = [(a - c) + j(b - d)] \quad (3.17)$$

$$|\Delta r|^2 = (a - c)^2 + (b - d)^2 \quad (3.18)$$

Referring to figure 3.2 a , b , c & d can be expressed as:

$$a = |r_1| \cos \varphi_1 \quad (3.19)$$

$$b = |r_1| \sin \varphi_1 \quad (3.20)$$

$$c = |r_2| \cos \varphi_2 \quad (3.21)$$

$$d = |r_2| \sin \varphi_2 \quad (3.22)$$

Using equations 3.19 to 3.22 $ad-bc$ becomes:

$$\begin{aligned} ad - bc &= |r_1| \sin(\varphi_1) |r_2| \cos(\varphi_2) - |r_1| \cos(\varphi_1) |r_2| \sin(\varphi_2) \\ &= |r_1| |r_2| \sin(\varphi_1 - \varphi_2) \\ &= |r_1| |r_2| \sin(\varphi_\Delta) \end{aligned} \quad (3.23)$$

Hence equation 3.15 can be written as:

$$\text{Im}\left(\frac{\Delta r}{r}\right) = -4 \frac{|r_1| |r_2| \sin(\varphi_\Delta)}{|r_1 + r_2|^2} \quad (3.24)$$

3.3.1 Applying approximations

Equations 3.14, 3.24 are *exact* solutions for $\text{Re}(\Delta r/r)$ and $\text{Im}(\Delta r/r)$, however, further simplification can be achieved if, as in many cases, the anisotropy is low, hence:

$$a \cong c \quad (3.25)$$

&

$$b \cong d \quad (3.26)$$

The validity and range of these approximations in equations 3.25 and 3.36 will be tested in chapter section 4.4

Using approximations 3.25 and 3.26 we can write:

$$\begin{aligned}
|r_1 + r_2|^2 &= (a + c)^2 + (b + d)^2 \quad \cong (a + a)^2 + (b + b)^2 \\
&\cong (2a)^2 + (2b)^2 \\
&\cong 2(a^2 + a^2 + b^2 + b^2) \\
&\cong 2(a^2 + c^2 + b^2 + d^2) \\
&\cong 2(|r_1|^2 + |r_1|^2) \tag{3.27}
\end{aligned}$$

hence $\text{Re}(\Delta r/r)$ from equation 3.9 can be approximated as:

$$\text{Re}\left(\frac{\Delta r}{r}\right) \cong \frac{a^2 + b^2 - c^2 - d^2}{(a^2 + c^2 + b^2 + d^2)} \tag{3.28}$$

or using definitions 3.5 and 3.6:

$$\text{Re}\left(\frac{\Delta r}{r}\right) \cong \frac{|r_1|^2 - |r_2|^2}{|r_1|^2 + |r_2|^2} \tag{3.29}$$

Thus the approximations made in equations 3.25 and 3.26 are important as they allow $\text{Re}(\Delta r/r)$ to be expressed in terms of reflectances (power ratio) which is measured by a detector, i.e. $|r_1|^2$ and $|r_2|^2$ rather than reflection coefficients, r_1 and r_2 .

Also using equation 3.27 $\text{Im}(\Delta r/r)$ from equation 3.10 can be written as:

$$\text{Im}\left(\frac{\Delta r}{r}\right) \cong \frac{2(bc - ad)}{(a^2 + c^2 + b^2 + d^2)} \tag{3.30}$$

or using definitions 3.5 and 3.6:

$$\text{Im}\left(\frac{\Delta r}{r}\right) \cong -2 \frac{|r_1||r_2|\sin(\varphi_\Delta)}{|r_1|^2 + |r_2|^2} \tag{3.31}$$

Also if approximations 3.25 and 3.26 hold, then:

$$\text{Im}\left(\frac{\Delta r}{r}\right) \cong \sin(\varphi_{\Delta}) \quad (3.32)$$

And again if approximations 3.25 and 3.26 hold then φ_{Δ} will be close to zero, therefore:

$$\text{Im}\left(\frac{\Delta r}{r}\right) \cong \varphi_{\Delta} \quad (3.33)$$

where φ_{Δ} is in radians.

Hence $\text{Im}(\Delta r/r)$ in a low anisotropy sample is equal to the phase difference between the Fresnel reflection coefficients.

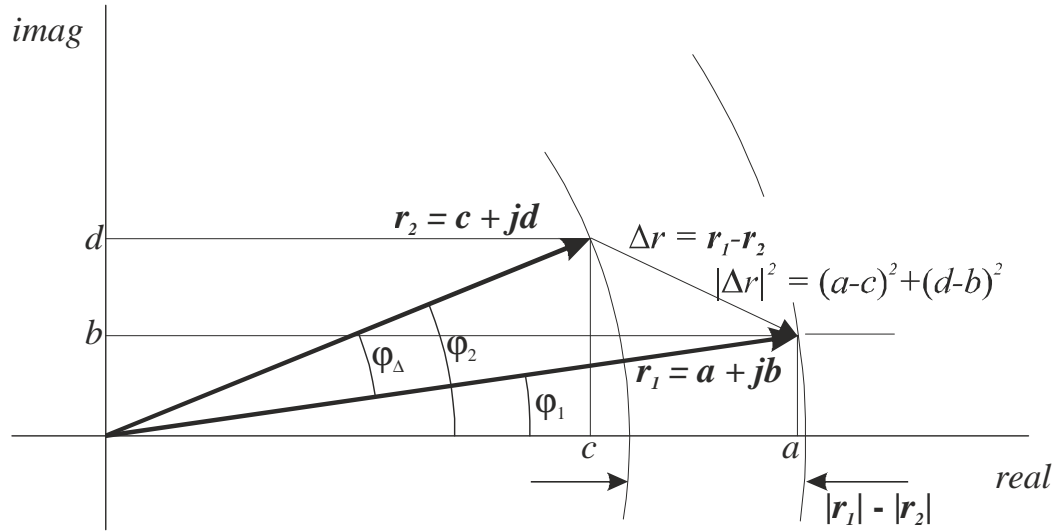


Figure 3.2 Argand diagram of Fresnel reflection coefficient eigenvalues, r_1 and r_2 .

The approximations for $\text{Re}(\Delta r/r)$ and $\text{Im}(\Delta r/r)$ above in equations 3.28 and 3.30 will be shown later (section 3.4.7) to be the exact output of a PEM-based RAS instrument (with the sample in the standard orientation of $\pi/4$ radian).

3.4 Instrumentation analysis

Here the output of the simple rotating-sample RAS instrument is examined and compared to the RAS definition, before the more complex PEM-based instrument. The analysis of the PEM-based instrument is extended from its normal fixed-sample orientation mode to a rotation mode. This rotational mode is referred to as ADRAS, Azimuthal Dependent Reflection Anisotropy Spectroscopy.

3.4.1 Rotating-sample RAS (non PEM)

In chapter 2 we introduced the Aspnes rotating-sample RAS. Here we more thoroughly examine the output of the instrument.

The complex Fresnel reflection coefficient, r , is by definition

$$\frac{E_{ref}}{E_{inc}} = r \quad (3.34)$$

where E_{inc} and E_{ref} are the respective incident and reflected electric field waves of the light. Light intensity, which has units of power, is proportional to the product of the electric field and its complex conjugate. Thus:

$$\frac{E_{ref}}{E_{inc}} \frac{E_{ref}^*}{E_{inc}^*} = rr^* = |r|^2 = \frac{P_{ref}}{P_{inc}} = R \quad (3.35)$$

where P_{ref} and P_{inc} are the respective reflection and incident power levels, R is by definition the sample reflectance and $*$ denotes complex conjugate. The difference in reflectance measured by the rotating-sample RAS, ΔR is thus:

$$\Delta R = R_1 - R_2 = |r_1|^2 - |r_2|^2 \quad (3.36)$$

with the overall reflectance, R :

$$R = (R_1 + R_2)/2 = (|r_1|^2 + |r_2|^2)/2 \quad (3.37)$$

Hence, dividing equation 3.36 by equation 3.37, the RAS value given by the rotating-sample instrument is:

$$\frac{\Delta R}{R} = \frac{2(|r_1|^2 - |r_2|^2)}{(|r_1|^2 + |r_2|^2)} \quad (3.38)$$

Using approximate equation 3.29 we see that:

$$\frac{\Delta R}{R} \cong 2 \operatorname{Re} \left(\frac{\Delta r}{r} \right) \quad (3.39)$$

Thus the rotating-sample RAS output for low anisotropy approximates to $2 \times$ real part of the RAS signal.

3.4.2 PEM-based RAS instrument analysis (with rotating-sample)

Chapter 2 gives a general description of the standard Aspnes PEM-based RAS instrument, which is designed to have the sample (usually a crystal) orientated such that the principal axis of the anisotropy is orientated at $\theta = \pi/4$ rad. In this analysis all values of θ are considered. This is important as experimentally the direction of the anisotropy may not be known and may also be a function of wavelength. Additionally the anisotropy may not coincide with the crystal principal axes, so the anisotropy will be referred to in terms of the eigenvectors and eigenvalues of the Fresnel reflection coefficient tensor.

By combining sample rotation and a PEM, more information can be obtained about the sample than just the output of the RAS instrument at a fixed sample orientation. Referring to the model of the RAS instrument in figure 3.3, the frame of reference is taken with respect to the laboratory vertical for the y component of the light. The x component is taken as pointing horizontally to the right while facing in the direction of propagation, whilst the z (not shown) is taken in the direction of propagation. The eigenvalues of the sample Fresnel reflection coefficient tensor are denoted as r_1 and r_2 . In the standard instrument the sample orientation is setup such that the eigenvector, v_1 , associated with r_1 is at $\pi/4$ radian to the x coordinate of the frame of

reference. In this analysis the sample is free to rotate, with its angle, θ , defined as between x and v_1 .

The polariser is fixed so that it polarises light in the y direction. The photoelastic modulator (PEM) is mounted with its fast and slow axes aligned with the x and y directions. The analyser is mounted at $\pi/4$ radian to x . The detector is assumed to give an output proportional to the light intensity after the analyser.

This analysis omits any window strain that may be present and thus affect the RAS spectrum.

3.4.3 Using Jones matrix formalisation

Figure 3.4 shows a schematic model of the RAS instrument with the different optical stages. Jones matrix formalisation [2] is used to analyse the instrument from the output of the polariser to the input of the detector. Jones matrices can only be used for polarised light so we make the inherent assumption that the polariser is perfect and the light from the polariser to the detector remains polarised (linearly, circularly or elliptically).

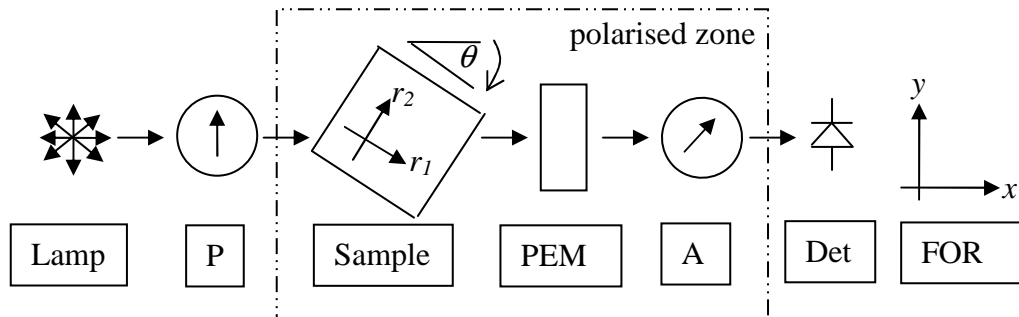


Figure 3.3 Schematic model of the RAS instrument with the different optical stages. The polarised zone is where Jones Matrixes are applicable. P is the polariser, A is the analyser, Det is the detector and FOR denotes frame of reference.

From the polariser output to detector input we have the following:

$$\text{Polarised light vector after polariser} = \begin{bmatrix} 0 \\ 1 \end{bmatrix} \quad (3.40)$$

$$\text{Rotated sample tensor, } Q(\theta) \equiv \begin{bmatrix} q_{11} & q_{12} \\ q_{21} & q_{22} \end{bmatrix} \quad (3.41)$$

$$\text{PEM tensor} = \begin{bmatrix} e^{i\delta} & 0 \\ 0 & 1 \end{bmatrix} \quad (3.42)$$

$$\text{Analyser tensor} = \frac{1}{2} \begin{bmatrix} 1 & 1 \\ 1 & 1 \end{bmatrix} \quad (3.43)$$

$$\text{Polarised light vector at detector} = \begin{bmatrix} x \\ y \end{bmatrix} \quad (3.44)$$

The result of the optical layout in figure 3.4 is thus:

$$\begin{bmatrix} x \\ y \end{bmatrix} = \frac{1}{2} \begin{bmatrix} 1 & 1 \\ 1 & 1 \end{bmatrix} \begin{bmatrix} e^{i\delta} & 0 \\ 0 & 1 \end{bmatrix} \begin{bmatrix} q_{11} & q_{12} \\ q_{21} & q_{22} \end{bmatrix} \begin{bmatrix} 0 \\ 1 \end{bmatrix} \quad (3.45)$$

where, δ = instantaneous PEM retardation in radians, q_{11} , q_{12} , q_{21} , q_{22} are the Jones matrix elements of the sample after rotation by θ , and, x and y are the complex coordinate values of the polarised light. Thus

$$\begin{bmatrix} x \\ y \end{bmatrix} = \frac{1}{2} \begin{bmatrix} 1 & 1 \\ 1 & 1 \end{bmatrix} \begin{bmatrix} q_{12}e^{i\delta} \\ q_{22} \end{bmatrix} \quad (3.46)$$

therefore

$$x = y = \frac{q_{12}e^{i\delta} + q_{22}}{2}. \quad (3.47)$$

Instead of calculating the rotated sample tensor separately for each value of θ , a fixed tensor, S , can be used for the sample with a rotation matrix applied before and after it. In general the fixed sample tensor, S , could be defined at any physical orientation to the frame of reference, say for example a physical mark on the sample. The fixed sample tensor could be defined as;

$$S = \begin{bmatrix} s_{11} & s_{12} \\ s_{21} & s_{22} \end{bmatrix} \quad (3.48)$$

where s_{11} , s_{12} , s_{21} and s_{22} are the complex tensor elements of the sample at the specified orientation.

For what follows in this chapter the sample's physical orientation is defined as 0 radian when s_{12} and s_{21} are zero and s_{11} (rather than s_{22}) acts in the x direction of the optical frame of reference. The assumption is made that tensor S is diagonalisable, *i.e.* both s_{12} and s_{21} can be zero at the same time.

With the sample at this orientation of 0 rad, s_{11} and s_{22} are equal to the eigenvalues of the sample reflection coefficient, r_1 and r_2 respectively. In this case the sample tensor S becomes;

$$S = \begin{bmatrix} r_1 & 0 \\ 0 & r_2 \end{bmatrix} \quad (3.49)$$

The tensor for the sample rotated at any given angle θ , $Q(\theta)$, is thus;

$$\begin{aligned} Q(\theta) &= \begin{bmatrix} \cos(-\theta) & \sin(-\theta) \\ -\sin(-\theta) & \cos(-\theta) \end{bmatrix} \begin{bmatrix} r_1 & 0 \\ 0 & r_2 \end{bmatrix} \begin{bmatrix} \cos(\theta) & \sin(\theta) \\ -\sin(\theta) & \cos(\theta) \end{bmatrix} \\ &= \begin{bmatrix} r_1 \cos^2 \theta + r_2 \sin^2 \theta & r_1 \sin \theta \cos \theta - r_2 \sin \theta \cos \theta \\ r_1 \sin \theta \cos \theta - r_2 \sin \theta \cos \theta & r_1 \sin^2 \theta + r_2 \cos^2 \theta \end{bmatrix} \end{aligned} \quad (3.50)$$

hence equation 3.47 becomes:

$$x = y = \frac{1}{2} e^{i\delta} (r_1 \sin \theta \cos \theta - r_2 \sin \theta \cos \theta) + \frac{1}{2} r_1 \sin^2 \theta + r_2 \cos^2 \theta \quad (3.51)$$

Substituting equations 3.5 and 3.6 into equation 3.51 we get, after expansion and simplification:

$$\begin{aligned}
x = y = & [a \sin \theta \cos \theta \cos \delta - c \sin \theta \cos \theta \cos \delta \\
& - b \sin \theta \cos \theta \sin \delta + d \sin \theta \cos \theta \sin \delta \\
& + a \sin^2 \theta + c \cos^2 \theta \\
& + i(b \sin \theta \cos \theta \cos \delta - d \sin \theta \cos \theta \cos \delta) \\
& + i(a \sin \theta \cos \theta \sin \delta - c \sin \theta \cos \theta \sin \delta) \\
& + i(b \sin^2 \theta + d \cos^2 \theta)]/2
\end{aligned} \tag{3.52}$$

3.4.4 Detector output

The detector measures the intensity so in order to get the detector response to the light after passing through the analyser each component of the polarised light vector must be multiplied by its complex conjugate, thus light intensity, I , at detector:

$$I = xx^* + yy^* = 2xx^* = 2yy^* \tag{3.53}$$

Substituting equation 3.52 into 3.53 and after extensive expansion and simplification we get the following expression for the intensity, I :

$$\begin{aligned}
I = & \cos \delta \left(\sin 2\theta (a^2 + b^2 - c^2 - d^2)/4 - \sin 4\theta ((a - c)^2 + (b - d)^2)/8 \right) \\
& + \sin \delta \sin 2\theta (ad - bc)/2 \\
& + (a^2 + c^2 + b^2 + d^2)/4 + \cos 2\theta (c^2 + d^2 - a^2 - b^2)/4
\end{aligned} \tag{3.54}$$

This describes the instantaneous detector output of an ideal Aspnes RAS instrument as a function of both the instantaneous retardation, δ , and sample orientation, θ .

3.4.5 Detector output as function of PEM frequency ωt

The PEM retardation, δ , is a function of the driving voltage applied to the birefringent optical element. When zero voltage is applied the response of the PEM is isotropic and shows no birefringence. The driving voltage is sinusoidal and to first order the resulting retardation is:

$$\delta = A \sin \omega t \tag{3.55}$$

where δ is the retardation, in radians, ω is the angular frequency of the PEM, t is time and A is the maximum retardation in radians. Thus substituting expression for δ in equation 3.55 into 3.54 gives:

$$\begin{aligned}
I = & \cos(A \sin \omega t) \left[\sin 2\theta (a^2 + b^2 - c^2 - d^2) / 4 - \sin 4\theta ((a - c)^2 + (b - d)^2) / 8 \right] \\
& + \sin(A \sin \omega t) \sin 2\theta (ad - bc) / 2 \\
& + (a^2 + c^2 + b^2 + d^2) / 4 + \cos 2\theta (c^2 + d^2 - a^2 - b^2) / 4
\end{aligned} \tag{3.56}$$

3.4.6 Jacobi–Anger expansion

Using Jacobi–Anger expansion [39] the terms $\cos(A \sin(\omega t))$ and $\sin(A \sin(\omega t))$ can be expanded thus:

$$\cos(A \sin \omega t) = J_0 + \sum_{n=1}^{\infty} (-1)^n J_{2n} \cos(2n \omega t) \tag{3.57}$$

$$\sin(A \sin \omega t) = 2 \sum_{n=1}^{\infty} J_{2n-1} \sin[(2n-1) \omega t] \tag{3.58}$$

where $J_0, J_1, J_2 \dots J_n$ are Bessel functions of the first kind which can be calculated from:

$$J_{\alpha}(A) = \sum_{m=0}^{\infty} \frac{(-1)^m}{m!(m+\alpha)!} \left(\frac{A}{2} \right)^{2m+\alpha}. \tag{3.59}$$

Substituting for $\cos(A\sin(\omega t))$ and $\sin(A\sin(\omega t))$, in equation 3.56, using respectively equations 3.57 and 3.58, we get:

$$\begin{aligned}
I = & (J_0 + 2J_2 \cos 2\omega t + 2J_4 \cos 4\omega t \dots) \\
& \times [\sin 2\theta (a^2 + b^2 - c^2 - d^2)/4 - \sin 4\theta ((a-c)^2 + (b-d)^2)/8] \\
& + (2J_1 \sin \omega t + 2J_3 \sin 3\omega t \dots) \sin 2\theta (ad - bc)/2 \\
& + (a^2 + c^2 + b^2 + d^2)/4 + \cos 2\theta (c^2 + d^2 - a^2 - b^2)/4
\end{aligned} \tag{3.60}$$

This is the detector output of an ideal Aspnes RAS instrument as a function of both the PEM phase, ωt , and the sample orientation, θ .

3.4.7 Linking experimental measurable quantities, to sample anisotropy

By extracting the experimental measurable quantities, I_{dc} , $I_{1\omega}$, and $I_{2\omega}$ which correspond respectively to the DC, ωt and $2\omega t$ components from I in equation 3.60 we get the following relationships:

$$\begin{aligned}
I_{DC}(\theta) = & (a^2 + c^2 + b^2 + d^2)/4 + \cos 2\theta (c^2 + d^2 - a^2 - b^2)/4 \\
& + J_0 [\sin 2\theta (a^2 + b^2 - c^2 - d^2)/4 - \sin 4\theta ((a-c)^2 + (b-d)^2)/8]
\end{aligned} \tag{3.61}$$

as $(a^2 + c^2 + b^2 + d^2) \gg (c^2 + d^2 - a^2 - b^2)$ and if the retardation is chosen so that $J_0 = 0$ (see section 3.6), then equation 3.61 reduces to:

$$I_{DC}(\theta) \cong (a^2 + c^2 + b^2 + d^2)/4 \tag{3.62}$$

$$I_{1\omega}(\theta) = J_1 \sin 2\theta (ad - bc) \tag{3.63}$$

$$\begin{aligned}
I_{2\omega}(\theta) = & J_2 [\sin 2\theta (a^2 + b^2 - c^2 - d^2)/2 \\
& - \sin 4\theta ((a-c)^2 + (b-d)^2)/4]
\end{aligned} \tag{3.64}$$

Replacing θ with $\pi/4$ radian gives the standard Aspnes instrument:

$$I_{DC}(\pi/4) = (a^2 + c^2 + b^2 + d^2)/4 \quad (3.65)$$

$$\begin{aligned} I_{1\omega}(\pi/4) &= J_1 \sin(2\pi/4)(ad - bc) \\ &= J_1(ad - bc) \end{aligned} \quad (3.66)$$

$$\begin{aligned} I_{2\omega}(\pi/4) &= J_2 [\sin 2\pi/4 (a^2 + b^2 - c^2 - d^2)/2 \\ &\quad - \sin 4\pi/4 ((a - c)^2 + (b - d)^2)/4] \\ &= J_2 (a^2 + b^2 - c^2 - d^2)/2. \end{aligned} \quad (3.67)$$

[note: for $\theta = \pi/4$ the $\cos 2\theta$ term in equation 3.61 is zero so equation 3.65 is exact (providing $J_0 = 0$)]

Rewriting equations 3.65, 3.66 and 3.67

$$a^2 + c^2 + b^2 + d^2 = 4I_{DC}(\pi/4) \quad (3.68)$$

$$ad - bc = I_{1\omega}(\pi/4)/J_1 \quad (3.69)$$

$$a^2 + b^2 - c^2 - d^2 = 2I_{2\omega}(\pi/4)/J_2 \quad (3.70)$$

Equations 3.68 to 3.70 relate the sample parameters (a, b, c, d), to the observable outputs, I_{DC} , $I_{1\omega}$ and $I_{2\omega}$, of the PEM-based RAS instrument, when the sample is orientated at $\pi/4$ rad. From section 3.3 (RAS definition and analysis) we have the approximations 3.28 and 3.30 that relate $\text{Re}(\Delta r/r)$ and $\text{Im}(\Delta r/r)$ respectively to the sample parameters a, b, c and d .

Thus we can now relate the real and imaginary parts of $(\Delta r/r)$ to the PEM-based RAS instrument. The output of the RAS instrument that relates to $\text{Im}(\Delta r/r)$ is termed *RAS1* and the output that relates to $\text{Re}(\Delta r/r)$ is termed *RAS2*, as defined below.

Hence:

$$\operatorname{Re}\left(\frac{\Delta r}{r}\right) \cong \frac{a^2 + b^2 - c^2 - d^2}{(a^2 + c^2 + b^2 + d^2)} = \frac{1}{2J_2} \frac{I_{2\omega}(\pi/4)}{I_{DC}(\pi/4)} \equiv RAS2 \quad (3.71)$$

$$\operatorname{Im}\left(\frac{\Delta r}{r}\right) \cong \frac{(bc - ad)}{(a^2 + c^2 + b^2 + d^2)} = \frac{-1}{2J_1} \frac{I_{1\omega}(\pi/4)}{I_{DC}(\pi/4)} \equiv RAS1 \quad (3.72)$$

expressed in terms of r_1 , r_2 and φ_Δ :

$$\operatorname{Re}\left(\frac{\Delta r}{r}\right) \cong \frac{|r_1|^2 - |r_2|^2}{|r_1|^2 + |r_2|^2} = \frac{1}{2J_2} \frac{I_{2\omega}(\pi/4)}{I_{DC}(\pi/4)} \equiv RAS2 \quad (3.73)$$

$$\operatorname{Im}\left(\frac{\Delta r}{r}\right) \cong \frac{4|r_1||r_2|\sin(\varphi_\Delta)}{|r_1|^2 + |r_2|^2} = \frac{-1}{2J_1} \frac{I_{1\omega}(\pi/4)}{I_{DC}(\pi/4)} \equiv RAS1 \quad (3.74)$$

This shows that the PEM-based RAS analysis, done for a sample in an arbitrary direction, agrees with Aspnes [18] when the sample is in the standard orientation, $\theta = \pi/4$ rad.

Note that from equations 3.71 and 3.72 the *RAS2* and *RAS1* outputs of the PEM-based RAS instrument are equal to the *approximate* values for $\operatorname{Re}(\Delta r/r)$ and $\operatorname{Im}(\Delta r/r)$ respectively. The accuracy of this approximation depends on low sample anisotropy, i.e. on the validity of $a \cong c$ & $b \cong d$. This will be investigated in chapter 4 section 4.4, see 3D plots figures 4.8, 4.9, 4.10 and 4.11.

When the sample is not in the standard orientation the output of the RAS instrument not only depends on the reflectivity of the sample but on the sample's azimuthal orientation, θ , as shown in equations 3.61, 3.63 and 3.64. The output of the RAS instrument shown in equations 3.71 and 3.72 gives the respective real and imaginary values of RAS, at the standard sample orientation of $\theta = \pi/4$ rad. At other values of θ the output of the RAS instrument is denoted *ADRAS1* and *ADRAS2* as shown below:

$$ADRAS1(\theta) = \frac{-1}{2J_1} \frac{I_{1\alpha}(\theta)}{I_{DC}(\theta)} \quad (3.75)$$

$$ADRAS2(\theta) = \frac{1}{2J_2} \frac{I_{2\alpha}(\theta)}{I_{DC}(\theta)} \quad (3.76)$$

Substituting from equations 3.62, 3.63 and 3.64 into equations 3.75 and 3.76 gives expression for *ADRAS1* and *ADRAS2* in terms of sample reflection coefficients, a, b, c, d and sample angle θ as follows:

$$\begin{aligned} ADRAS1(\theta) &= \frac{-1}{2J_1} \frac{J_1 \sin 2\theta (ad - bc)}{(a^2 + c^2 + b^2 + d^2)/4} \\ &= 2 \frac{\sin 2\theta (bc - ad)}{(a^2 + c^2 + b^2 + d^2)} \end{aligned} \quad (3.77)$$

$$ADRAS2(\theta) = \frac{\sin 2\theta (a^2 + b^2 - c^2 - d^2)}{(a^2 + c^2 + b^2 + d^2)} - \frac{\sin 4\theta ((a - c)^2 + (b - d)^2)}{2(a^2 + c^2 + b^2 + d^2)} \quad (3.78)$$

Referring back to section 3.3 and the RAS definition we see from equation 3.30 that equation 3.77 can be written as:

$$ADRAS1(\theta) \cong \sin 2\theta \operatorname{Im}\left(\frac{\Delta r}{r}\right) \quad (3.79)$$

Again from the RAS definitions in section 3.3 using equations 3.28, 3.11 and 3.18, in equation 3.76, *ADRAS2*(θ) can be written as:

$$ADRAS2(\theta) \cong \sin 2\theta \operatorname{Re}\left(\frac{\Delta r}{r}\right) - \sin 4\theta \frac{|\Delta r|^2}{|r|^2}. \quad (3.80)$$

By normalising the reflectivity, so that $|r|=1$, we see from equation 3.80 that *ADRAS2*(θ) always has a $\sin 4\theta$ component, if there is any anisotropy, and as this is dependent on $|\Delta r|^2$ this will usually be much less than $\operatorname{Re}(\Delta r)$.

3.5 Reflection in terms of complex refractive index

From Fresnel's equations at normal incidence:

$$r = \frac{1 - \tilde{n}}{1 + \tilde{n}} \quad (3.81)$$

where r is reflectivity and \tilde{n} is the complex refractive index. It follows that

$$\tilde{n} = \frac{1 - r}{1 + r} \quad (3.82)$$

We can also write

$$r = \frac{1 - (n - jk)}{1 + (n - jk)} \quad (3.83)$$

where the convention $\tilde{n} = n - jk$ is used. Thus equation 3.5 can be written as

$$r = \frac{1 - n^2 + j2k - k^2}{(1 + n)^2 + k^2} \quad (3.84)$$

for $r_x = a + jb$

$$a = \frac{1 - n_x^2 - k_x^2}{(1 + n_x)^2 + k_x^2} \quad (3.85)$$

$$b = \frac{2k_x}{(1 + n_x)^2 + k_x^2} \quad (3.86)$$

similarly for $r_y = c + jd$

$$c = \frac{1 - n_y^2 - k_y^2}{(1 + n_y)^2 + k_y^2} \quad (3.87)$$

$$d = \frac{2k_y}{(1 + n_y)^2 + k_y^2} \quad (3.88)$$

3.6 Sample rotation angle

In the work above the rotation angle, θ , is defined as being between the x direction of the frame of reference and an eigenvector of the anisotropy. However because the eigenvectors are a function of wavelength, the rotation angle, θ , will also be a function of wavelength. It is therefore necessary to define the frame of reference at a particular wavelength, and introduce a phase term to the ADRAS signal. The rotation angle θ can then be expressed as the sum of a common angle, denoted θ_r , and a wavelength depended phase, ϕ , *i.e.*:

$$\theta = \theta_r + \phi \quad (3.89)$$

Figure 3.4 illustrates the relationship between θ , θ_r and ϕ , and also includes θ_x which represents a completely arbitrary reference used in the experiment, which may simply be a physical mark on the sample. After experimental data has been taken θ_r maybe chosen based on the overall dominant direction of the anisotropy, this is often chosen to be aligned with a crystal principal axis, if a crystal is used.

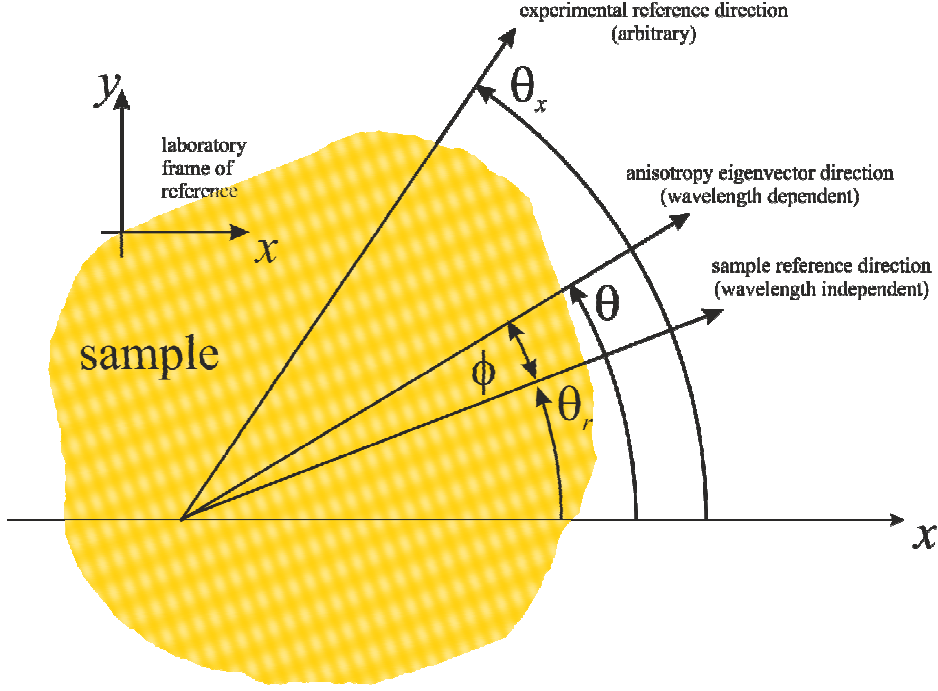


Figure 3.4 Illustration of relationship between sample orientation angles. In the mathematical analysis θ is the angle between the x direction of the frame of reference and the eigenvector of the sample reflection coefficient, r_1 in equation 3.50. The angle θ_x represents the angle recorded during the experiment. The angle θ_r is the angle chosen as a reference that is independent of wavelength and is often a particular crystal principal axis. The angle ϕ represents the difference between θ and θ_r and can be wavelength dependent.

ADRAS equations, such as 3.79 and 3.80 can then be written as:

$$ADRAS1(\theta_r + \phi) = \sin 2(\theta_r + \phi) \text{Im}\left(\frac{\Delta r}{r}\right) \quad (3.90)$$

$$ADRAS2(\theta_r + \phi) = \sin 2(\theta_r + \phi) \text{Re}\left(\frac{\Delta r}{r}\right) - \sin 4(\theta_r + \phi) \frac{|\Delta r|^2}{|r|^2}. \quad (3.91)$$

Thus *ADRAS1* and *ADRAS2* can thus be plotted against θ_r with a phase shift of ϕ .

During an experiment the eigenvector directions of the sample anisotropy will probably be unknown, and so the orientation may be completely arbitrary, In this case the orientation angle is deemed to be θ_x . and will have a constant offset to θ_r .

3.7 Exploiting sample rotation

Equations 3.61, 3.63 and 3.64 show the values for I_{DC} , $I_{1\alpha}$ and $I_{2\alpha}$ respectively. If the retardation is set (see section 3.8 determining optimum retardation, below) such that $J_1 = 0$, then I_{DC} will have a large DC component plus a small $\cos(2\theta)$ anisotropic dependent component. So strictly speaking I_{DC} is not purely DC, but if the anisotropy is small then I_{DC} can be considered effectively DC. The $I_{1\alpha}$ value varies as $\sin 2\theta$ hence will be a maximum at $\theta = \pi/4$ radians and zero at $\theta = \pi/2$ radians. The $I_{2\alpha}$ value has two components $\sin 2\theta$ and $-\sin 4\theta$. Consequently $I_{2\alpha}$ has a $\sin 2\theta$ component in-phase with $I_{1\alpha}$, and a $-\sin 4\theta$ component that will be zero every $\theta = \pi/4$ rotation. This means in the standard Aspnes PEM-based RAS, the ' $\sin 4\theta((a-c)^2 + (b-d)^2)$ ' term in equation 3.64 does not contribute to the output. Figure 3.2 shows how $(a-c)^2 + (b-d)^2 = \Delta r^2$, where Δr is the difference between r_1 and r_2 . This means that if there is any anisotropy, *i.e.* $\Delta r \neq 0$, then there will be always be a $\sin 4\theta$ component. However the $\sin 2\theta$ component in equation 3.64 may be zero if $a^2 + b^2 = c^2 + d^2$.

The expressions for *ADRAS2* show that if the anisotropy eigenvectors are a function of wavelength then using a standard RAS instrument cannot give an accurate spectrum for $\text{Re}(\Delta r/r)$. However using the *ADRAS* technique and by extracting the 2θ component an accurate value for $\text{Re}(\Delta r/r)$ can in theory be obtained at each wavelength.

3.8 Determining optimum retardation

In order to understand the data from the RAS instrument it is essential to set the correct maximum retardation, A , as this determines the values of the Bessel functions, $J_0(A)$, $J_1(A)$ and $J_2(A)$, see equation 3.59, and thus the instrument output.

Figure 3.4 illustrates the how the choice of retardation affects how the RAS instrument operates. For example to maximise the 2α component which relates to the real part of the signal, a retardation of $A = 3.054$ radian would be used as this coincides with the peak in J_2 . However if accuracy was important a retardation of

approx $A = 2.4$ radian would make J_0 zero and thus reduce the anisotropic contribution to the DC value, to that shown in equation 3.62.

PEM controllers, such as the Hinds Instruments PEM 100 [28] can set the retardation at each wavelength, and thus a constant retardation across the spectrum can be achieved. If this is not done the retardation will vary with wavelength and will thus have to be taken into account.

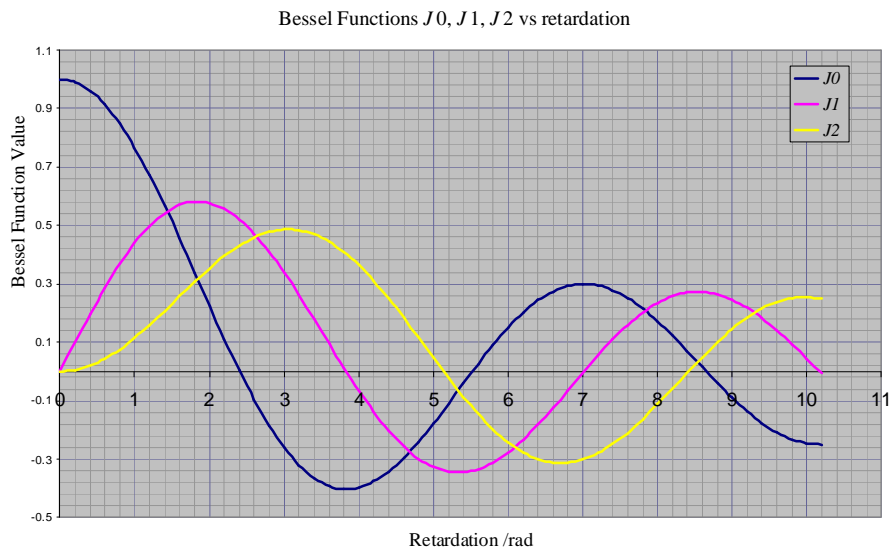


Figure 3.5 Variation of Bessel functions J_0 , J_1 , and J_2 as function of the maximum retardation, A .

Chapter 4: Simulation of PEM-based RAS instrument

4.1 Simulation of PEM-based RAS instrument	58
4.1.1 Simulation using Jones matrix formalisation	58
4.1.2 Simulation of multiple stage system	60
4.1.3 Simulation over one PEM cycle	61
4.1.4 Simulation of lock-in amplifier	62
4.1.5 Basic overall code for a single rotation of the sample	64
4.2 Checking simulation against analytical expression	66
4.3 Detector output as function of sample properties for $\theta = 0.25 \pi$ rad	68
4.3.1 Case 1: $\varphi_1 = \varphi_2, r_1 \neq r_2 $	69
4.3.2 Case 2: $\varphi_1 \neq \varphi_2, r_1 = r_2 = 1$	71
4.3.3 Case 3: $\varphi_1 \neq \varphi_2, r_1 \neq r_2 $	73
4.4 $\text{Re}(\Delta r/r)$ and $\text{Im}(\Delta r/r)$ compared to simulated RAS1 and RAS2	73
4.4.1 $\text{Re}(\Delta r/r)$ compared to simulated RAS2 from RAS instrument	73
4.4.2 $\text{Im}(\Delta r/r)$ compared to simulated RAS1 from RAS instrument	75
4.5 Detector output as function of rotating sample	76
4.5.1 RAS instrument rotation waveform component I_{DC}	77
4.5.2 RAS instrument rotation waveform component	78
4.5.3 RAS instrument rotation waveform components	80
4.5.4 RAS instrument ADRAS simulation	80
4.6 Conclusion	84

4.1 Simulation of PEM-based RAS instrument

In Chapter 3 the PEM-based RAS instrument was analysed mathematically, this provided insight into how the output of the instrument was affected by sample reflection coefficients and sample azimuth orientation. The output of the RAS instrument under sample rotation was termed ADRAS. In this chapter a computer simulation is described that was used to model the instrument using the Jones matrix formalisation [2].

The simulation program developed here is able to set the sample tensors elements to any complex values, however for clarity and for comparison with chapter 3 the simulation was limited to the sample tensor being diagonalisable, with eigenvalues r_1 and r_2 . The same laboratory frame of reference was used as in the analysis in chapter 3, with the z axis defined as the propagation direction, and with the sample orientation defined as the angle between the eigenvector of r_1 and the x direction.

A simulation of this kind lacks the analysis as carried out in chapter 3 but has more flexibility to deal with parameter changes in any of the stages. It also allows the analysis of chapter 3 to be checked for algebraic mistakes, and allows the approximations made in chapter 3 to be validated over an operation range.

To distinguish the output of an ideal Aspnes RAS instrument from the exact definition of RAS we use ‘*RAS1*’ as the instrument output that is considered to correspond with $\text{Im}(\Delta r/r)$, and ‘*RAS2*’ as the instrument output that corresponds to $\text{Re}(\Delta r/r)$. When the sample is not in the standard orientation ($\theta = \pi/4$ rad.) the RAS instrument output corresponding to *RAS1* and *RAS2* are termed *ADRAS1* and *ADRAS2* respectively.

4.1.1 Simulation using Jones matrix formalisation

As shown in chapter 3, section 3.4.3, Jones vectors represent polarised light, thus it is assumed that after the polariser the light is 100% polarised (i.e.. linear, circular or elliptical). This simulation uses Jones matrix formalisation and thus assumes 100% polarisation. For partially or unpolarised light Stokes vectors and Mueller calculus can be used [2]. It may also be possible for less than 100% polarisation to be

simulated, using Jones matrixes, by averaging the output due to a distribution of polarisations.

Any general optical stage, or series of optical stages, U , operating under polarised light conditions, can be represented with a Jones matrix:

$$U = \begin{bmatrix} u_{11} & u_{12} \\ u_{21} & u_{22} \end{bmatrix}. \quad (4.1)$$

If U is comprised of multiple stages, U_a, U_b, U_c, U_d , then U is simply the product of all the composite stages *i.e.*:

$$U = U_a U_b U_c U_d. \quad (4.2)$$

As shown in chapter 3, section 3.4.3, a stage can be rotated by applying rotation matrices before and after the matrix that represents the un-rotated stage. Thus any stage U rotated by an azimuth angle, θ , can be represented thus:

$$U(\theta) = R(-\theta).U.R(\theta) \quad (4.3)$$

where R is the rotation matrix.

Therefore operating on a vector, $[x_1, y_1]^T$ gives:

$$[x_2, y_2]^T = R(-\theta).U.R(\theta)[x_1, y_1]^T \quad (4.4)$$

where x_1 and y_1 are the respective complex x and y components of the light before passing through U , and x_2 and y_2 are the resulting components exiting U . A suitable subroutine, in the C programming language [40], to evaluate x_2, y_2 given x_1, y_1, θ , and the matrix elements for U is shown in listing 4.1. The listings are provided show the relatively small amount of code needed to simulate the basics of the RAS instrument.

```

void jones_matrix (complex u[2][2],complex x1, complex
y1,float theta, complex *x2,complex *y2)
{
    // Jones Matrix Subroutine
    // Evaluation of output vector [x2 y2]^T
    // Input vector [x1 y1]^T
    // Input matrix elements u[2,2]
    // Input rotation angle theta
    // rotate stage by angle theta
    complex a[2][2];
    a[1][1] = u[1][1]*cos(theta)*cos(theta)-
              (u[1][2]+u[2][1])*sin(theta)*cos(theta)+
              u[2][2]*sin(theta)*sin(theta);
    a[1][2] = u[1][2]cos(theta)*cos(theta)+
              (u[1][1]-u[2][2])*sin(theta)*cos(theta)-
              u[2][1]*sin(theta)*sin(theta);
    a[2][1] = u[2][1]*cos(theta)*cos(theta)+
              (u[1][1]-u[2][2])*sin(theta)*cos(theta)-
              u[1][2]*sin(theta)*sin(theta);
    a[2][2] = u[2][2]*cos(theta)*cos(theta)+
              (u[2][1]+u[1][2])*sin(theta)*cos(theta)+
              u[1][1]*sin(theta)*sin(theta);
    // output vector [x2 y2]^T
    *x2 = x1*a[1][1]+y1*a[1][2];
    *y2 = x1*a[2][1]+y1*a[2][2];
}

```

Listing 4.1 C code for a Jones vector-matrix product which includes stage rotation, theta. Program variables, x2 and y2 represent the complex output vector components.

4.1.2 Simulation of multiple stage system

The subroutine listed in 4.1 can be used to represent each stage, where the output of one stage becomes the input to the next. When the electric field vector of the light, $[x_d \ y_d]^T$, reaches the detector, the output of the detector is a scalar quantity proportional to the input power level, and is thus proportional to the sum of the squares of the electric field components. If the input electric field vector to the detector is $[x_d \ y_d]^T$ then the detector output is proportional to $x_d x_d^* + y_d y_d^*$ where x_d^* and y_d^* are the complex conjugates of x_d and y_d respectively.

Simulating the complete PEM-based RAS instrument can now be done by the ‘Jones-matrix’ function for each stage. The C code in listing 4.2 illustrates how the output from PEM-based RAS instrument may be simulated, when setup in the normal configuration.

```

void RAS_sim (complex s[2][2], float samp_theta, float
mret, float wt, float *detlev)
{
    // This function evaluates detector output detlev, given
    // the following inputs:
    // complex jones matrix for sample, s[2,2]
    // sample orientation, theta
    // PEM max retardation, mret
    // PEM phase angle, wt
    // x and y are set to the components of polarisation
    // vector
    // leaving polariser orientated vertically
    complex x, y;
    float theta, mres;
    x=0+0i;
    y=1+0i;
    // the following simulates sample using input
    // variables s[1][1],s[1][2],s[2][1],s[2][2]
    //
    jones_matrix(s,x,y,samp_theta,&x,&y);
    // x and y now represent light reflected from sample
    // the following simulates PEM
    s[1][1]= exp(del=mret*sin(wt));
    s[1][2]= 0+0i;
    s[2][1]= 0+0i;
    s[2][2]= 1+0i;
    theta= 0;
    jones_matrix(s,x,y,theta,&x,&y);
    // x and y now represent light output from PEM
    // following simulates analyser
    s[1][1]=1+0i;
    s[1][2]=0+0i;
    s[2][1]=0+0i;
    s[2][2]=0+0i;
    theta=0.25;
    jones_matrix(s,x,y,theta,&x,&y);
    // x and y now represent light output from analyser
    // determining output from detectot 'detlev'
    // compcon(x) returns complex conjugate of x
    detlev=x*compcon(x) + y*compcon(y);
}

```

Listing 4.2 C code listing for RAS-sim. The returned value detlev is the output of the detector.

4.1.3 Simulation over one PEM cycle

To simulate the output of a PEM RAS over 1 cycle of the PEM then ‘RAS_sim’ is called (see listing 4.3), for a range of values, from $\omega t = 0$ to $\omega t = 2\pi$. In the listing 16 steps are used as this is sufficient to accurately obtain the fundamental and 2nd harmonic required to resolve $I_{\omega t}$ and $I_{2\omega t}$ (see equations 3.61 to 3.64 in chapter 3) from the lock-in amplifier.

```

void PEM_cycle (complex s[2][2],float theta, float mret,
float *wave[16])
{
    // Evaluation of waveform output from PEM RAS
    // Input complex jones matrix for sample, s11, s12, s21,
    // s22
    // Input sample orientation, theta
    // Input PEM max retardation, mret
    // output waveform in wave
    float wt, detlev;
    // step wt over 1 cycle in 16 intervals
    For ( int n = 0 ; n<16; n++)
    {
        wt= n*pi/8;
        RAS_sim(s,theta,mret,wt,&detlev)
        wave[n] = detlev;
    }
}

```

Listing 4.3 C code listing to simulate output over 1 PEM cycle

4.1.4 Simulation of lock-in amplifier

The next stage was to simulate the lock-in amplifier [41] (sometimes called a synchronous detector) to determine the components of the light intensity, I , namely I_{DC} , $I_{1\omega}$ and $I_{2\omega}$, see equations 3.61, 3.62, 3.63 and to 3.64 in chapter 3. In the simulation the detector output voltage, V_i , was considered proportional to the light intensity, I . I_{DC} is simply the mean value of I and its measurement does not require a lock-in amplifier, although many lock-in amplifiers do provide analogue to digital converters (ADCs).

A lock-in amplifier essentially consists of an AC coupled multiplier stage, in which the input signal is multiplied by an AC reference, followed by a low pass filter to give the mean value of this product. If the frequency and phase of the reference are the same as the frequency and phase component of the input signal, the mean or DC output of the lock-in is proportional to the amplitude of the input signal at the reference frequency. If the reference signal is derived from the PEM drive voltage then it will be synchronised with the optical polarisation signal. This is shown in more detail in what follows.

Consider the ac output of the detector, and hence the input to the lock-in input, V_i , to be:

$$V_i = A \cos \omega t + B \sin \omega t \quad (4.5)$$

where t is time, A and B are constants and ω is the angular frequency of the PEM.

If we consider a dual channel lock-in amplifier comprising of channels, X and Y, where the X channel reference is V_{ref_X} and the Y channel reference is V_{ref_Y} . Such that

$$V_{ref_X} = \cos \beta t \quad (4.6)$$

$$V_{ref_Y} = \sin \beta t \quad (4.7)$$

where t is time and β is the angular frequency of the reference signal.

The X channel output of the lock-in multiplier, V_{mX} , becomes:

$$\begin{aligned} V_{mX} &= V_i V_{ref_X} \\ &= (A \cos \omega t + B \sin \omega t) \cos \beta t \\ &= A(\cos \omega t \cos \beta t) + B(\sin \omega t \cos \beta t) \end{aligned} \quad (4.8)$$

$$= A \frac{1}{2} (\cos(\omega t - \beta t) + \cos(\omega t + \beta t)) + B \frac{1}{2} (\sin(\omega t + \beta t) + \sin(\omega t - \beta t)) \quad (4.9)$$

If $\beta \neq \omega$ then the mean value of V_{mX} , will tend to zero as $t \gg \left| \frac{1}{(\omega - \beta)} \right|$, this is

because all of the terms in equation 4.9 will be sinusoidal, with the lowest angular frequency being $(\omega - \beta)$. Thus after the low pass filter of the lock-in, the lock-in output, V_{LX} will tend to zero. Similarly If $\beta = \omega$ equation 4.9 becomes:

$$V_{mX} = A \frac{1}{2} (1 + \cos 2\omega t) + B \frac{1}{2} (\sin 2\omega t) \quad (4.10)$$

and so V_{LX} will tend to a dc value equal to the mean of V_{mX} , *i.e.*

$$V_{LX} = \frac{A}{2}$$

Similarly it can be shown that the Y channel output of the lock-in, V_{LY} becomes:

$$V_{LY} = \frac{B}{2}$$

Hence by setting $\beta = \omega$, which is easily done by deriving the lock-in amplifier reference frequency from the PEM controller, the cosine and sine components, at the angular frequency of β , can be extracted from the detector. To extract the cosine and sine values of I_{ω} the angular frequency, β needs to be set to ω . Similarly to extract the cosine and sine values of $I_{2\omega}$ β needs to be set to 2ω .

In this simulation V_{LX} and V_{LY} were calculated from the mean value of V_{mX} and V_{mY} by integrating over a complete PEM cycle, rather than by simulating a low pass filter. This is possible as there is no noise in the simulation and, importantly, no components of the signal longer than the PEM cycle. If the effects of noise, filter time constant and system dynamics are important a low pass filter would have to be incorporated into the simulation. In this simulation the basic operation and comparison with theory is being studied, so noise and dynamics are not being considered. The C code listing to simulate the lock-in is shown in listing 4.4. For convenience listing 4.4 also calculates the mean or ‘DC’ value of the detector output, I_{DC} .

4.1.5 Basic overall code for a single rotation of the sample

By combining the C code functions listed above a basic overall program, ‘rasrot’ was written to simulate the PEM RAS instrument over a complete rotation of the sample, this is shown in listing 4.5. It was this code that formed the core of the simulation program that is used in the rest of the chapter to check the analysis from chapter 3 and to study how the output of the RAS-instrument is affected by sample properties. The final complete program needs a user interface, graphics and file input/output which are not shown.


```

void lock_in (float wave[16],float *Idc, float *x1, float
*x2, float *y1, float *y2)
{
    // Evaluation of lock-in output for PEM RAS
    // input waveform in wave
    // output Idc, x1, y1, x2, y2
    int m, n;
    // initialise
    x1=0;
    y1=0;
    x2=0;
    y2=0;
    m=16;
    for (n = 0; n<m; n++)
    {
        alpha=n*pi/8;
        *Idc = *Idc + wave(alpha);
        x1= x1+wave(alpha)*cos(alpha);
        y1= y1+wave(alpha)*sin(alpha);
        x2= x2+wave(alpha)*cos(2*alpha);
        y2= y2+wave(alpha)*sin(2*alpha);
    }
    *Idc =*Idc/m
    x1= 2*x1/m;
    y1= 2*y1/m;
    x2= 2*x2/m;
    y2= 2*y2/m;
}

```

Listing 4.4 C code listing for simulation of lock-in amplifier .

```

void rasrot(complex s, float mret, float wave[16], Idctheta[16],
xltheta[16], x2theta[16], yltheta[16], y2theta[16])
{
    for(n=0;n<16,n++)
    {
        theta = n*0.125*pi();
        PEM-cycle (s, theta, mret, &wave);
        lock-in (wave,&Idc, &x1, &x2, &y1, &y2);
        Idctheta[n]=Idc;
        xltheta[n]=x1;
        x2theta[n]=x2;
        yltheta[n]=y1;
        y2theta[n]=y2;
    }
}
// array Idctheta contains Idc over 2pi sample rotation
// array xltheta contains Idc over 2pi sample rotation
// array x2theta contains Ilwt as over sample rotation of 2pi
// array yltheta contains Idc as over sample rotation of 2pi
// array y2theta contains Idc as over sample rotation of 2pi

```

Listing 4.5 C code for one sample rotation

4.2 Checking simulation against analytical expression

In what follows the simulated output of the RAS instrument is compared to the analytical expression given in figure 3.60. These should agree if the analysis and simulation have been carried out accurately. Having checked this the values of $RAS1$ and $RAS2$, from the instrument, can be compared to the exact values of $\text{Re}(\Delta r/r)$ and $\text{Im}(\Delta r/r)$ respectively. This is summarised in equations 3.71 and 3.72 which show how $\text{Re}(\Delta r/r)$ and $\text{Im}(\Delta r/r)$ relate to $RAS1$ and $RAS2$ respectively.

The code examples above are written in C, as C is one of the most popular and well understood programming languages. However for convenience the actual simulation was carried out in Labview [42].

The important expectation that is easily verified by the simulation is that in the output from the detector contains no odd numbered cosine terms, such as $\cos(\alpha)$, $\cos(3\alpha)$, $\cos(5\alpha)$ etc. Also there are no even numbered sine terms, such as $\sin(2\alpha)$, $\sin(4\alpha)$, $\sin(6\alpha)$ etc. This is a confirmation of the Jacobi-Anger expansion described in chapter 3 section 3.4.6.

The analytic expression for the output of the PEM-based RAS, equation 3.60, was compared to the simulation program. The light intensity, I , determined by equation 3.60 is a function of a , b , c , and d which are the terms of the complex eigenvalues of the sample tensor, see equations 3.5 and 3.6. I is also a function, via the Bessel function constants, $J_0, J_1, J_2, \dots, J_n$, of the maximum retardation of the PEM denoted A , in equation 3.57 and 3.58. In all the simulations carried out in this chapter the maximum retardation, A , was set to 2.405 rad, this is the retardation value that makes $J_0 = 0$ (see section 3.8), and thus simplifies the expression for I_{DC} in equation 3.61. The equations 3.57 and 3.58 need only be evaluated for $n = 1$ as only the 'DC', α and 2α components need to be calculated for the simulation.

The iteration level of equation 3.59 should be made large enough to ensure accurate computation of the Bessel functions, figure 4.1 shows the \log_{10} of the absolute error in determining the Bessel functions against the number of iterations used. (An iteration level of 30 was chosen as a reference to determine the error.) It shows that

for 13 iterations the error approaches 10^{-15} , which is near the precision limit for the double precision 64 bit IEEE 754-2008 standard [43] used in Labview simulation program.

A comparison of the output from simulation and the output from the analytic expression (equation 3.60), was also carried out. Variables: a, b, c, d were randomly chosen between -2 and +2 ; the maximum retardation was varied between 0 and 3 radian; and the sample orientation was varied between -2π and $+2\pi$. Figure 4.2 shows the difference between the simulation and equation 3.60 for different iteration levels for the determination of the Bessel functions. This shows that as the iteration level, m , approaches 13 the difference between the simulation and equation 3.60 is approximately 10^{-15} , which as noted above, in the determination of the Bessel functions, is the precision limit for the computation.

Thus this indicates that both the analysis in chapter 3 and the simulation in this chapter agree to the precision of the software, provided the Bessel functions are evaluated correctly. This strongly indicates that the analytic expression for the RAS instrument in chapter 3 is correct and has no algebraic mistakes. It also suggests that the simulation is correct and could be used beyond the confinements of the analytic parameters.

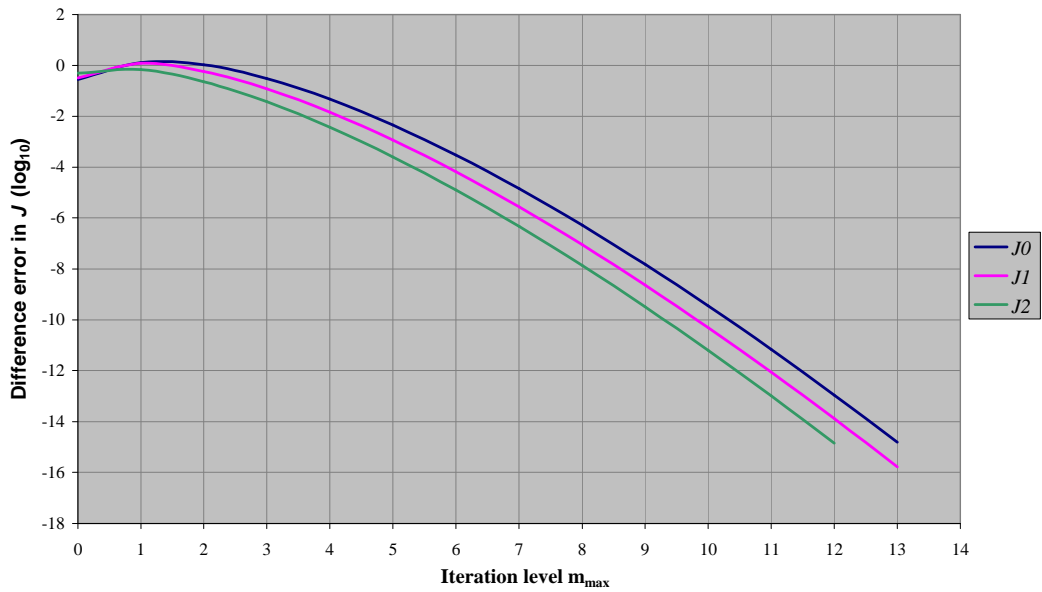


Figure 4.1 Error in determining Bessel functions J_0 , J_1 and J_2 vs iteration level in

equation 3.59. The retardation, A , was set to 2.408 rad which makes $J_0 \cong 0$. Similar error values were obtained for other values of A . The reference value had an iteration level of 30.

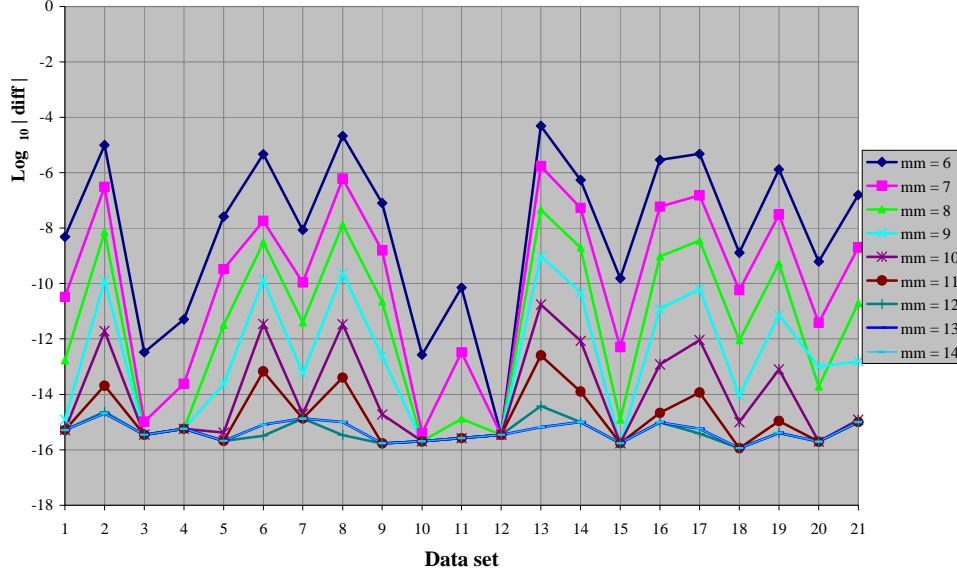


Figure 4.2 Difference between detector output from RAS simulation and RAS analytical solution, (equation 3.60) vs random data set. The maximum iteration level for the calculation of the Bessel functions, J_0 , J_1 and J_2 (equations 3.57 and 3.58), is denoted mm. For each iteration level a random data set of sample reflection coefficients, r_1 , r_2 , and orientation, θ , were chosen (horizontal axis). At an iteration level of mm = 13, the error between simulation and equation 3.60 approaches the floating point accuracy of the software.

4.3 Detector output as function of sample properties for $\theta = 0.25 \pi$ rad

In this section the simulator was used to examine some characteristics of the standard RAS instrument and its accuracy over a wide anisotropic range. The standard RAS instrument means that the r_1 eigenvalue of the sample is at $\pi/4$ rad to the x direction in the frame of reference. Representing the eigenvalues of the sample, r_1 and r_2 , in polar form, $r_1 = |r_1|e^{j\varphi_1}$ and $r_2 = |r_2|e^{j\varphi_2}$, where φ_1 and φ_2 are the respective complex arguments. The sample anisotropy can be due to either a difference between $|r_1|$ and $|r_2|$ and/or a difference between φ_1 and φ_2 .

From the RAS instrument analysis in chapter 3, the detector output is given by equation 3.60, this reduces to the following when the sample is in the standard orientation of $\theta = 0.25 \pi$ rad, and the harmonic content is limited to DC, 1st harmonic and 2nd harmonic:

$$I = (J_0 + 2J_2 \cos 2\alpha)(a^2 + b^2 - c^2 - d^2)/4 + J_1 \sin \alpha(ad - bc) + (a^2 + c^2 + b^2 + d^2)/4 \quad (4.11)$$

Thus the detector output consists of the following:

$$I_{DC} = (a_2 + b_2 + c_2 + d_2)/4 + J_0(a_2 + b_2 - c_2 - d_2)/4 \quad (4.12)$$

$$I_{1\omega} = J_1(ad - bc) \quad (4.13)$$

$$I_{2\omega} = J_2(a_2 + b_2 - c_2 - d_2)/2 \quad (4.14)$$

4.3.1 Case 1: $\varphi_1 = \varphi_2$, $|r_1| \neq |r_2|$

Figure 4.3 shows the ac output waveform from the detector (as would be seen on the output of the detector by an ac-coupled oscilloscope) for different magnitudes of r_1 , but with $\varphi_1 = \varphi_2 = 0$ and $|r_2| = 0.5$. (0.5 was taken as a reference value for r_2 as the reflectivity has to be between 0 and 1.) The traces show an even function, hence they will contain no sine components and hence $I_{1\omega}$ will be zero (equation 4.13 and 3.60), and so $RASI = 0$. The simulation was repeated (not illustrated) with different values of φ_1 , but keeping $\varphi_2 = \varphi_1$. The output was the same as for $\varphi_1 = \varphi_2 = 0$. Consider the following:

$$r_1 = a + jb = |r_1|e^{j\varphi} = |r_1|\cos\varphi + j|r_1|\sin\varphi \quad (4.15)$$

$$r_2 = c + jd = |r_2|e^{j\varphi} = |r_2|\cos\varphi + j|r_2|\sin\varphi \quad (4.16)$$

Thus evaluating $ad - bc$ gives:

$$(ad - bc) = |r_1|\cos\varphi|r_2|\sin\varphi - |r_1|\sin\varphi|r_2|\cos\varphi = 0. \quad (4.17)$$

Hence when $\varphi_2 = \varphi_1$, then $(ad - bc) = 0$ and from equation 3.63 the detector output component, $I_{1\omega t} = 0$. This fits with $\text{Im}\left(\frac{\Delta r}{r}\right) \equiv (\varphi_2 - \varphi_1)$ (equation 3.72).

Figure 4.4 shows how the RAS instrument output, $RAS2$, varies with r_1 given the case 1 conditions, and compares it to the exact $\text{Re}(\Delta r/r)$ value defined by equation 3.4. This shows the region in which the RAS instrument gives accurate results. The largest difference is when $|r_1|$ approaches 0 ($a \rightarrow 0, b = 0$), with $|r_2| = 0.5$ ($c = 0.5, d = 0$) where the RAS output is half the value of $\text{Re}(\Delta r/r)$.

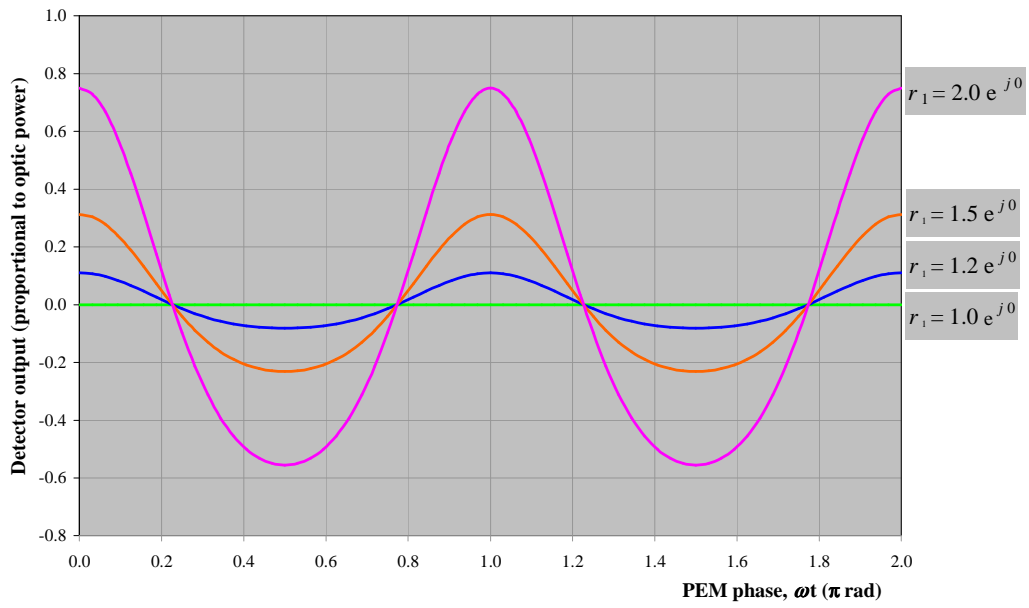


Figure 4.3 Case 1 $\varphi_2 = \varphi_1, |r_1| \neq |r_2|$. This shows the ac output waveform from the detector for different magnitudes of r_1 , but with $\varphi_2 = \varphi = 0$ and $|r_2| = 1$. The even waveform results in the RAS instrument output for $RAS1 = 0$.

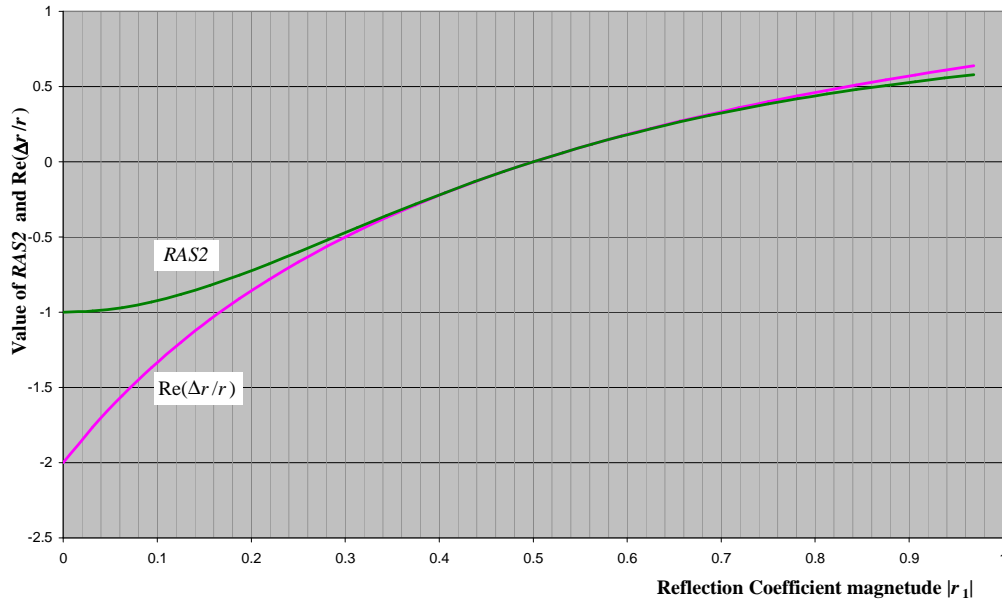


Figure 4.4 Change in RAS instrument output, $RAS2$ and exact $\text{Re}(\Delta r/r)$ with $|r_1|$ given $|r_2| = 0.5$ and $\varphi_1 = \varphi_2 = 0$

4.3.2 Case 2: $\varphi_1 \neq \varphi_2$, $|r_1| = |r_2| = 1$

With $|r_1| = |r_2| = 1$ and $\varphi_2 = 0$, figure 4.5 shows how the detector ac output changes with the complex argument φ_1 . The traces show an odd function, therefore they will not contain any cosine terms. This agrees with equation 3.60 which shows that if $|r_1| = |r_2|$ then $a^2 + b^2 - c^2 - d^2 = 0$, thus making $I_{2\omega} = 0$ as shown in equation 4.14, and so also $RAS2 = 0$.

Figure 4.6 shows how the $RAS1$ output varies with r_1 given the case 2 conditions, and compares it to the exact $\text{Im}(\Delta r/r)$ value, defined by equation 3.4, and to the approximation 3.33, which shows that $\text{Im}(\Delta r/r) \cong \varphi_\Delta$.

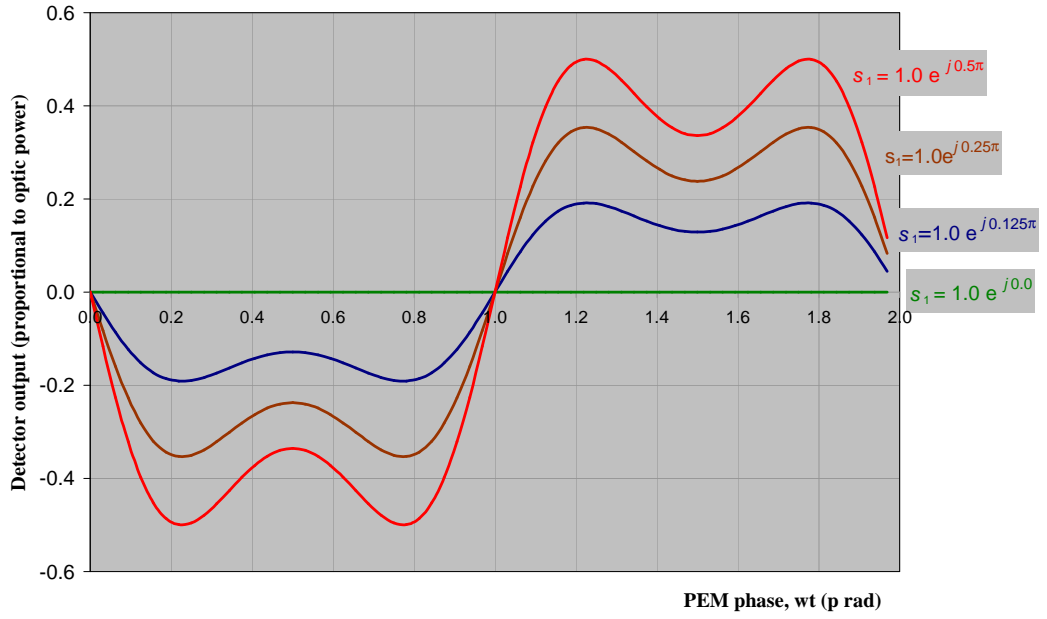


Figure 4.5 Case 2 $\varphi_1 \neq \varphi_2$, $|r_1| = |r_2| = 1$ and $\varphi_1 = 0$. This shows how the detector AC output changes with the complex argument φ_2 . The odd function waveform results in $RAS2 = 0$.

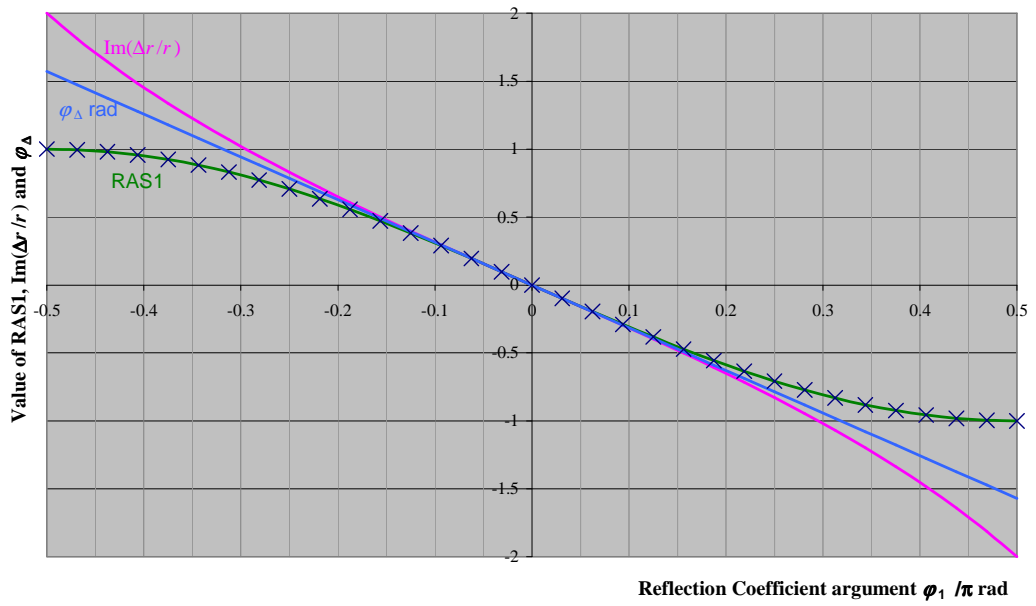


Figure 4.6 Change in $RAS1$ with φ_1 , compared to $\text{Im}(\Delta r/r)$ and φ_Δ , given $|r_1| = |r_2| = 0.5$ and $\varphi_2 = 0$.

4.3.3 Case 3: $\varphi_1 \neq \varphi_2, |r_1| \neq |r_2|$

To illustrate the general case where $\varphi_1 \neq \varphi_2$ and $r_1 \neq r_2$ figure 4.7 shows detector output for $\varphi_1 = 0.1$, $\varphi_2 = 0$, $|r_1| = 0.75$, $|r_2| = 0.5$. As figure 4.7 shows both $I_{1\omega t}$, $I_{2\omega t}$ together with $I_{1\omega t} + I_{2\omega t} + I_{DC}$.

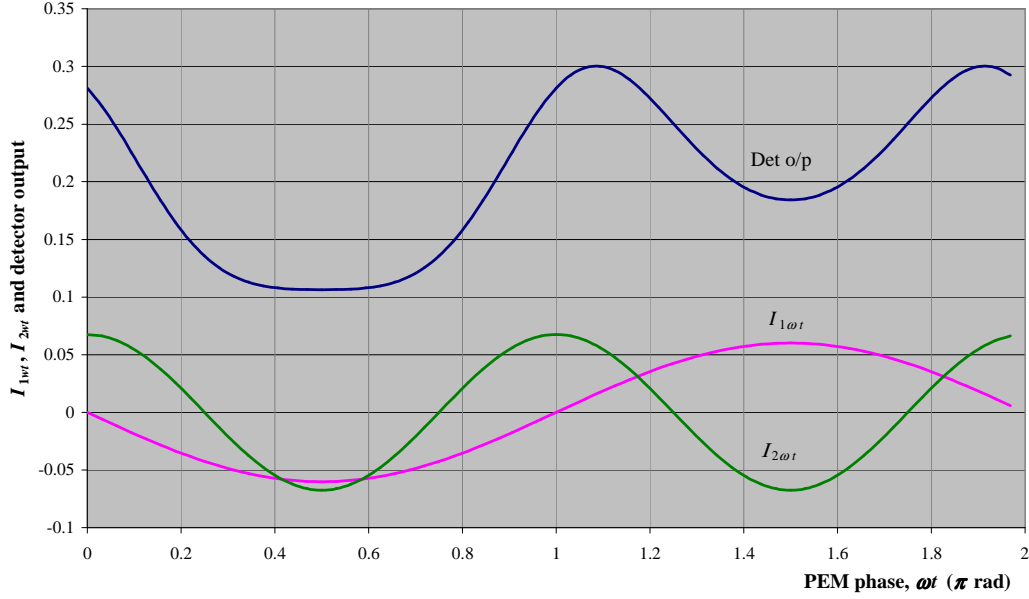


Figure 4.7 Detector output for $\varphi_1 = 0.1$, $\varphi_2 = 0$, $|r_1| = 0.75$, $|r_2| = 0.5$.

4.4 $\text{Re}(\Delta r/r)$ and $\text{Im}(\Delta r/r)$ compared to simulated *RAS1* and *RAS2*

This section shows surface plots illustrating the exact values of $\text{Re}(\Delta r/r)$ and $\text{Im}(\Delta r/r)$ (from equation 3.4) and the simulated instrument outputs, *RAS1* and *RAS2* over the range of reflection coefficient values: $a = 0$ to 1 and $b = -1$ to +1, when $c = 0.5$ and $d = 0$. The difference between these values will show the affects of the approximations $a \cong c$ and $b \cong d$ (equations 3.25 and 3.26). It is only when these approximations hold that $\text{Re}(\Delta r/r) \cong \text{RAS2}$ and $\text{Im}(\Delta r/r) \cong \text{RAS1}$. The sample orientation is maintained at $\theta = 0.25 \pi$ rad. The reflection coefficients are expressed in rectangular ($a + jb$) form so that the surface plots are over the complex plane.

4.4.1 $\text{Re}(\Delta r/r)$ compared to simulated *RAS2* from RAS instrument

The surface/contour plot in figure 4.8 shows the $\text{Re}(\Delta r/r)$ output that would be expected according to the definition of RAS, equation 3.4. This can be compared to the *RAS2* output from the RAS instrument simulation shown in the surface/contour

plot in figure 4.9. The contour plots show that at radius $|r_1| = |r_2| = 0.5$, both $\text{Re}(\Delta r/r)$ and $RAS2$ are zero, and therefore close to this radius $\text{Re}(\Delta r/r) \cong RAS2$.

However at: $a = 0$, $b = 0$ ($c = 0.5$ and $d = 0$), the exact $\text{Re}(\Delta r/r)$ value is -2, whereas the simulated value for $RAS2$ is -1. Comparing these surface plots shows the regions of large anisotropy where the RAS instrument output of $RAS2$ is widely different from the exact $\text{Re}(\Delta r/r)$ from the RAS definition.

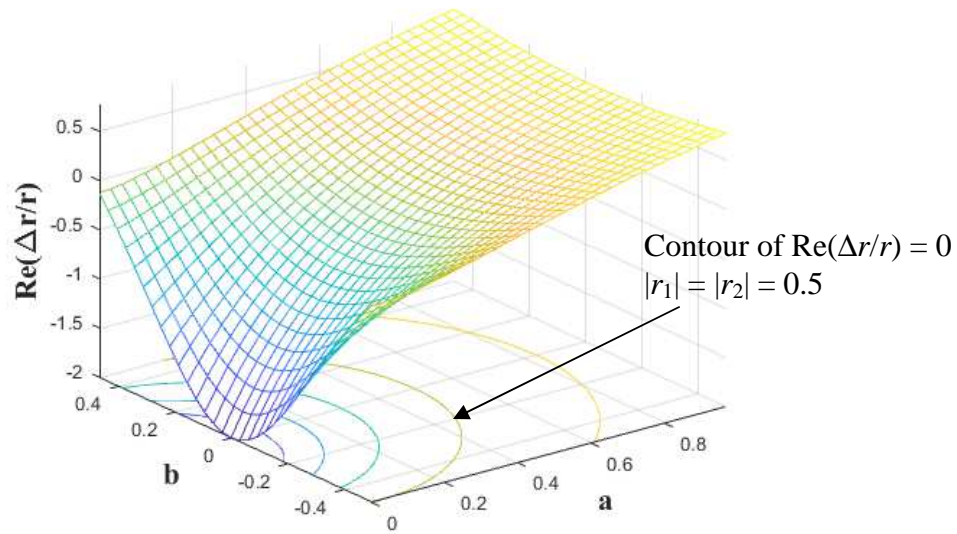


Figure 4.8 $\text{Re}(\Delta r/r)$ output from RAS definition, equation 3.4. For range of $a = 0$ to 1 and $b = -0.5$ to $+0.5$, c and d held constant at 0.5 and 0 respectively.

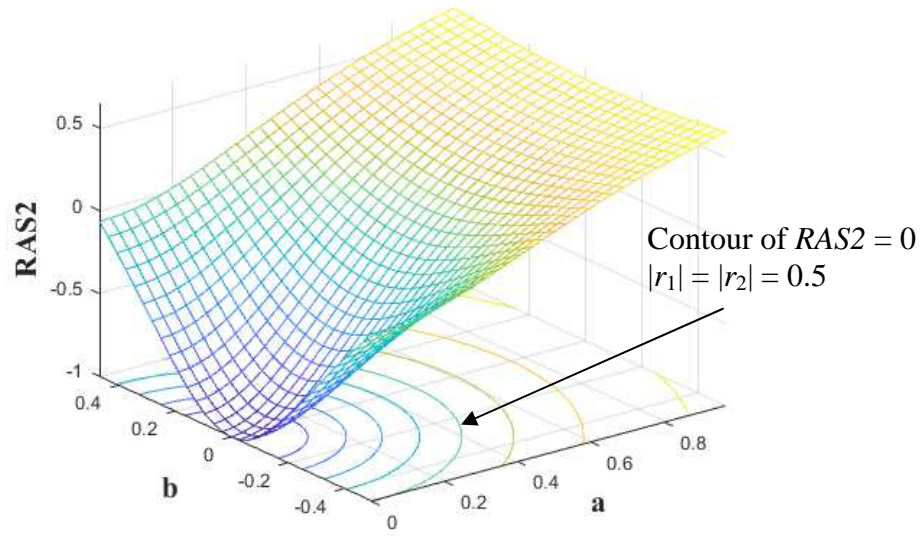


Figure 4.9 *RAS2* output from the simulation of the RAS instrument. For the range of $a = 0$ to 1 and $b = -0.5$ to $+0.5$, c and d held constant at 0.5 and 0 respectively.

4.4.2 $\text{Im}(\Delta r/r)$ compared to simulated *RAS1* from RAS instrument

The surface/contour plot in figure 4.9 shows the $\text{Im}(\Delta r/r)$ output that would be expected according to the definition of RAS, equation 3.4. This can be compared to the *RAS1* output from the RAS instrument simulation shown in the surface/contour plot in figure 4.10. The contour plots show that when $b = 0$, $d = 0$ both $\text{Im}(\Delta r/r)$ and *RAS1* are zero, and therefore close to this line $\text{Im}(\Delta r/r) \cong \text{RAS1}$. More generally equation 3.24 shows that $\text{Im}(\Delta r/r) = 0$ when the complex arguments of r_1 and r_2 , φ_1 and φ_2 respectively, are equal, i.e. $\varphi_\Delta = 0$.

At: $a = 0$ the $\text{Im}(\Delta r/r)$ value, figure 4.9, varies from -2 to +2 as b varies from +0.5 to -0.5, whereas for the simulated RAS instrument, figure 4.10, *RAS1* varies from -1 to +1, over the same values of a , b , c and d . Unlike the *RAS2* output it is the large differences between the imaginary components, b and d , that result in a discrepancy between the exact and simulated values of *RAS1* and $\text{Im}(\Delta r/r)$.

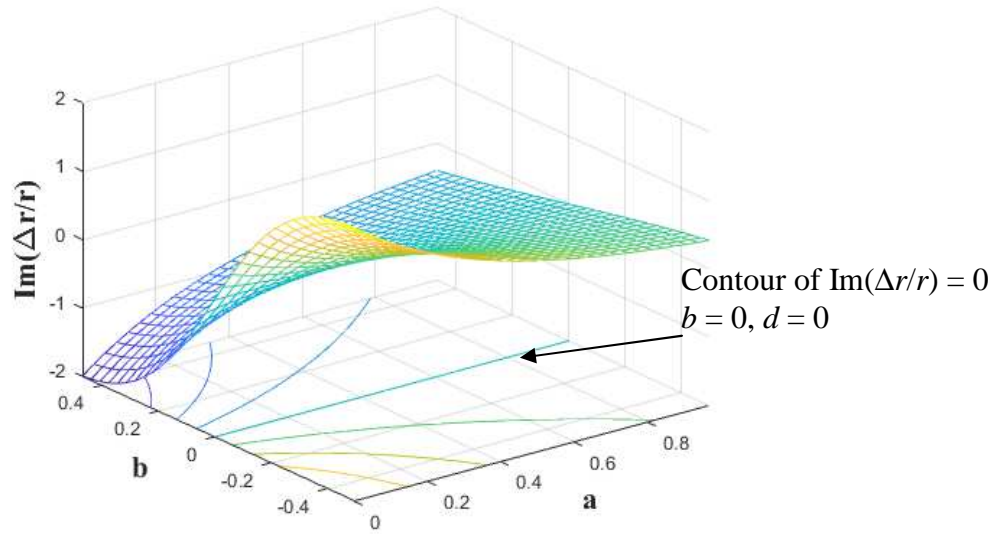


Figure 4.10 $\text{Im}(\Delta r/r)$ output from RAS definition, equation 3.4. For range of $a = 0$ to 1 and $b = -0.5$ to $+0.5$, c and d held constant at 0.5 and 0 respectively.

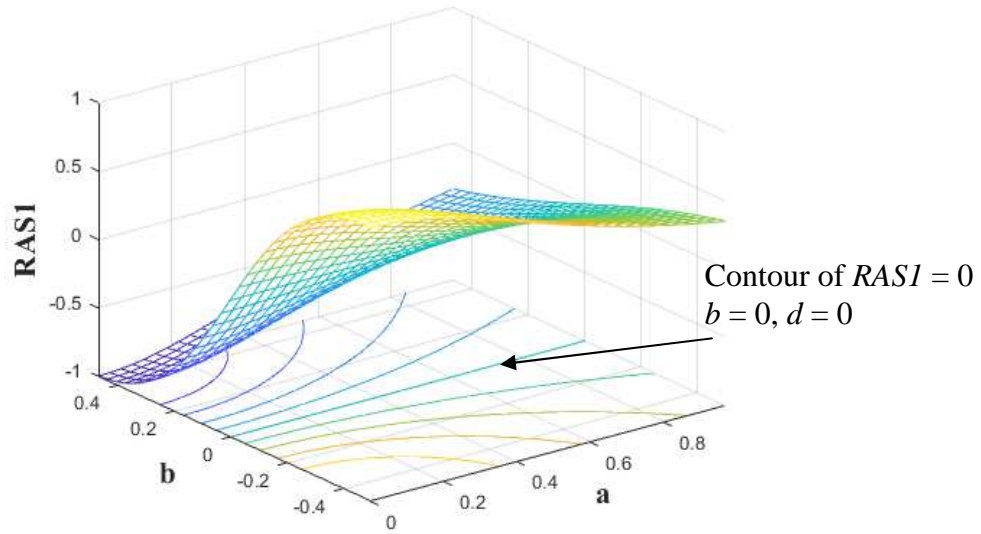


Figure 4.11 $RASl$ output from the simulation of the RAS instrument. For the range of $a = 0$ to 1 and $b = -0.5$ to $+0.5$, c and d held constant at 0.5 and 0 respectively.

4.5 Detector output as function of rotating sample

The results presented so far are for an instrument in the standard configuration where the sample is orientated at $\theta = 0.25$ rad. This section looks at the output from an instrument in which the sample rotates. The RAS definition (equation 3.4) is not defined for a sample in an arbitrary orientation; hence exact RAS values do not exist for a conditions other than the standard, $\theta = 0.25$ rad orientation. To avoid confusion

when the sample is rotated the term RAS is not used, instead *ADRAS1* and *ADRAS2* are used where, respectively, these correspond to the ωt and $2\omega t$ signals at the detector, see equations 3.61, 3.62, 3.63 and 3.64. Thus when the sample is rotated the output of the detector generates a waveform that, as a function of θ , contains components such as $\sin(2\theta)$, $\cos(2\theta)$, $\sin(4\theta)$ etc. Table 4.1 shows the components for each channel, I_{DC} , $I_{\omega t}$ and $I_{2\omega t}$. As with the results in section 4.4 and 4.5 above, a is varied from 0 to 1, b is varied from -0.5 to +0.5.

Harmonic	I_{DC}	$I_{1\omega t}$	$I_{2\omega t}$	ADRAS1	ADRAS2
DC	I_{DC-dc}	-	-	-	-
$\sin(2\theta)$	-	$I_{1\omega t-2\theta}$	$I_{2\omega t-2\theta}$	$ADRAS1_{2\theta}$	$ADRAS2_{2\theta}$
$\sin(4\theta)$	-	-	$I_{2\omega t-4\theta}$	-	$ADRAS2_{4\theta}$
$\cos(2\theta)$	$I_{DC-2\theta}$	-	-	-	-

Table 4.1 Rotation waveform component names, ‘-’ indicates not present. The columns are ordered according to PEM harmonic, the rows are ordered according to the rotation waveform harmonic.

To illustrate the effects of sample rotation on the detector output of the RAS instrument, a set of surface plots have been generated with each showing how a particular component of the rotation waveform varies as a function of the reflection coefficients. The rotation waveform components looked at are: I_{DC-dc} , $I_{DC-2\theta}$, $I_{\omega t-2\theta}$, $I_{2\omega t-2\theta}$ and $I_{2\omega t-4\theta}$. Where I_{DC-dc} is the mean of I_{DC} , $I_{DC-2\theta}$ is the $\cos(2\theta)$ component of I_{DC} , $I_{\omega t-2\theta}$ is the $\sin(2\theta)$ component of $I_{\omega t}$, $I_{2\omega t-2\theta}$ is the $\sin(2\theta)$ component of $I_{2\omega t}$ and $I_{2\omega t-4\theta}$ is the $\sin(4\theta)$ component of $I_{2\omega t}$. In addition the 2θ and 4θ components of the rotation waveforms generated by *ADRAS1* and *ADRAS2*, are calculated.

4.5.1 RAS instrument rotation waveform component I_{DC}

The I_{DC} value is constant with respect to the PEM phase, ωt , however it is not constant under rotation, *i.e.* in addition to a dc value it has a rotational waveform ($I_{DC-2\theta}$). This can be seen in equation 3.60. Assuming J_0 is zero the dc level of I_{DC} , which we call I_{DC-dc} , is equal to $(a^2 + b^2 + c^2 + d^2) / 4$, this is shown in figure 4.12. I_{DC}

also has a $\cos(2\theta)$ component, again from equation 3.60, which is called $I_{DC-2\theta}$ which has an amplitude equal to $(c^2 + d^2 - a^2 - b^2)/4$, shown in surface plot figure 4.13.

The implications from equation 3.60 are very important for we see that when $a = 0$, $b = 0$, $d = 0$ and $\theta = 0.5\pi$ rad (or 1.5π rad) then $I_{DC} = 0$. As I_{DC} is the denominator in the *ADRAS1* and *ADRAS2* it may seem that *ADRAS1* and *ADRAS2* would go to infinity, but as $\sin(2\theta)$ and $\sin(4\theta)$ also go to zero, *ADRAS1* and *ADRAS2* do not go to infinity. However when I_{DC} is at a low value it causes *ADRAS1* or *ADRAS2* to change rapidly causing the rotational waveform of the ADRAS values to generate higher harmonics other than the 2θ and 4θ terms. These higher order harmonics are not shown here, they may be present in some experimental setups.

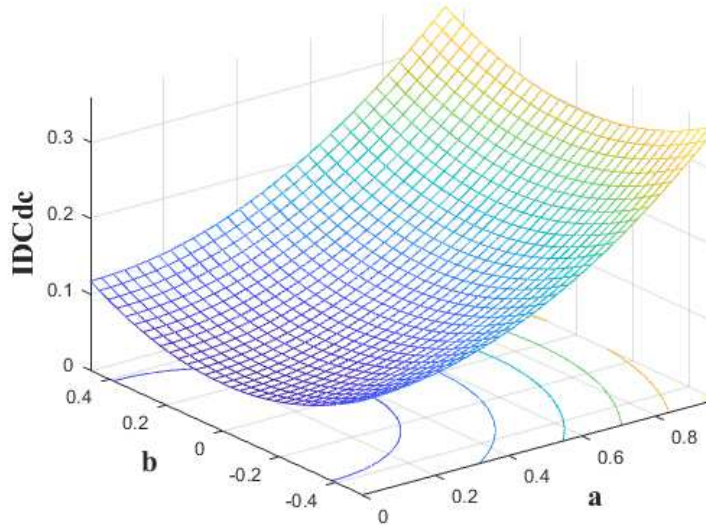


Figure 4.12 I_{DC-dc} , the mean value of I_{DC} over a complete sample rotation. For range of $a = 0$ to 1 and $b = -0.5$ to $+0.5$, c and d held constant at 0.5 and 0 respectively.

The surface plot in figure 4.13 shows $I_{DC-2\theta}$, this is the amplitude of the $\cos(2\theta)$ variation on I_{DC} caused by the rotation of the sample. The variation in I_{DC} with θ and reflection coefficients means that it must be taken into account when recording an ADRAS measurement.

4.5.2 RAS instrument rotation waveform component $I_{1\omega t-2\theta}$

There is only one rotation component of $I_{1\omega t}$ and that is, $I_{1\omega t-2\theta}$. The coefficient is

simply $(ad - bc)$ as inspection of equation 3.60 shows, the surface plot of which is a flat plane shown in figure 4.14.

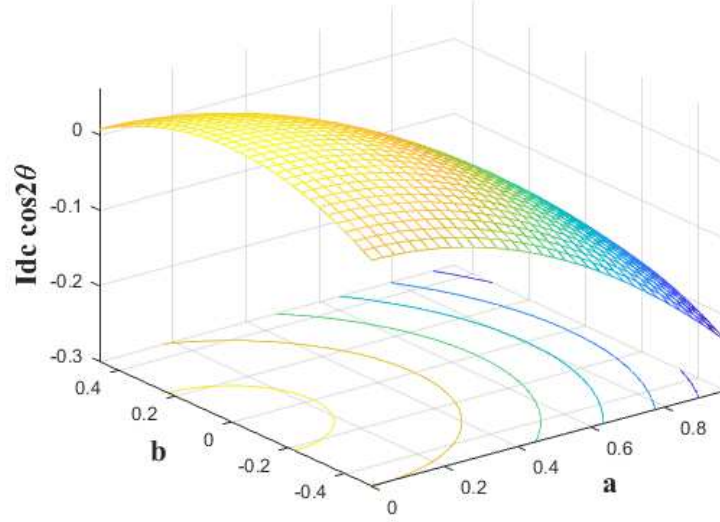


Figure 4.13 $I_{DC-2\theta}$ the amplitude of $\cos(2\theta)$ component of I_{DC} . For the range of $a = 0$ to 1 and $b = -0.5$ to $+0.5$, c and d held constant at 0.5 and 0 respectively.

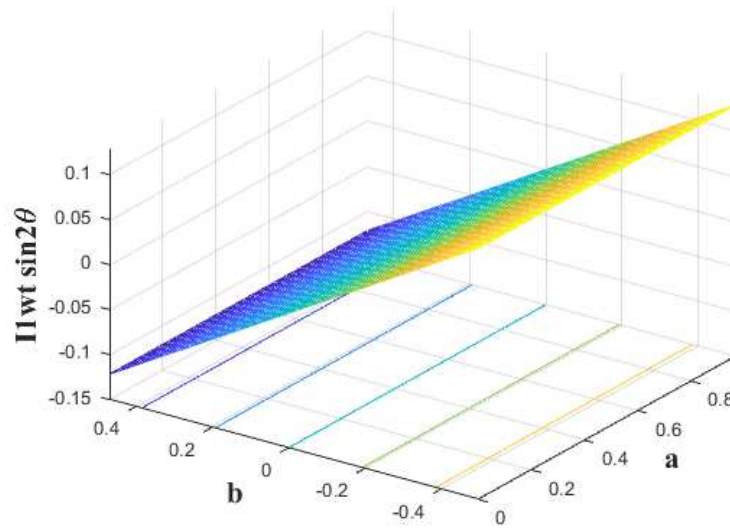


Figure 4.14 Surface plot of $I_{ac-2\theta}$. This shows the amplitude of the $\sin(2\theta)$ component of I_{ac} . For the range of $a = 0$ to 1 and $b = -0.5$ to $+0.5$, c and d held constant at 0.5 and 0 respectively. This surface is a flat inclined plane that is parallel to the a axis. It arises simply from equation 3.60 as d is zero and c is a constant $I_{ac-2\theta}$ is proportional to b .

4.5.3 RAS instrument rotation waveform components $I_{2\omega-2\theta}$ and $I_{2\omega-4\theta}$

The $I_{2\omega}$ output under sample rotation has two components: $I_{2\omega-2\theta}$ and $I_{2\omega-4\theta}$. The coefficients of the former are, from equation 3.60 equal to $(a^2 + b^2 - c^2 - d^2)$, this is the same as the numerator/2 for the real part of the RAS signal see equation 3.9. The $I_{2\omega-4\theta}$ term is the amplitude of the 4θ rotation waveform seen in the Ag near the plasmon resonance [44], as well as other materials. The coefficient of the $I_{2\omega-4\theta}$ term is, from equation 3.60, $((a - c)^2 + (b - d)^2)/8$. The 4θ coefficient is hence usually very small for low anisotropy samples as $a \cong c$ and $b \cong d$ this makes $(a - c)^2$ and $(b - d)^2$ both very small.

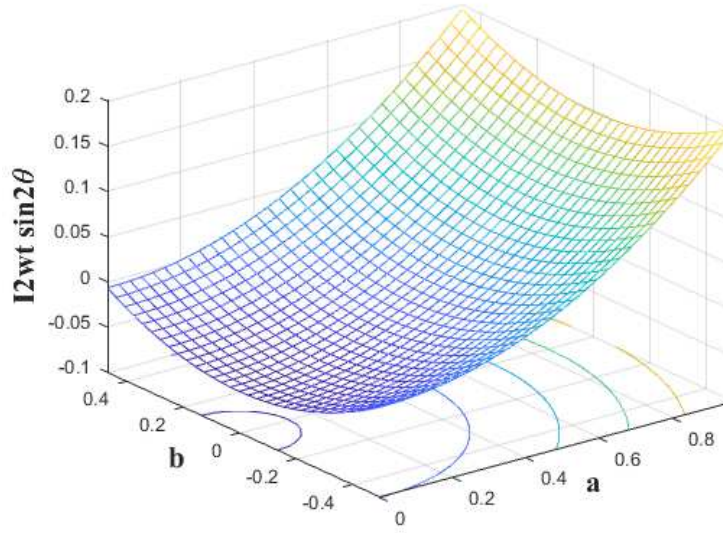


Figure 4.15 $I_{2\omega-2\theta}$, the amplitude of $\sin(2\theta)$ component of $I_{2\omega}$. For the range of $a = 0$ to 1 and $b = -0.5$ to $+0.5$, c and d held constant at 0.5 and 0 respectively. This shows the 2θ component of equation 3.64. The surface value is equal to $a^2 + b^2 - c^2 - d^2$, with $d = 0$ and $c = 0.5$, it is therefore a parabola which is proportion to $a^2 + b^2 + \text{constant}$, centred at $a = 0$ and $b = 0$.

4.5.4 RAS instrument ADRAS simulation

The RAS instrument components shown above are very interesting for analysis purposes but are not very useful for a practical instrument. A major benefit of the RAS/ADRAS definition is that the anisotropy is normalised to the overall reflectance of the sample. This normalisation eliminates spectral variation caused by the lamp, optics and detector. To make scientific use of the individual components such as $I_{1\omega}$ and $I_{2\omega}$ careful calibration would have to be carried out to ensure the RAS

instrument gave a flat spectral response. In addition, dynamic changes in light intensity (lamp flicker) may introduce errors or noise. For these reasons the rotational information gained from rotating the sample will, in practice, boil down to *ADRAS1* and *ADRAS2*.

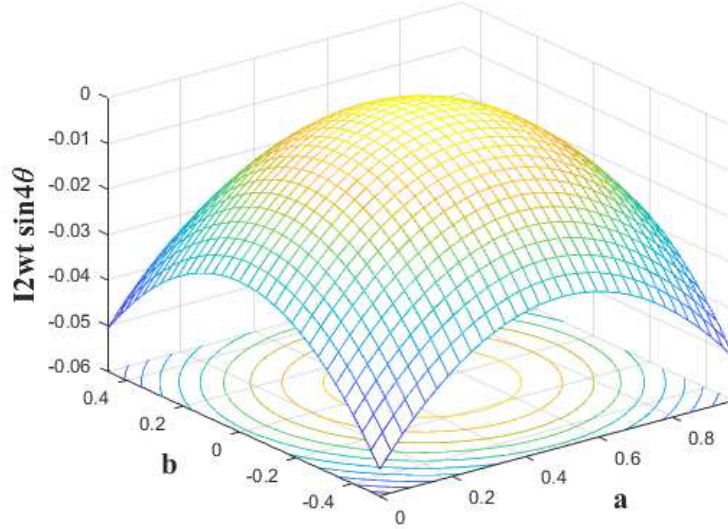


Figure 4.16 $I_{2\omega-4\theta}$, the amplitude of $\sin(4\theta)$ component of $I_{2\omega}$. For range of $a = 0$ to 1 and $b = -0.5$ to $+0.5$, c and d held constant at 0.5 and 0 respectively. This shows the 4θ component of equation 3.64. The surface value is proportional to $-(a - c)^2 - (b - d)^2$. With $d = 0$ and $c = 0.5$, it is therefore proportion to $-a^2 - b^2 + 0.5a - 0.25$. This makes it predominantly a negative parabola centred at $a = 0.5$ and $b = 0.5$.

An important distinction between ADRAS results and standard RAS results is that for the standard RAS the I_{DC} value is a proper dc value, which only changes when the sample properties change. When the sample is rotated I_{DC} takes on a $\cos 2\theta$ component, as I_{DC} is the denominator in the expression that describes both *ADRAS1* and *ADRAS2*, this $\cos 2\theta$ component can affect both *ADRAS1* and *ADRAS2* in a way that it not limited to normalisation. For low values of anisotropy the I_{DC} $\cos 2\theta$ component is very small, shown in equation 3.60, hence will only become relevant for large anisotropies.

The surface plots in figures 4.17 and 4.18 show respectively the amplitudes for rotation waveforms of *ADRAS1*_{sin2θ} and *ADRAS2*_{sin2θ}. Figure 4.19 shows the

equivalent for $ADRAS2_{\sin 4\theta}$. The value of these plots is that they provide a guide to how the anisotropy will determine the character of the rotation waveforms.

Whilst for low anisotropy samples $ADRAS1$ will have a single $\sin(2\theta)$ rotation component, $ADRAS2$ will have a $\sin(2\theta)$ and a $\sin(4\theta)$ rotation component. However under high anisotropy, $ADRAS1$ and $ADRAS2$ will have high order rotation waveform harmonics, which are a result of the $\cos(2\theta)$ component in I_{DC} .

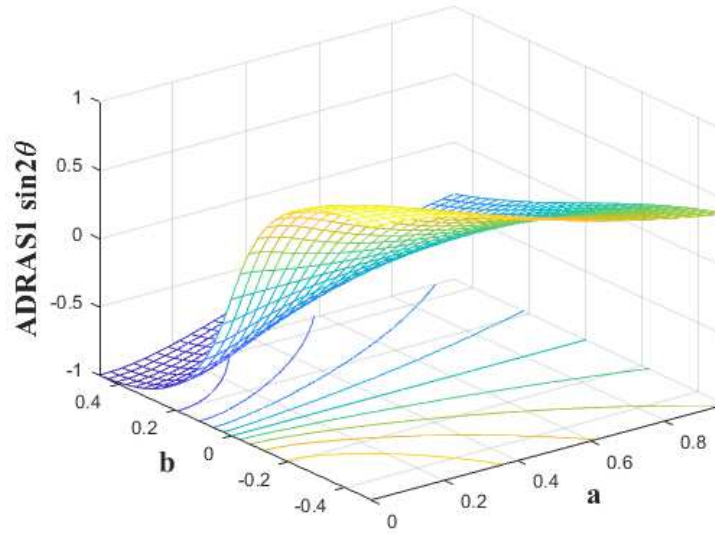


Figure 4.17 shows as a surface plot $ADRAS1-2\theta$, the amplitude of $\sin(2\theta)$ component of $ADRAS1$. For range of $a = 0$ to 1 and $b = -0.5$ to $+0.5$, c and d held constant at 0.5 and 0 respectively. This is described by equation 3.77. It shows that for low values of a , the $ADRAS1$ value is very sensitive to a change in the value of b . For high values of a , the output is not as sensitive to b .

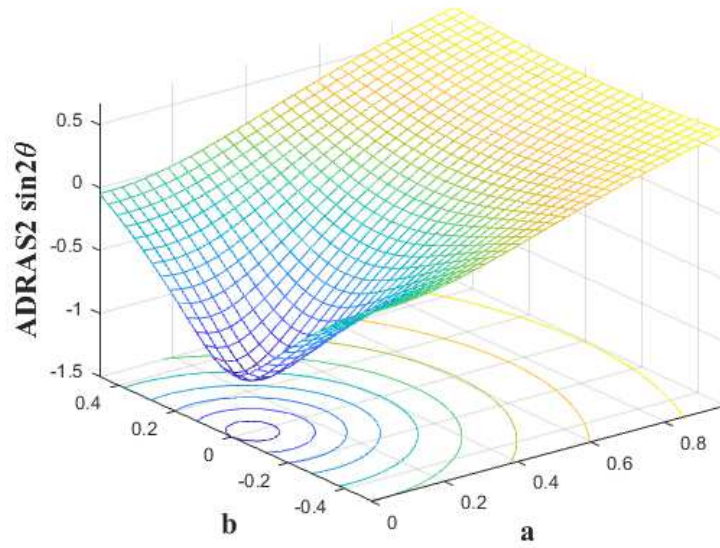


Figure 4.18 shows as a surface plot $ADRAS2-2\theta$, this is described by the amplitude of $\sin(2\theta)$ component of $ADRAS1$. For range of $a = 0$ to 1 and $b = -0.5$ to $+0.5$, c and d held constant at 0.5 and 0 respectively, see equation 3.78.

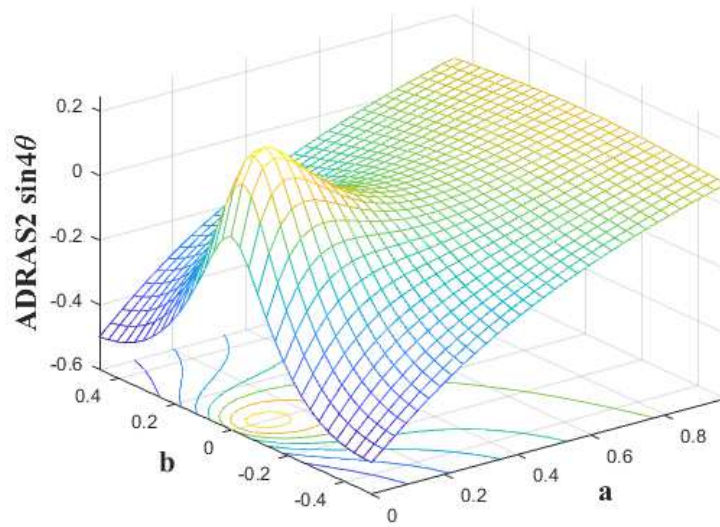


Figure 4.19 shows as a surface plot $ADRAS2-4\theta$, this is described by the amplitude of $\sin(4\theta)$ component of $ADRAS1$. For range of $a = 0$ to 1 and $b = -0.5$ to $+0.5$, c and d held constant at 0.5 and 0 respectively.

4.6 Conclusion

The objective of this chapter is to outline a way of simulating the RAS instrument. This is useful for a number of reasons, for example checking analytic models of the instrument to predicting how changes in components or samples may affect the output.

In section 4.2 the simulation was found to agree with the analysis in chapter 3 to an accuracy only limited by the floating point accuracy of the software. This is significant as the simulation simply breaks down the instrument into a number of modules, where the output of one module becomes the input to the next. The final simulation result from the lock-in amplifier agrees exactly with the analysis which involves the use of Bessel functions to describe the output. This agreement gives confidence that both the simulation and analysis were both done correctly. The simulator is far more adaptable than the analysis and can be used for studying the instrument in many different ways. The simulation could be expanded to look at the effect of imperfect components or imprecise setup. This may require the simulator to model partially polarised light, for example to study the influence of imperfect polarisers, in that case Stokes vectors and Mueller calculus would be required.

Within section 4.3 it was shown how the output of the RAS instrument compared to the definition of RAS in equation 3.4. This is illustrated in figures 4.4 and 4.6 respectively, the $RAS2$ to $\text{Re}(\Delta r/r)$ comparison and the $RAS1$ to $\text{Im}(\Delta r/r)$ comparison. This would help to establish the range over the instrument could be regarded as accurate.

The application of the simulator to rotation waveforms may help to explain some ADRAS experimental results, particularly where $ADRAS2_{\sin 4\theta}$ component is found, see section 4.5.8.

The simulation is very useful when the anisotropy is high and the I_{DC} value is low. For low anisotropy, I_{DC} is fairly constant and thus $ADRAS1$ and $ADRAS2$ will have the same components as $I_{\omega t}$ and $I_{2\omega t}$. Under high anisotropy, although the channel $I_{1\omega t}$ has only a $\sin(2\theta)$ component and $I_{2\omega t}$ has only $\sin(2\theta)$ and $\sin(4\theta)$ components,

this does not mean respectively that *ADRAS1* and *ADRAS2* also have only these components. I_{DC} will not be a dc value under rotation and may even go close to zero. A consequence of this is that both *ADRAS1* and *ADRAS2* may contain high rotation waveform harmonics not present in $I_{1\omega r}$ or $I_{2\omega r}$.

Chapter 5: Displaying ADRAS data

5.1 Displaying ADRAS data	87
5.1.1 Argand-type diagram	89
5.2 ADRAS of Ag(110)	90
5.2.1 Surface plots of Ag(110) ADRAS data	93
5.2.2 Ag(110) rotation data as a locus on an Argand-type diagram	94
5.2.3 Ag(110) aligning phase with sample anisotropy	96
5.2.4 Plotting ADRAS2 spectrum of Ag(110) as orthogonal components	97
5.3 Summary of Ag(110) ADRAS results	98
5.4 ADRAS of Au(110)	99
5.4.1 Au(110) rotation data as a locus on an Argand-type diagram	100
5.4.2 Plotting ADRAS2 spectrum of Au(110) as orthogonal components	103
5.5 Summary of Au(110) (1×1, (1×2) and (1×3) ADRAS2 results	107
5.6 Conclusion	108

5.1 Displaying ADRAS data

This chapter looks at the azimuthal-dependent reflection Anisotropy spectroscopy (ADRAS) data from two sets of published experimental results, the first using a Ag(110) sample [44], the second using a Au(110) sample, in an electro-chemical cell in which the surface can be made to adopt different surface structures: (1×1), (1×2) and (1×3) [45].

Azimuthally dependent reflection anisotropic spectroscopy (ADRAS) was introduced in chapter 3 to define the output of the RAS instrument when the sample orientation, θ , is arbitrary. The normal outputs of the RAS instrument with the sample having the standard orientation ($\theta = \pi/4$ rad) are denoted *RAS1* and *RAS2*, see section 4.1. These outputs are denoted *ADRAS1* and *ADRAS2* respectively when the sample has an arbitrary orientation. When the sample is rotated, *ADRAS1* and *ADRAS2* generate rotation waveforms. This means that the rotation data can be Fourier transformed to extract appropriate harmonic components. This greatly reduces the noise that is often generated while rotating the sample, mainly caused by the need to realign the beam during rotation. The phase information is also obtained which is much more accurate than relying on zero crossing points. This is illustrated in figure 5.1 in which Fourier transform ‘fits’ are overlaid on the rotational waveform data.

In section 3.6 the use of an offset angle was introduced, to allow for *ADRAS1* and *ADRAS2* spectra to be plotted against a common orientation angle θ_r , rather than θ which is defined as the angle between the eigenvector of r_I and the x direction. Typically θ_r may be set to an average value of θ or to θ at a particular wavelength. Whatever the value θ_r is set to, it means that the harmonics of the rotation waveforms will have a phase, ϕ , associated with them, see section 3.6. Thus the rotation waveforms listed in table 4.1 need to be expressed as vectors, if a physical orientation angle is used. For example the 2θ harmonic of *ADRAS1*, in table 4.1, is denoted *ADRAS1-2 θ* when the orientation is referenced to θ , however when the orientation is referenced to θ_r it needs to be denoted as a vector. Thus, for example,

the 2θ harmonic of *ADRAS2* is denoted ***ADRAS1-2 θ_r*** . The use of bold type face is to indicate vector quantity and θ_r denotes the physical reference angle.

Hence the rotation waveform harmonics can be expressed as a magnitude and phase or as orthogonal sine and cosine components. Returning to the examples above ***ADRAS1-2 θ_r*** has respective sine and cosine components which are denoted *ADRAS1-2 θ sin* and *ADRAS1-2 θ cos*; ***ADRAS2-4 θ_r*** has respective sine and cosine components denoted, *ADRAS2-4 θ sin* and *ADRAS2-4 θ cos*.

When experimental data is taken, the orientation angle may be completely arbitrary, this is denoted as θ_x which will have a constant offset to θ_r .

(It is often convenient to represent waveforms using complex notation. However it is deliberately avoided here to prevent confusion with ‘real’ and ‘imaginary’ parts of the RAS signal.)

The intensity of the RAS signal for these samples being studied in this chapter is of the order of 10^{-3} . For low anisotropies such as this, the theory in chapter 3 and the simulation in chapter 4 indicate that *ADRAS1* should have only DC and 2θ rotation harmonic components, with *ADRAS2* having only 2θ and 4θ harmonics see equations 3.79 and 3.80.

Unfortunately the *ADRAS1* data is not available for both of the published sets of data used in this chapter; hence only *ADRAS2* will be considered. *ADRAS2* consists of two components ***ADRAS2-2 θ_r*** and ***ADRAS2-4 θ_r*** . The full *ADRAS2* signal thus has a total of 4 components: *ADRAS2-2 θ_r sin*, *ADRAS2-2 θ_r cos*, *ADRAS2-4 θ_r sin* and *ADRAS2-4 θ_r cos*. Of these 4 components *ADRAS2-2 θ_r sin* is close to standard RAS spectra because it is the coefficient of the $\sin(2\theta)$ term in the expression for *ADRAS2* shown in equation 3.80, i.e., $\text{Re}(\Delta r / r)$. Hence *ADRAS2-2 θ_r sin* is the same as *RAS2* spectra for a properly setup RAS instrument. The *ADRAS2-2 θ_r cos* component highlights any anisotropy that is orthogonally to this. Note that because the rotation is a function of 2θ , then orthogonal in real space means an angle of $\theta = \pi/4$ radians.

The 4θ terms $ADRAS2-4\theta_{cos}$ and $ADRAS2-4\theta_{sin}$ represent the rotationally orthogonal functions of the $\sin(4\theta)$ term in equation 3.80, *i.e.*, $|\Delta r/r|^2$; illustrated in figure 3.2. For low anisotropy samples then usually $|\Delta r/r|^2 \ll \text{Re}(\Delta r/r)$ except when Δr is near zero.

The purpose of this chapter is to present the results in a different way to that already published to gain a different insight into the processes that are taking place. This is done in two different ways: as an Argand-type diagram and as separate orthogonal components. For the Ag(110) data the $ADRAS2-2\theta_{sin}$ and $ADRAS2-4\theta_{sin}$ is also plotted as a 3D surface plot.

5.1.1 Argand-type diagram

An Argand-type diagram can be used to plot the locus of the magnitude and phase of the ADRAS rotation waveforms as the wavelength of the light is scanned across the energy range. This reveals the net anisotropy at a particular wavelength, as a point on a 2D plane, with the direction of the anisotropy from the origin passing through the point. If the locus deviates from a straight line passing through the origin it shows that the anisotropy direction changes with wavelength. This is caused by the bandwidth of one dipole overlapping another, creating a change in anisotropy direction with wavelength.

The most obvious use of the Argand-type diagram is to reveal if the sample is orientated as expected. For ADRAS2 there are two Argand-type diagrams one for the 2θ component and one for the 4θ component. For the 2θ Argand-type diagram, a locus that moves up and/or down the vertical axis indicates that the sample orientation is setup as would be expected in the standard instrument, *i.e.* at $\theta = \pi/4$ radians. This is because the horizontal axis represents an orientation of $\theta = 0$ radians, whereas the vertical represents an orientation of $2\theta = \pi/2$ radians, *i.e.* $\theta = \pi/4$ radians. So if the sample has a net anisotropy which has an eigenvector at $\theta = \alpha$, then this would produce a line that is 2α to the horizontal axis. For the 4θ Argand-type diagram the vertical axis represents $\theta = \pi/4$ and an angle of $\theta = \alpha$, would produce a line of 4α to the horizontal axis.

5.2 ADRAS of Ag(110)

The output of the *RAS2* channel of a PEM-based RAS instrument was recorded where the sample, a Ag(110) crystal, was rotated through a series of steps from 0 to over 180 degrees, to acquire *ADRAS2* data. As shown in chapter 3 equation 3.80, if the anisotropy is low *ADRAS2* consist of two terms: a 2θ term and a 4θ term. Previous studies have shown [46] that RAS signals on the Ag(110) surface are very sensitive close to the 3.9 eV plasmon resonance.

Figure 5.1 shows the *ADRAS2* response around 3.9 eV at 3 sample wavelengths (Fourier transform ‘fits’ are overlaid on the rotational data). The 4θ response at 3.9 eV becomes very clear, using the expanded axis shown on the right hand side of the plot. The phase θ_x on the rotation waveforms, θ_r was defined to be zero when the *ADRAS2* signal was zero. Figure 5.2 shows the Ag(110) *ADRAS2* spectra for rotation angles of $\theta_x = 0, 15, 30, 45, 60, 75, 90, 105, 120, 135, 150, 165$ and 180 degrees.

The spectra shown in figure 5.2 are the raw *ADRAS2* spectra plotted for a range of sample orientation angles. The 2θ and 4θ fits of the rotation waveform, were made and plotted as spectra, respectively in figures 5.3 and 5.4.

The similarity between the raw *ADRAS2* rotation spectra (figure 5.2), and the *ADRAS2-2 θ_x* spectra (figure 5.3), is due to the dominance of the 2θ component in the rotation waveform. The *ADRAS2-2 θ_x* fits show a very precise common zero crossing point as well as common spectra peaks. This would suggest that the 2θ component of the rotation waveform does not have different anisotropy eigenvectors at different wavelengths. The *ADRAS2-4 θ_x* fits however do not show the same common zero crossing point or alignment of peaks, as is shown in figure 5.4. This suggests that the 4θ spectrum has more than one anisotropy eigenvector at different wavelengths.

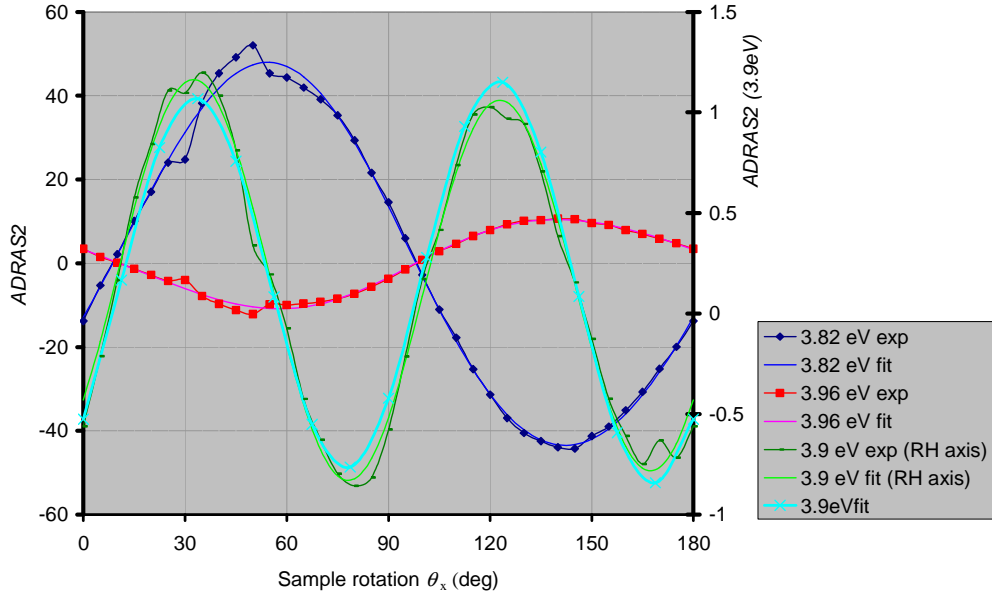


Figure 5.1. *ADRAS2* rotation waveforms for 3.82 eV, 3.90 eV and 3.96 eV, together with fits generated from ‘ 2θ ’ and ‘ 4θ ’ Fourier components. Note angle is expressed in θ_x degrees as recorded in the experiment.

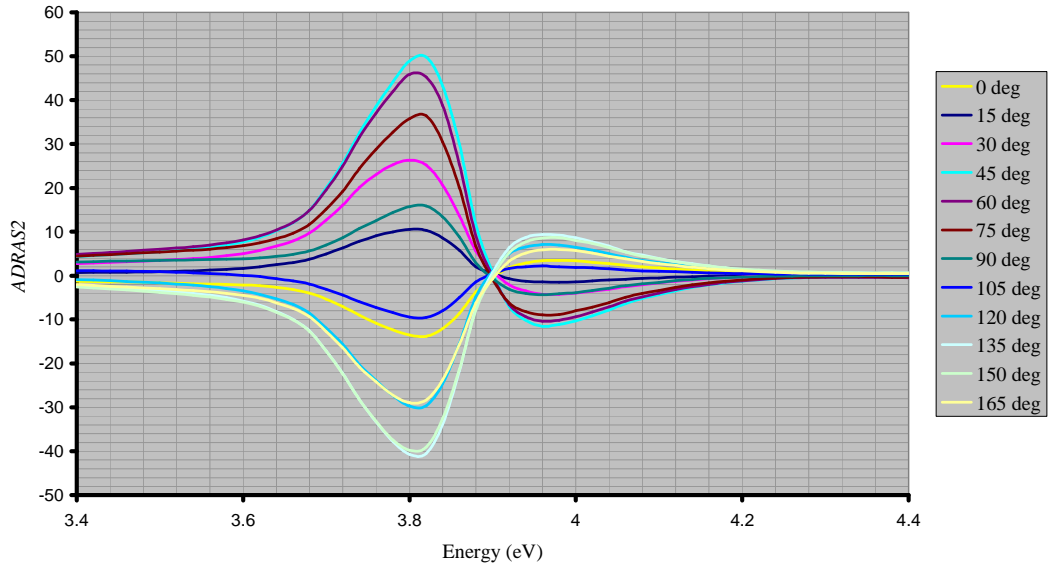


Figure 5.2 *ADRAS2* spectra from raw rotation data. Spectra plotted for rotation angles of every 15 degrees from 0 to 165. As the spectra repeat on and after 180 degrees, only spectra up to 165 degrees are shown.

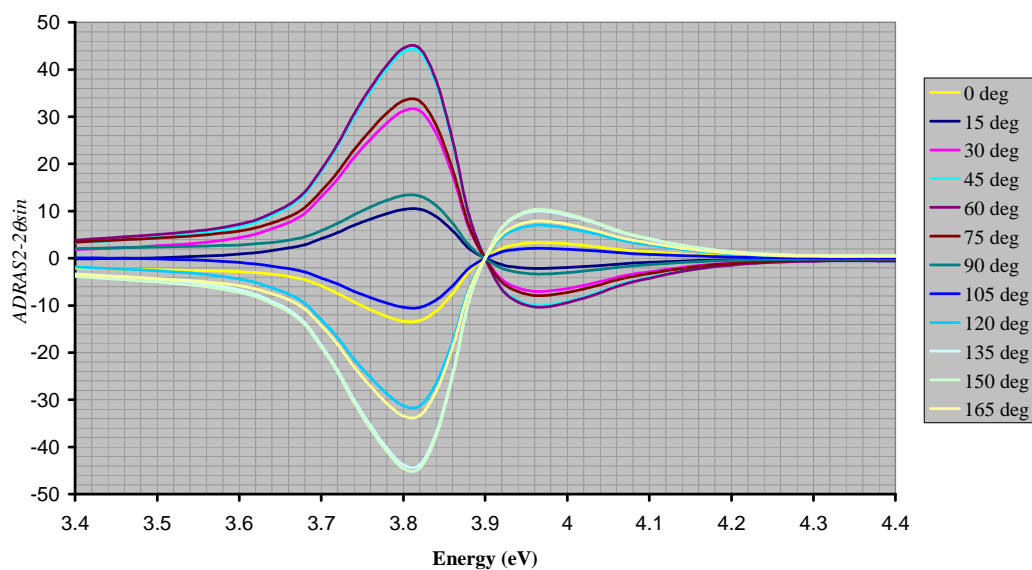


Figure 5.3 ADRAS2 spectra from 2θ fits to rotation data, plotted every 15 degrees from 0 to 165, corresponding to the raw data in figure 5.2. Note how the peaks in the spectra are all in line as well as the zero crossing point.

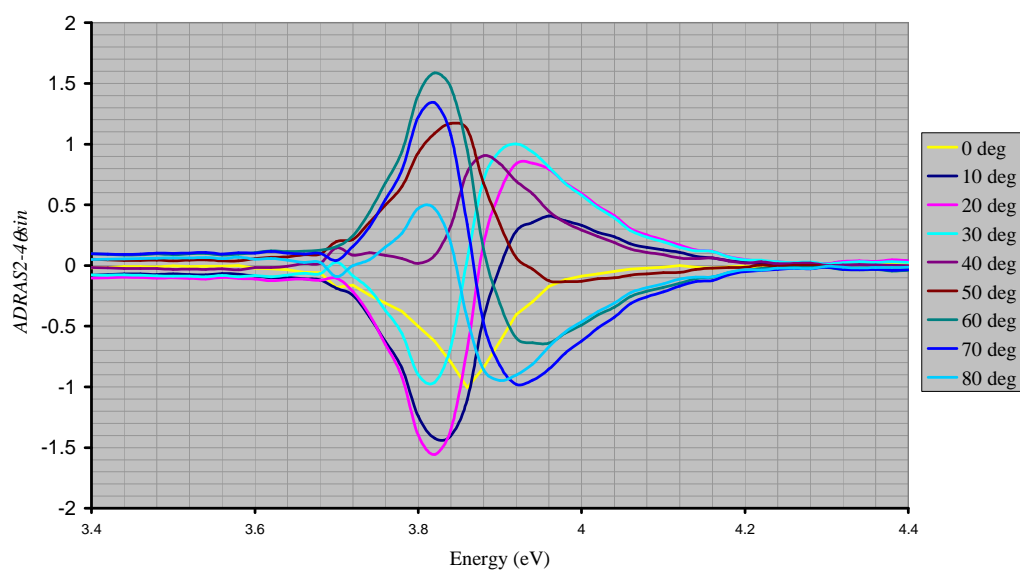


Figure 5.4 ADRAS2 spectra from 4θ fits to rotation data, plotted every 10 degrees from 0 to 90. Unlike the 2θ plot in figure 5.3 the peaks in the spectra don't line up and there is no common zero crossing point. As the spectra repeat on and after 90 degrees, only spectra up to 80 degrees are shown.

5.2.1 Surface plots of Ag(110) ADRAS data

A clearer picture of how the *ADRAS2-2 θ_x* and *ADRAS2-4 θ_x* spectrum changes with sample rotation can be seen by looking at the respective surface plots shown in figures 5.5 and 5.6. The surface plot in figure 5.6 shows clearly how the spectrum changes with sample rotation, with a large peak around 3.8 eV and a smaller peak around 3.9 eV occurring at different rotation angles. This would suggest that these peaks have different sources that have different eigenvectors.

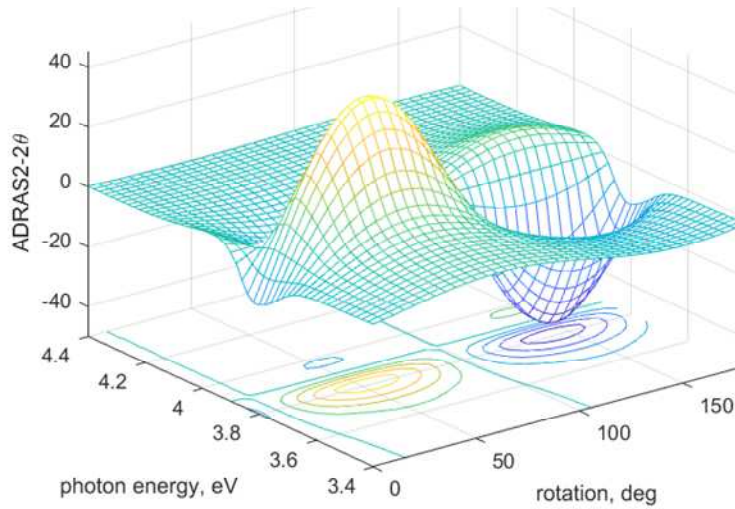


Figure 5.5 Surface and contour plots of *ADRAS2-2 θ_x* spectra. From the point of view of the ‘rotation’ axis it consists of a family of 2θ sinusoids, which change in amplitude but not in phase. From the point of view of the ‘photon energy’ axis it consists of a family of spectra, as figure 5.2.

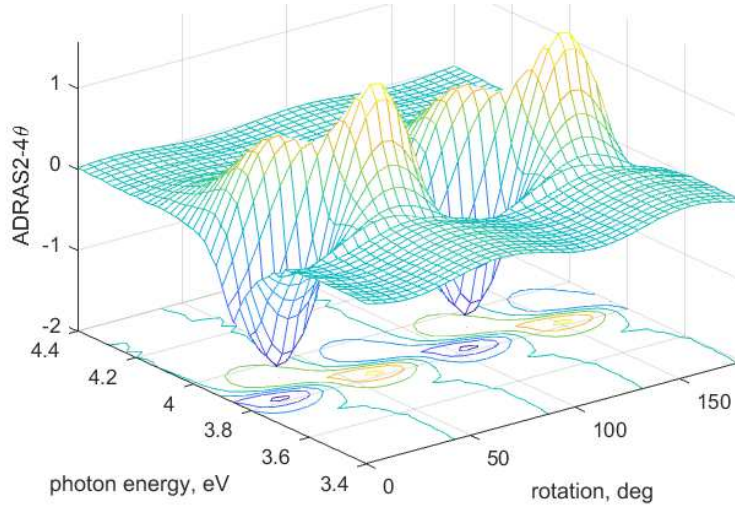


Figure 5.6 Surface and contour plots of *ADRAS2-4θ_x* spectra. From the point of view of the ‘rotation’ axis it consists of a family of 4θ sinusoids, which change in amplitude and phase. From the point of view of the ‘photon energy’ axis it consists of a family of spectra, as figure 5.3.

5.2.2 Ag(110) rotation data as a locus on an Argand-type diagram

Figure 5.7 shows the locus of the *ADRAS2-2θ_x* results, where the horizontal axis represents the *ADRAS2-2θ_xcos* component, and the vertical axis represents the *ADRAS2-2θ_xsin* component. The locus of *ADRAS2-2θ_x* clearly illustrates how the orientation of the anisotropy eigenvector varies with wavelength. It shows that the anisotropy lies close to a straight line, with a minor deviation around 3.4 eV. The rapid movement from 3.6 to 4.2 eV identifies the large peak in the spectrum, around 3.8 eV followed by a reverse peak around 4 eV. The deviation around 3.4 eV suggests a dipole acting away from the direction of the dominant anisotropy direction.

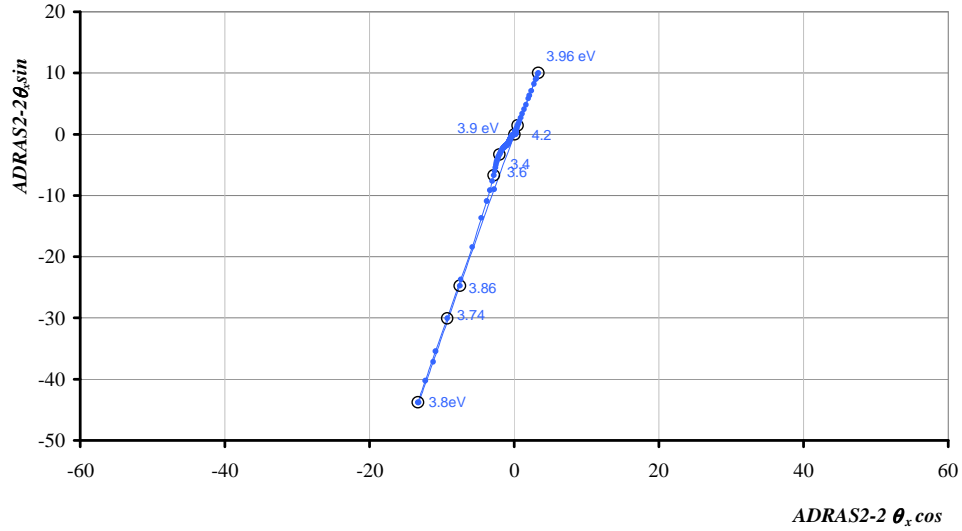


Figure 5.7 Locus of $ADRAS2-2\theta_x$ for Ag(110). θ_x represents the unaligned experimental values. This shows a sharp dominant anisotropy with a small deviation around 3.4 eV.

The locus of the 4θ Fourier magnitude and phase is shown plotted in figure 5.8, where the horizontal axis represents the $ADRAS2-4\theta_x \cos$ component, and the vertical axis represents the $ADRAS2-4\theta_x \sin$ component.

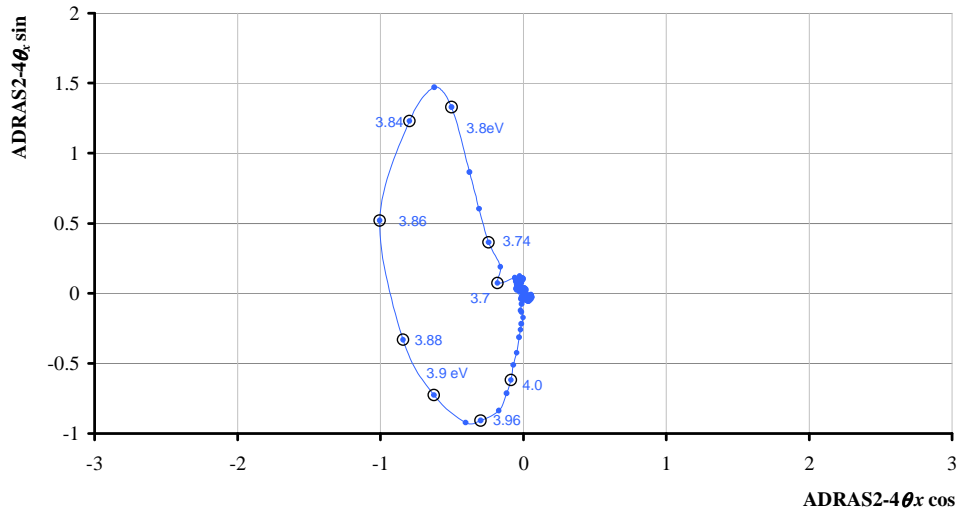


Figure 5.8 Locus of $ADRAS2-4\theta_x$ for Ag(110). θ_x represents the unaligned experimental values. Below 3.7 eV and above about 4.3 eV the magnitude of the $ADRAS2-4\theta_x$ is very small; between these figures the locus displays a large change in magnitude and phase.

5.2.3 Ag(110) aligning phase with sample anisotropy

Figure 5.9 shows the same data as figure 5.7 but with a phase shift (98.45 deg) added to θ_x such that the resulting $ADRAS2-2\theta_r$ rotation waveform at 3.8 eV is at a zero crossing point, this will correspond to the eigenvectors of the anisotropy at 3.8 eV being aligned and orthogonal to the x axis of the physical frame of reference at $\theta_r = 0$. This results in the magnitude of the $ADRAS2-2\theta_r$ signal at a maximum at 3.8 eV, when θ_r is at 45 degrees (the standard RAS instrument setup) which is represented by the vertical axis in figure 5.9.

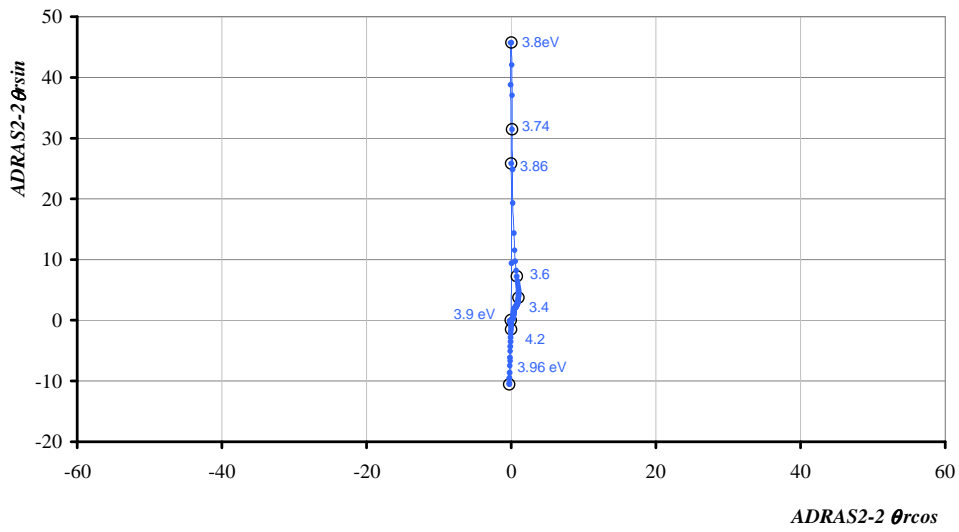


Figure 5.9 Locus of $ADRAS2-2\theta_r$ with the rotation reference shifted in order to show the dominant anisotropy in the standard orientation.

The locus of $ADRAS2-4\theta_r$ is shown in figure 5.10, with the same phase shift (98.45 deg) as the $ADRAS2-2\theta_r$ signal. The locus shows a large variation in both magnitude and phase from approximately 3.7 to 4.0 eV. Unlike the $2\theta_r$ locus, in figure 5.9, the $4\theta_r$ locus does not have a dominant anisotropy direction, and suggests the sources of the anisotropy are dipoles that are centred at different wavelengths but overlap, generating the elliptical shape between 3.8 and 4.1 eV; the plasmon resonance region. According to equation 3.80 the magnitude of $ADRAS2-4\theta_r$ should be equal to $|\Delta r|^2/|r|^2$. Figure 3.2 indicates that a change in $|\Delta r|^2$ is the result of phase and/or magnitude differences in reflection coefficients r_1 and r_2 . The magnitude is small apart from 3.7 to 4.1 eV which covers the plasmon resonance.

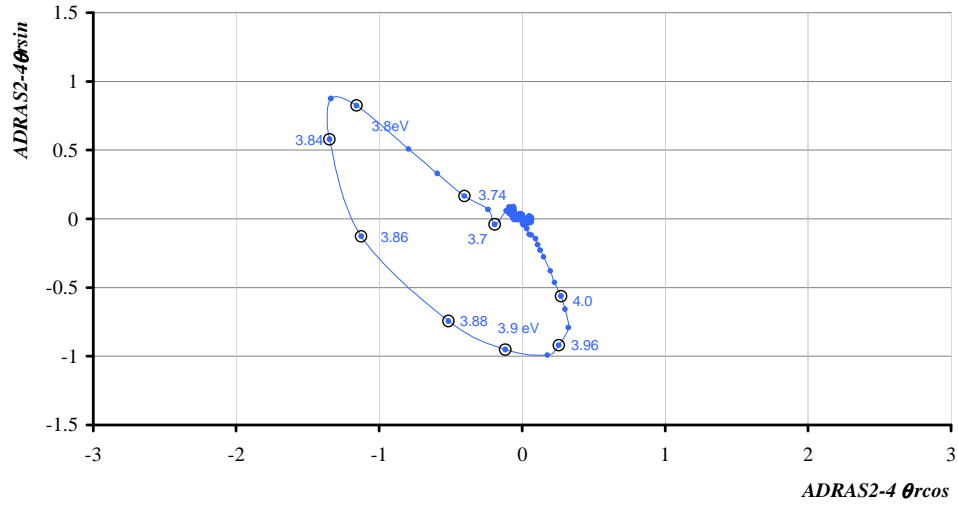


Figure 5.10 Locus of $ADRAS2-4\theta_r$ with the same rotation reference as figure 5.9. Unlike $ADRAS2-2\theta_r$ there is no dominant anisotropy direction. The magnitude is small apart from 3.7 to 4.1 eV which covers the plasmon resonance.

5.2.4 Plotting $ADRAS2$ spectrum of Ag(110) as orthogonal components

Here the $ADRAS2-2\theta_r$ signal and $ADRAS2-4\theta_r$ signal are each plotted as a spectrum as projected onto the orthogonal axes of the aligned Argand-type diagrams. We thus obtain the following 4 spectra: $ADRAS2-2\theta_r \cos$ and $ADRAS2-2\theta_r \sin$, plotted in figure 5.11; $ADRAS2-4\theta_r \sin$ and $ADRAS2-4\theta_r \cos$, plotted on figure 5.12.

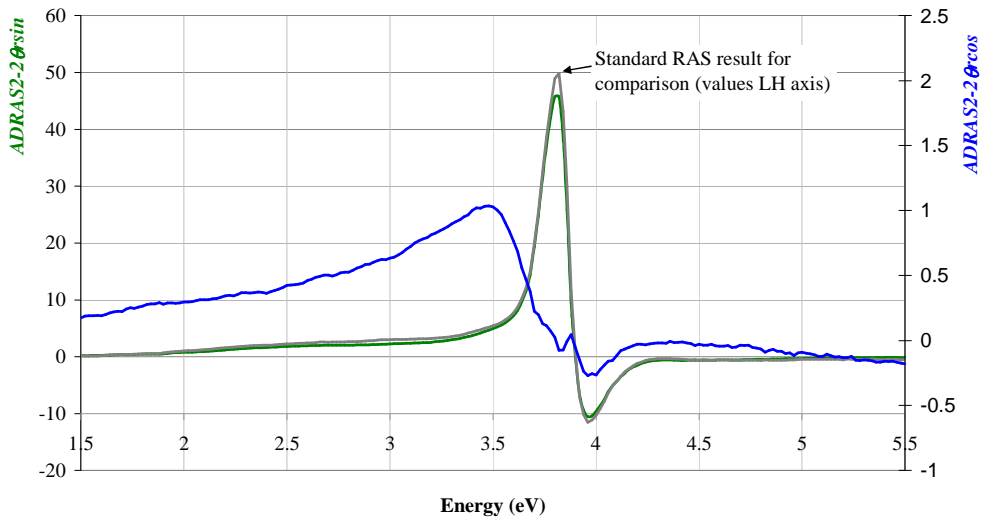


Figure 5.11 Spectra of $ADRAS2-2\theta_r \cos$ and $ADRAS2-2\theta_r \sin$ for Ag(110). The signal on $ADRAS2-2\theta_r \cos$ accounts for the deviation around 3.4 eV on the locus plot. The ADRAS data here has the same rotation reference as figure 5.9.

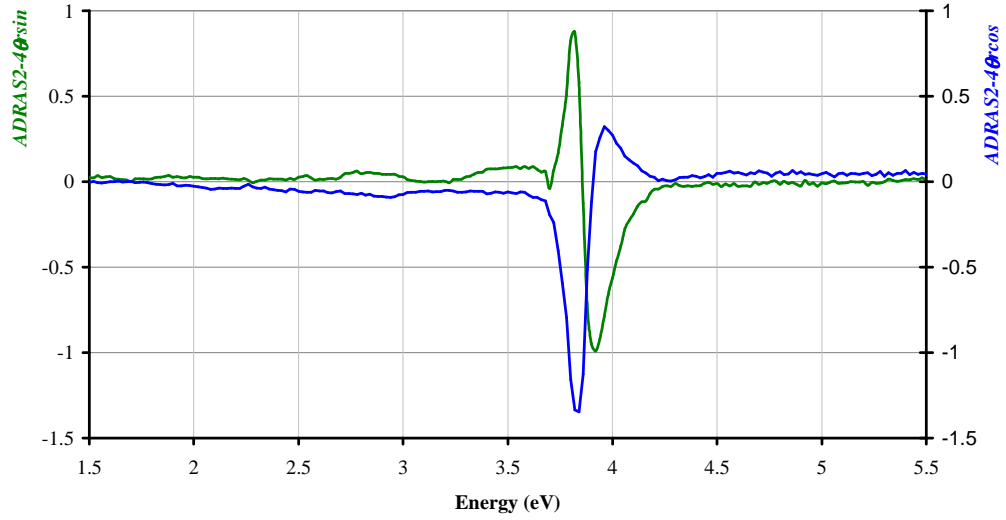


Figure 5.12 Spectra of $ADRAS2-4\theta_{cos}$ and $ADRAS2-4\theta_{sin}$ for Ag(110), using the same rotation reference as figure 5.9.

5.3 Summary of Ag(110) ADRAS results

The *ADRAS2* results from Ag(110) show a clear example of both 2θ and 4θ components in the *ADRAS2* rotation waveform. The Argand-type diagrams of figures 5.9 and 5.10 show how the phase of these rotation waveforms is wavelength dependent, both for the 2θ and 4θ cases.

When translated into spectra showing orthogonal components, as in figures 5.11 and 5.12, the presence of dipoles acting away from the Ag(110) principal axes become clear. In figure 5.11 where the *ADRAS2-2θ* spectra are shown, the *ADRAS2-2θ_{sin}* spectrum is near identical to the normal RAS signal. This is as would be expected as the sample is roughly aligned along the major direction of the anisotropy.

The orthogonal *ADRAS2-2θ_{cos}* spectrum however shows significant signal at 3.5 eV and below, which is not seen on the RAS signal, this shows the presence of dipoles acting in this region away from the major direction of the anisotropy; a feature not revealed in the original published results by Farrell *et al* [44]. This key observation demonstrates the power of displaying the data in this way. It is clear that a standard RAS instrument which is unable to show anisotropic orientation may give misleading results.

The **ADRAS2-4 θ_r** spectra shown in figure 5.12, as with the RAS and **ADRAS2-2 θ_r** spectra, show sensitivity around the 3.9 eV plasmon resonance. From equation 3.80 and figure 3.2 the **ADRAS2-4 θ_r** can be seen to be sensitive to a change in $|\Delta r|^2$, where Δr is the vector difference between the reflection coefficients r_1 and r_2 . Thus a magnitude or phase change in r_1 or r_2 would result in a change in Δr and hence a change in **ADRAS2-4 θ_r** . From equations 3.80 and 3.29, if the magnitudes of r_1 and r_2 are not changed then **ADRAS2-2 θ_r** will not change thus a change in **ADRAS2-4 θ_r** must be due to a phase change in r_1 or r_2 . This should be apparent on **ADRAS1** which is proportional to the phase change, for low anisotropy samples (see equation 3.33). Unfortunately **ADRAS1** is not available from this experiment.

5.4 ADRAS of Au(110)

This section presents a more detailed analysis of published data by Weightman et al [45] from the ADRAS of Au(110). By using an electrochemical cell the Au(110) surface can be made to adopt different surface arrangements; (1 \times 1), (1 \times 2) and (1 \times 3) [47]. As in the Ag(110) case above, the sample was rotated through a series of steps from 0 to over 180 degrees. Figures 5.13 – 5.15 show respectively, the Au(110) rotation data for the (1 \times 1), (1 \times 2) and (1 \times 3) surface arrangement, each displayed as a series of overlaid spectra. As with the Ag(110) data above (see figure 5.2) displaying the rotation data as a series of overlay spectra for selected sample orientation, or displaying rotation waveforms for selected photon energies, does not reveal any subtle effects. It is difficult using these figures to see how the amplitude and phase of the ADRAS varies with wavelength.

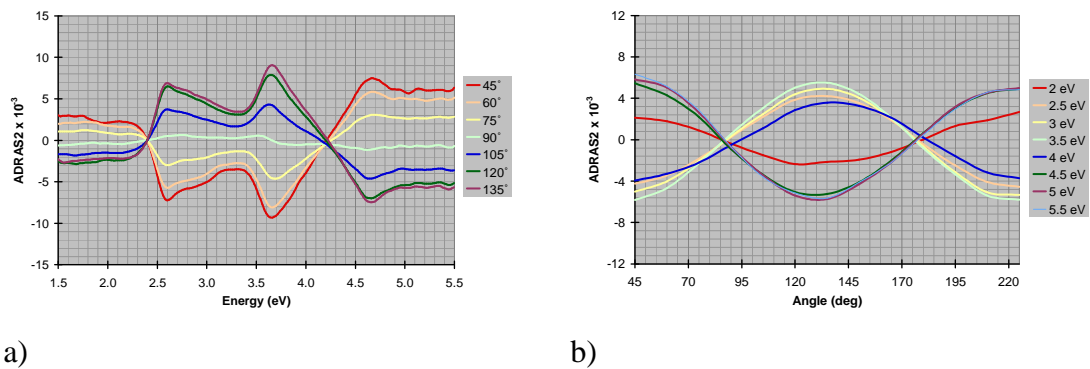


Figure 5.13 ADRAS of Au(110)-(1 \times 1), a) as function of energy, b) as function of wavelength

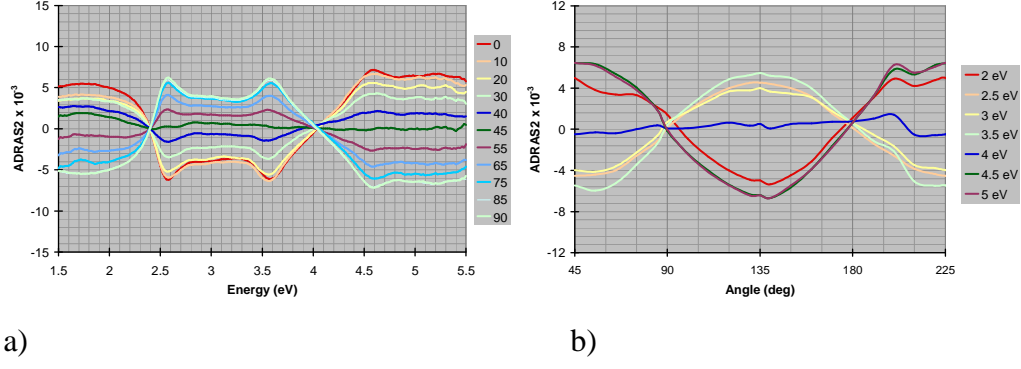


Figure 5.14 ADRAS of Au(110)-(1×2), a) as function of energy, b) as function of wavelength

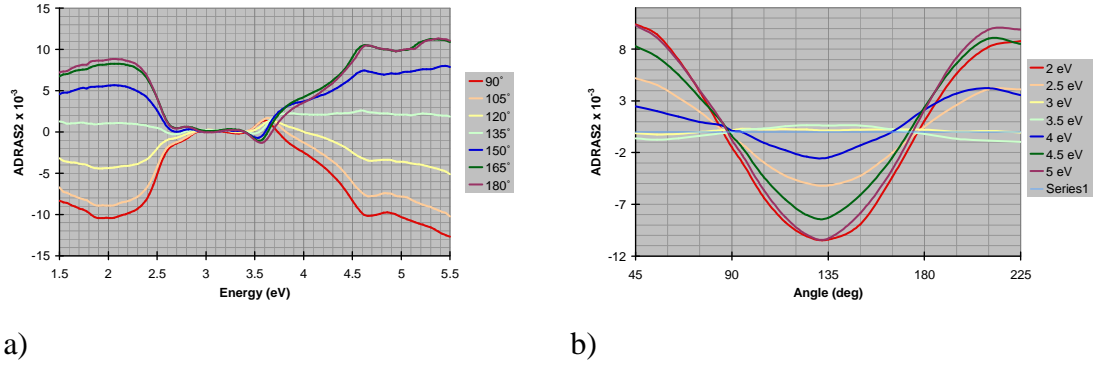


Figure 5.15 ADRAS of Au(110)-(1×3), a) as function of energy, b) as function of wavelength

5.4.1 Au(110) rotation data as a locus on an Argand-type diagram

Figure 5.16, 5.17 and 5.18 show loci from the Au(110) with the respective reconstructions (1×1), (1×2) and (1×3). With each figure consisting of, a) the $ADRAS2-2\theta_r$ locus and b) the $ADRAS2-4\theta_r$ locus. Note the vertical and horizontal scales on the plots are not equal.

All the loci are plotted with a common orientation reference θ_r , which was chosen to align $ADRAS2-2\theta_r$ locus in fig 5.16a (note expanded horizontal scale).

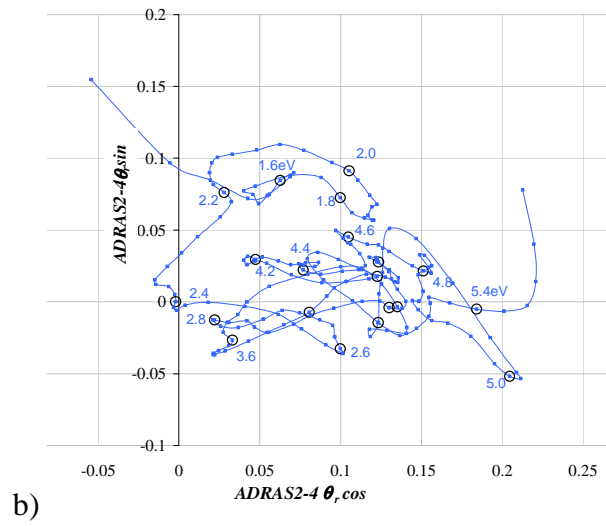
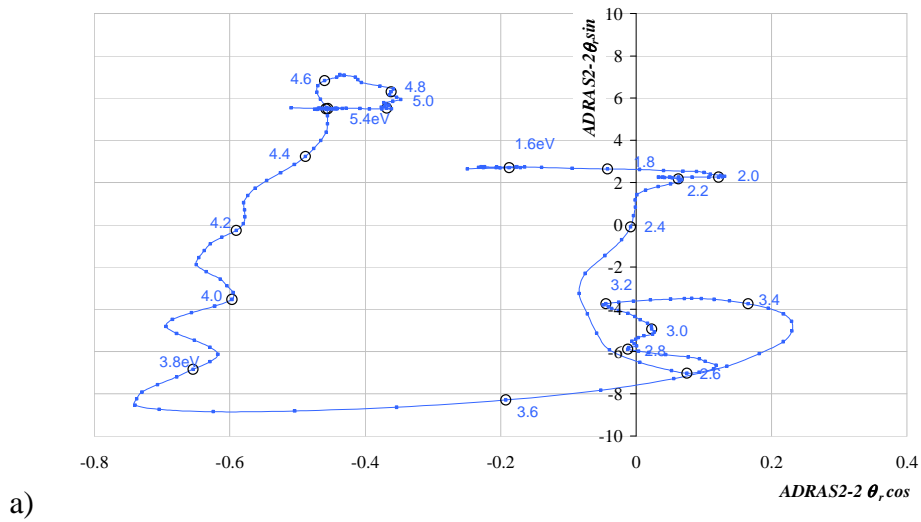


Figure 5.16 Loci of Au(110)-(1×1), a) **ADRAS2-2 θ** and b) **ADRAS2-4 θ** .

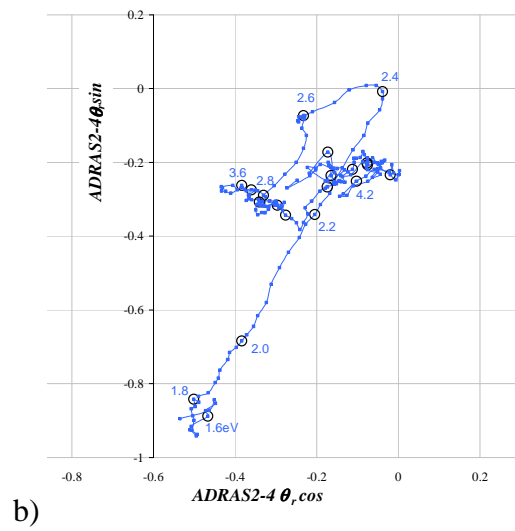
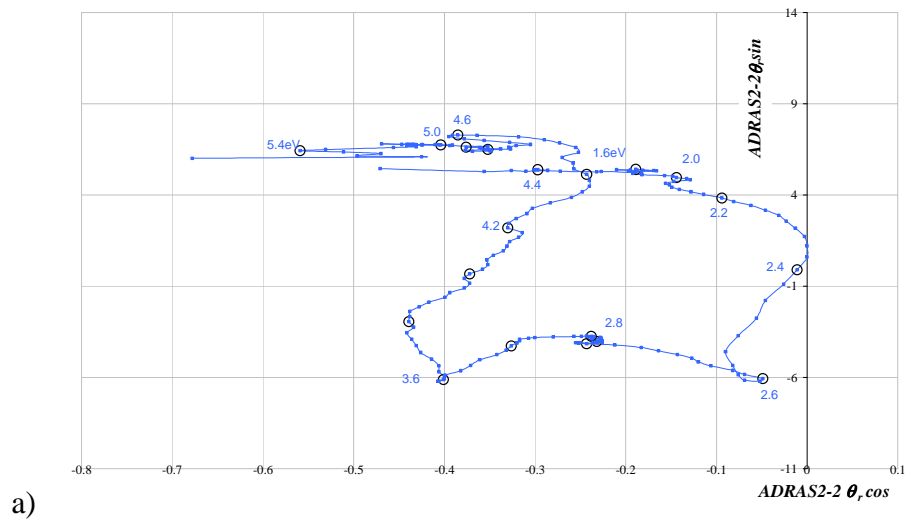
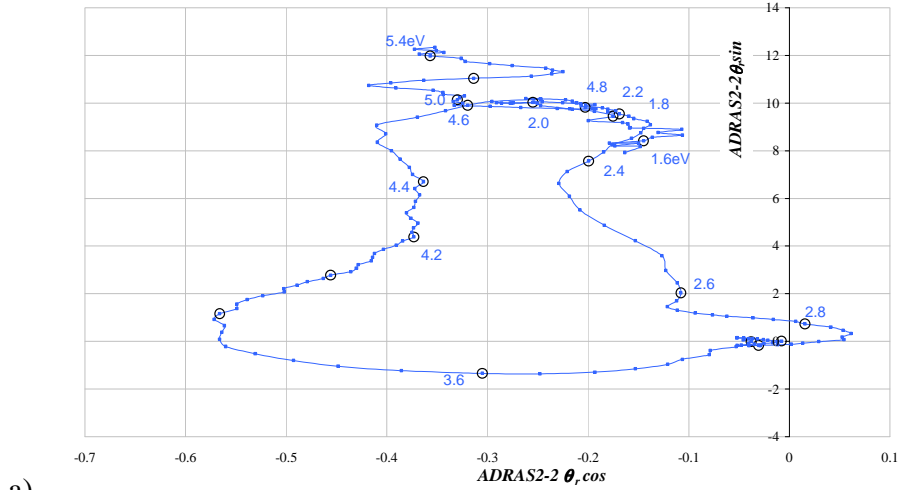
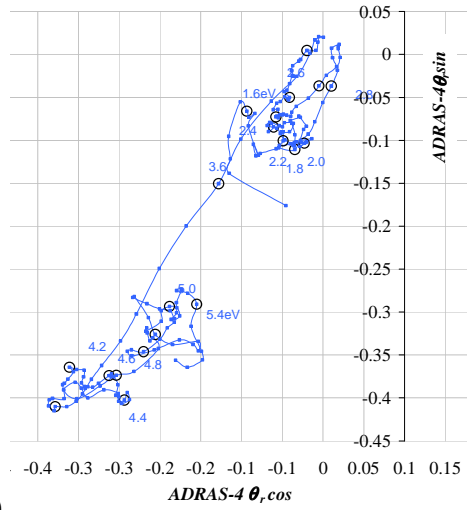


Figure 5.17 Loci of Au(110)-(1×2), a) $ADRAS2-2\theta_r$ and b) $ADRAS2-4\theta_r$.



a)



b)

Figure 5.18 Loci of Au(110)-(1 \times 3), a) *ADRAS2-2 θ* , and b) *ADRAS2-4 θ* .

5.4.2 Plotting ADRAS2 spectrum of Au(110) as orthogonal components

Figure 5.22 shows the *ADRAS2-2 θ , sin*, *ADRAS2-2 θ , cos* spectra for Au(110)-(1 \times 1) surface structure. Figure 5.23 shows the same spectra for Au(110)-(1 \times 2). Similarly figure 5.24 shows the plots for the Au(110)-(1 \times 3) reconstruction. The corresponding RAS signal is also plotted on all 3 plots. Figure 5.25 shows the corresponding 4 θ spectrums; 5.25a (1 \times 1), 5.25b (1 \times 2) and 5.22c (1 \times 3) reconstructions for Au(110).

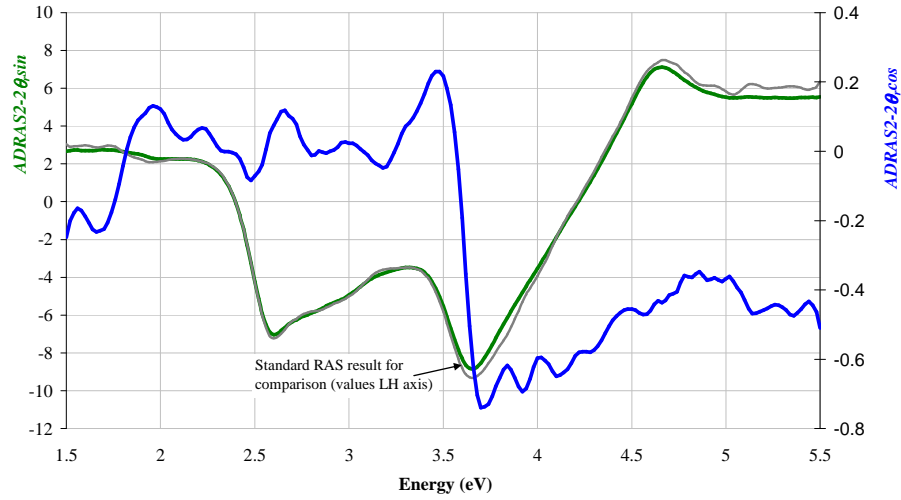


Figure 5.22 ADRAS2-2 θ_{sin} spectrum (green) and ADRAS2-2 θ_{sin} (blue), both for Au(110) 1 \times 1. The equivalent standard RAS spectrum is also included, shown in grey.

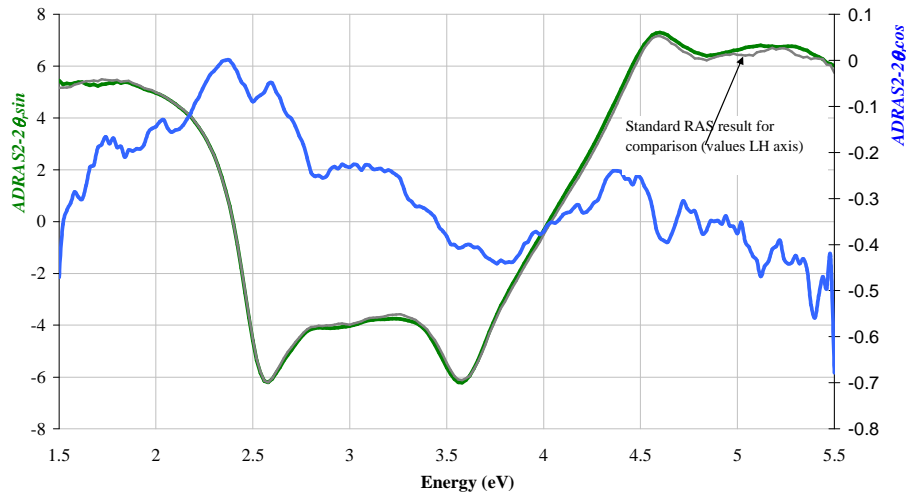


Figure 5.23 ADRAS2-2 θ_{sin} spectrum (green) and ADRAS2-2 θ_{cos} (blue), both for Au(110)-(1 \times 2). The equivalent standard RAS spectrum is also included, in grey.

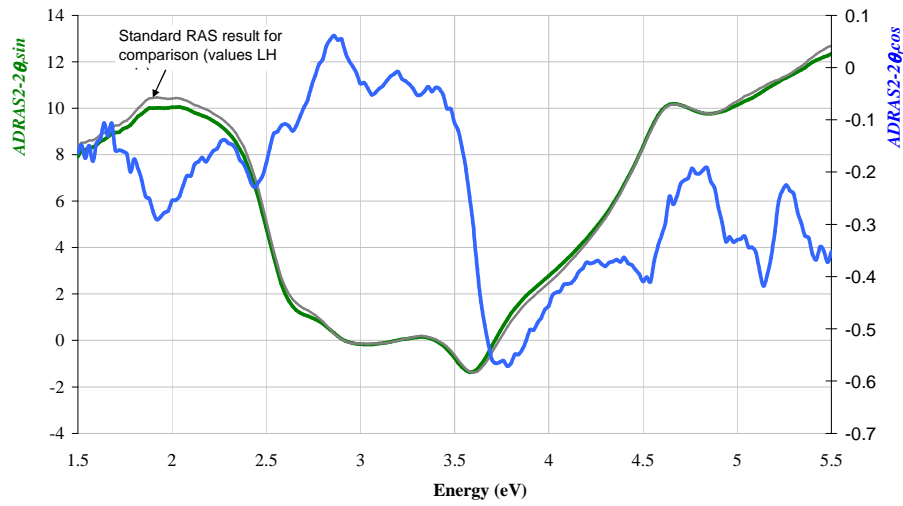


Figure 5.24 $ADRAS2-2\theta_{sin}$ spectrum (green) and $ADRAS2-2\theta_{cos}$ (blue), both for Au(110)-(1×3). The equivalent standard RAS spectrum is also included, in grey.

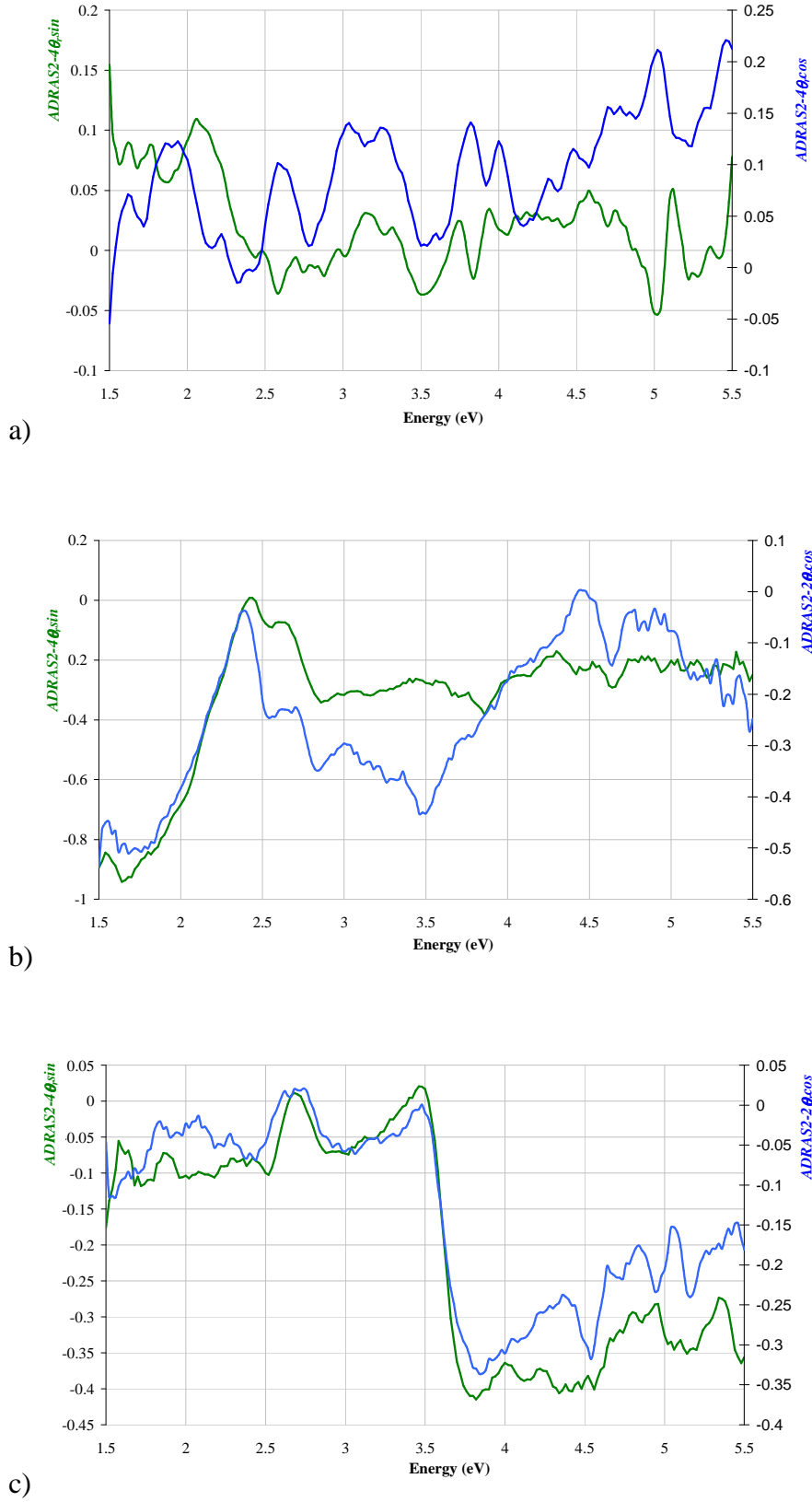


Figure 5.25 $ADRAS2-4\theta_{sin}$ spectrum (green) and $ADRAS2-4\theta_{cos}$ (blue), for a) (1×1), b) (1×2) and c) (1×3).

5.5 Summary of Au(110) (1×1), (1×2) and (1×3) ADRAS2 results

As with the Ag(110) sample in the first part of this chapter, the 2θ rotation data shows a dominant anisotropy for each surface structure: (1×1), (1×2) and (1×3). Figures 5.16a, 5.17a and 5.18a show the 2θ rotation data for the respective reconstructions (1×1), (1×2) and (1×3). These 3 locus plots show a small shift in the overall anisotropy between the reconstructions with the (1×2) (figure 5.17a) anisotropy orientation rotated in a negative angular direction and the (1×3) (figure 5.18a) shifted in a positive angular direction compared to the (1×1) (figure 5.16a). The (1×1) 2θ locus (figure 5.16a) is very interesting as it shows a shift in orientation between about 3.6 eV and 3.7 eV which remains for all higher photon energies. The shift is not apparent on the normal RAS spectrum so may be an indication of a feature not taken into account using normal RAS analysis. As mentioned above, using the same data, Weightman *et al* [45] noted a phase shift in the RAS (represented here as **ADRAS2- 2θ**) at an energy of 4.2 eV and suggest this arises from the (111) facets that feature on the surface of the (1×1) structure. The RAS is close to zero at 4.2 eV, which would have made a phase shift in the **ADRAS2- $2\theta_{cos}$** more easily visible in the RAS. Figure 5.22 shows the transition in **ADRAS2- $2\theta_{cos}$** to actually occur around 3.6 eV, where there is a peak in the RAS. The large value of the RAS signal would have hidden this from Weightman *et al* [45]. This energy is consistent with the observation by Sheridan [10] *et al* that the spectrum above 3.8 eV is known to be associated with the presence of surface steps.

Figures 5.16a, 5.17a and 5.18a show that the locus paths do not seem to be the result of random noise as although they are intricate, they are smooth. This suggests that they may be useful in identifying physical properties of the samples.

Figure 5.24 illustrating **ADRAS2- $2\theta_{cos}$** shows a step that occurs around the 2.5 eV and another step back around 3.6 eV. This makes an interesting comparison with the (1×1) case which has the 3.6 eV step down but not the 2.5 eV step up.

The **ADRAS2- 4θ** loci (figures 5.16b, 5.17b and 5.18b, show an interesting change as the reconstruction progresses from (1×1), (1×2) to (1×3). In the (1×1) surface

structure the *ADRAS2-4 θ* , has no clear direction with most of the points clustered near the origin. In the (1 \times 2) *ADRAS2-4 θ* , locus another cluster is formed around the -0.9, -0.5 coordinates, made up from energies below 2.0 eV. The *ADRAS2-4 θ* , locus for the (1 \times 3) reconstruction shows a bigger cluster away from the origin at around -0.25, 0.35 coordinates, made up from energies above 4.0 eV. The (1 \times 2)

5.6 Conclusion

Representing the ADRAS data in the novel way described in this chapter may allow for a better interpretation of the data. The use of loci on an Argand-type diagram would allow for accurate alignment and study of the direction of anisotropies.

The display of spectra that is orthogonal to normal RAS spectra shows evidence of dipole contributions aligned away from the principal axis used for the RAS.

The separation of 2θ and 4θ rotational components and the observation that they act at different parts of the spectrum, could provide important information about the presence of dipoles on the surface. The presence of a dipole acting orthogonally from the dominant dipoles on the Ag(110) surface, shown in figure 5.11, illustrates this point. In general together with the knowledge from chapter 3 on the RAS theory, the ADRAS technique should enable a much better analysis of surface properties, than RAS alone.

There is also the possibility of obtaining more accurate and lower noise RAS by extracting the $\sin 2\theta$ component in the *ADRAS2* data. Equation 3.80 shows that $\sin 2\theta$ component of *ADRAS2* is equal to $\text{Re}(\Delta r/r)$. Although the $\sin 4\theta$ component should be eliminated if the sample is orientated at $\pi/2$ rad, it is not always easy to do this especially if the eigenvectors of anisotropy are wavelength dependent. Also a $\sin 2\theta$ fit to the *ADRAS2* data may improve the signal/noise by also eliminating none $\sin 2\theta$ noise.

Chapter 6: Development of a fast RAS instrument

6.1 Review of fast RAS instrumentation	110
6.1.1 Multiplexed single lock-in design by Núñez-Olvera <i>et al</i>	110
6.1.2 Multi-channel lock-in design by Kaspari <i>et al</i>	111
6.1.3 Rotating compensator CCD readout design by Hu <i>et al</i>	112
6.2 Liverpool 16 channel fast RAS instrument version 1 (FRASv1)	113
6.2.1 Optical description	113
6.2.2 Electronic overview	114
6.2.3 Photo diode array and pre-amplification	115
6.2.4 Noise filtering	117
6.2.5 DC (r) section	118
6.2.6 AC (Δr) section	118
6.2.7 PC interface	119
6.2.8 Timing unit (AC path)	119
6.2.9 Multiplexer	120
6.2.10 AC calibration procedure	121
6.2.11 PEM retardation	121
6.2.12 Determination of retardation over spectral range	121
6.2.13 Wavelength Calibration	124
6.2.14 Electronic test and calibration	124
6.3 Experimental use of the FRASv1 16 channel fast RAS instrument	125
6.4 FRASv2 32 channel enhanced UV upgrade	126
6.4.1 Enhanced photodiode array	126
6.4.2 Read-out electronics	127
6.5 Experimental use of the Liverpool FRASv2 32 instrument	128
6.6 Summary	129

6.1 Review of fast RAS instrumentation

The aim of this chapter is to describe in detail two versions of fast RAS instrumentation developed at Liverpool; FRASv1 and FRASv2, together with a brief summary of other fast RAS instruments. FRASv1 is a 16 channel instrument; FRASv2 is an upgrade to a 32 channel device with enhanced UV.

In the conventional PEM RAS instrument, covered in the introduction, the time to complete a single spectrum necessitates scanning a monochromator. Also, it is normally necessary to pause the scan when taking a reading to integrate the signal in order to reduce the noise. This generally means that each spectrum can take several minutes to acquire.

To speed up the acquisition of spectra the obvious first consideration is to replace the monochromator with a dispersive element (*eg.* focusing grating) and a linear detector array. Each element of the array can then correspond to a different wavelength and so can potentially be read-out independently of other elements. We can then in principle read-out the whole spectrum in parallel. In practice the readout hardware/software may still impose some sequential process in the array read-out, for example when a charge coupled devices (CCDs) or multiplex systems are used, but this can be done much faster than mechanically stepping of a monochromator. Before describing the Liverpool fast RAS instrument an overview of other fast RAS techniques will be briefly reviewed. All the fast techniques share the fact that they all use a dispersive element and a linear detector array, the type of array and the readout will vary however.

6.1.1 Multiplexed single lock-in design by Núñez-Olvera *et al*

Núñez-Olvera *et al* [48] developed a design based on extending the standard Aspnes single channel PEM design by using a 32 element detector multiplexed to a single lock-in amplifier. By doing this, the designers have replaced the monochromator, and so avoided the time needed to change wavelength, while retaining the simplicity of the single channel design. The drawback is that the lock-in amplifier must integrate each channel in turn. In comparison to having 32 channels processed simultaneously, this design, in principle, would take at least 32 times longer to

achieve was used instead, then using digital signal processing (DSP) techniques in either hardware and/or software the same signal-to-noise performance as a 32 channel parallel system. It does however have the advantage that the PEM can be adjusted at each wavelength to give a uniform angular retardation, and so would not require the Bessel function correction of other designs (explained later in section 6.2.12).

The time taken to achieve a full spectrum with this design can be estimated by multiplying the time taken to read each individual channel by 32. Núñez-Olvera *et al* state the time taken to read each channel for the data illustrated consisted of, 6.6 ms to allow for channel shift noise to fade and 9 ms ‘logging time’ [48]. This results in each spectrum being acquired in 500 ms. This means that of the time needed to change channel (9 + 6.6 ms) only 9 ms is used to integrate the signal, or only 0.58 of the time is used. If we combine this with the fact that all other channels are idle then the available time used, compared to a parallel system is $0.58/32 = 1.8\%$. Compared to a parallel read-out this design requires more than 50x the time to achieve the same noise levels.

6.1.2 Multi-channel lock-in design by Kaspari *et al*

This design by Kaspari *et al* [49] uses a lock-in amplifier (Femto Messtechnik LIA-BV-150-H) for each channel. This has the advantage over Nunez-Olvera *et al* design in that multiplexing the signal into a single lock-in amplifier is avoided. Each lock-in is available in a Euro-card format that can be housed in a 19” rack. The outputs from the lock-in modules are digitised, together with the ‘DC’ signal from each channel using a multichannel ADC PC card.

Like other designs this approach needs to compensate for the wavelength dependence of the angular retardation generated by the PEM. The data from each channel should be of comparable quality to the standard single channel design although a larger number of channels will make for a bulky instrument.

The trend in lock-in design, in order to improve cost/performance ratio, from mainstream manufacturers, is to digitize the signal after initial amplification, and to

follow this by DSP techniques rather than analogue phase sensitive detection (PSD). These are now available with as many as 32 inputs per unit and also multiple units can be linked together to form large units with 100s of inputs [50]. This approach however is unlikely to result in a commercially viable product. Rather than use a multi-input DSP type lock-in amplifier, it would make more sense to use have a dedicated system to process the RAS signal after digitisation.

6.1.3 Rotating compensator CCD readout design by Hu *et al*

Unlike the designs listed above, this design by Hu *et al* [51] does not use a PEM, but a rotating compensator. A rotating compensator (RC) in its simplest form is a quarter-wave plate that can be rotated along the axis in line with the light beam. A linear polarised beam passing through the RC has its polarisation changed depending on the orientation angle of the RC. Depending on the rotation angle the output polarisation can be linear (in the same direction as the input), clockwise circular or anti-clockwise circular. In this way it behaves in a similar way to a PEM, except that a PEM oscillates at a high frequency (50 kHz) and can dynamically change its maximum retardation angle. This technique, like the PEM techniques described above, has the ability to detect both the real and imaginary parts of the RAS spectrum. The relatively slow and controllable operation of the RC makes it possible to readout large linear arrays, for each polarisation state.

This approach presents a number of technical challengers which Hu *et al* acknowledge and address. These include, most significantly, imperfections in the mechanically rotated achromatic quarter-wave compensator which necessitates a time consuming correction, called the ‘two-zone correction’ procedure. This involves the 90 degree rotation of the analyser between two subsequent measurements. Lamp fluctuations, which are mitigated in the PEM instrument also present problems.

An experiment was run to demonstrate the performance of the instrument. It took 11.25 seconds to record each spectrum. This suggests that this technique, at present at least, is not suitable for experiments that require higher speed spectra acquisition.

6.2 Liverpool 16 channel fast RAS instrument version 1 (FRASv1)

This is a detailed description of the Liverpool fast RAS instrument version 1 design (FRASv1) as published by Harrison *et al* [52]. It is a 16 channel fast RAS designed to operate with a PEM-based RAS. A signal averaging noise reduction technique applied over a number of PEM cycles can enhance the signal to noise ratio, as required, to acceptable levels, at the cost of reducing the spectra acquisition rate.

6.2.1 Optical description

Figure 6.1 shows the optical layout of version 1 of the fast RAS (FRASv1) instrument. As can be seen this is very similar to the standard Aspnes PEM design, with the monochromator replaced by a focusing grating and a photodiode array. In common with the Aspnes PEM design it is capable of measuring the real and imaginary components of the RAS, but uniquely compared to the other fast RAS designs, it measures these *simultaneously*. Like other designs, such as the multichannel lock-in design by Kaspari *et al*, there is a need to compensate for the wavelength dependence of the angular retardation generated by the PEM. This is dealt with in section 6.2.12.

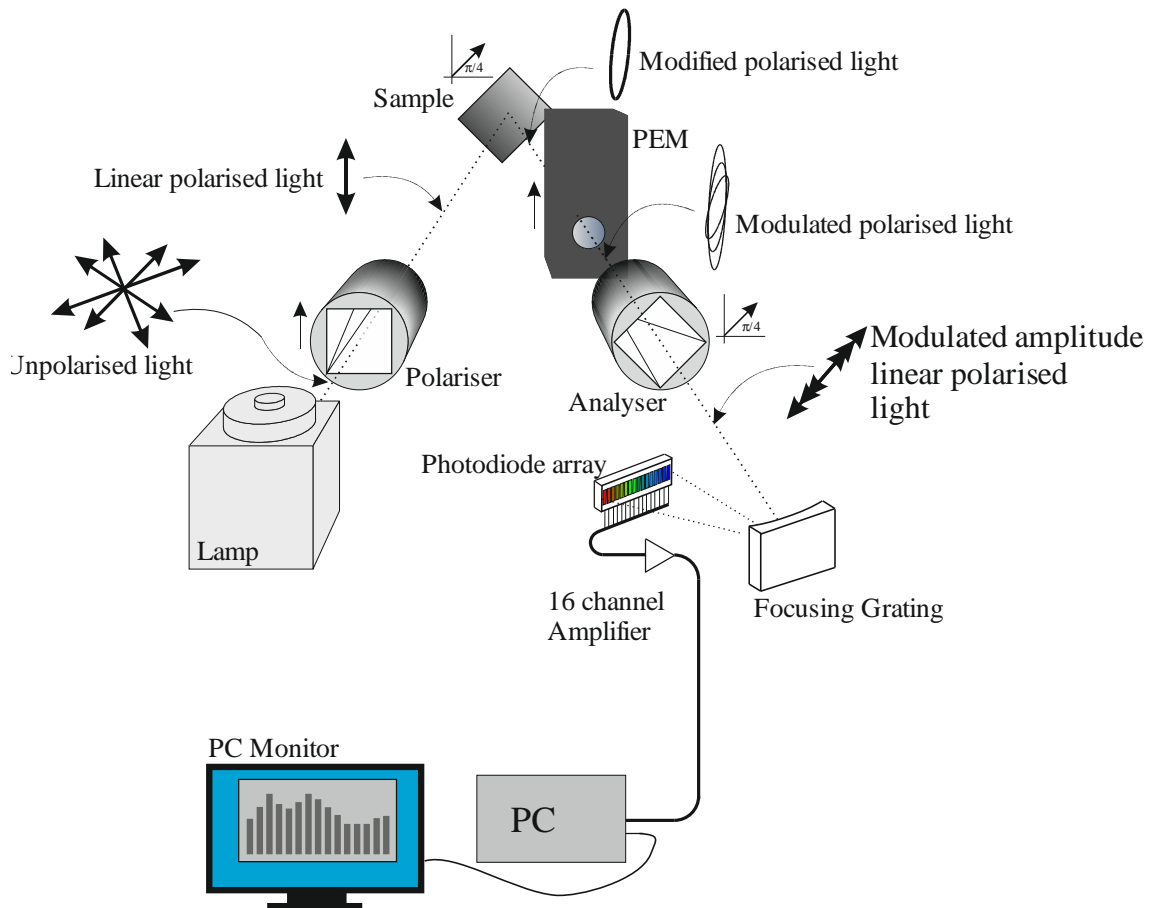


Figure 6.1 Optical layout of version 1 of the fast RAS (FRASv1) instrument

6.2.2 Electronic overview

Figure 6.2 shows the electronic system diagram of the fast RAS instrument. The detector is a IPL10220NW16 16 element PIN photo-diode array made by Thales Optonics. Use is made of a fast ‘flash’ analogue to digital converter to sample the AC component of each of the 16 photo-diode channels, 16 times over a PEM 20 μ s period, thus giving the ADC a maximum conversion rate of 12.8 MHz. This sampling is phase locked to the PEM to enable easy signal averaging by summing over a number of cycles. The ADC used was a Burr Brown (now part of Texas Instruments) ADS820, this flash converter is capable of operating at 40MHz whilst maintaining 8 bit integrity. By using a multiplexing technique it was thus possible read all 16 channels 16 times over the PEM cycle. This makes the data sampling rate $16 \times 16 \times 50 \text{ kHz (PEM frequency)} = 12.8 \text{ MHz}$, or 0.8 MHz per channel. This enabled a cheap and very compact instrument to be developed.

Equations 3.71 shows that to measure the real term of the RAS, $\text{Re}(\Delta r/r)$, the 2ω component needs to be extracted from the detected signal and equation 3.72 shows the imaginary part, $\text{Im}(\Delta r/r)$ requires the 1ω component. For the 50 kHz PEM this means extracting up to 100 kHz component. Using 16 point sampling over the PEM period puts the Nyquist frequency a comfortable 4 octaves above this. With appropriate filtering, at the pre-amp and AC amplification stages, the sampled data can represent a true continuous representation of the sampled signal.

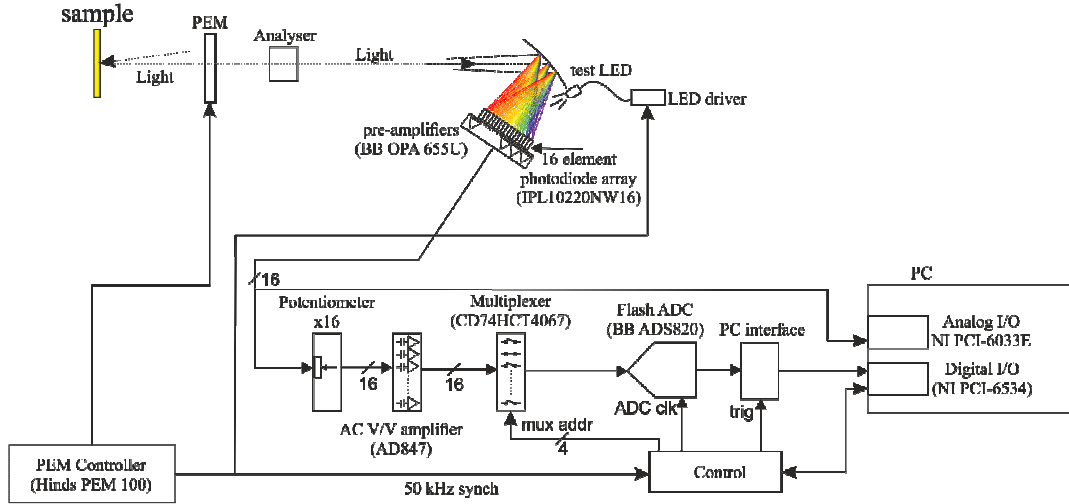


Figure 6.2 Electronics system diagram showing overview of 16 channel FRASv1 instrument.

6.2.3 Photo diode array and pre-amplification

The detector used, a IPL10220NW16, is a photodiode array. Photodiode current under normal operation is approximately proportional to incident light, the pre-amplifiers are therefore configured in a transimpedance mode (figure 6.3), so that the pre-amp output voltage is proportional to the photo-diode current and hence the incident light, *i.e.*.

$$V_o = I_{in} \times R_f \quad (6.1)$$

where V_o is the output voltage, I_{in} is the photo-diode current and R_f is the transimpedance feedback.

Pre-amplification of the photo-diode signals was done using Burr Brown OPA 655U FET input operational amplifiers. The use of surface mount components and the low component count (5 including decoupling capacitors) enabled a compact design that was low noise, resistant to interference and could be mounted close to the photodiode array in a screened box. A photograph of one of the ‘home made’ printed circuit board (PCB) modules of with 8 pre-amplifiers is shown in figure 6.4. The photodiode array was fully screened with just the active area exposed. Figure 6.3 shows circuit diagram for one of the photodiode channels.

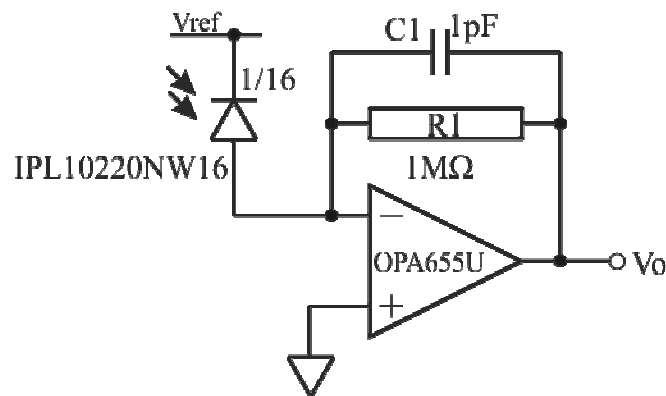


Figure 6.3 Circuit diagram of transimpedance pre-amplifier used for each photodiode. R_1 provides feedback to fix the gain over operation of 100 kHz. C_1 in parallel with R_1 provide roll-off after 100 kHz.

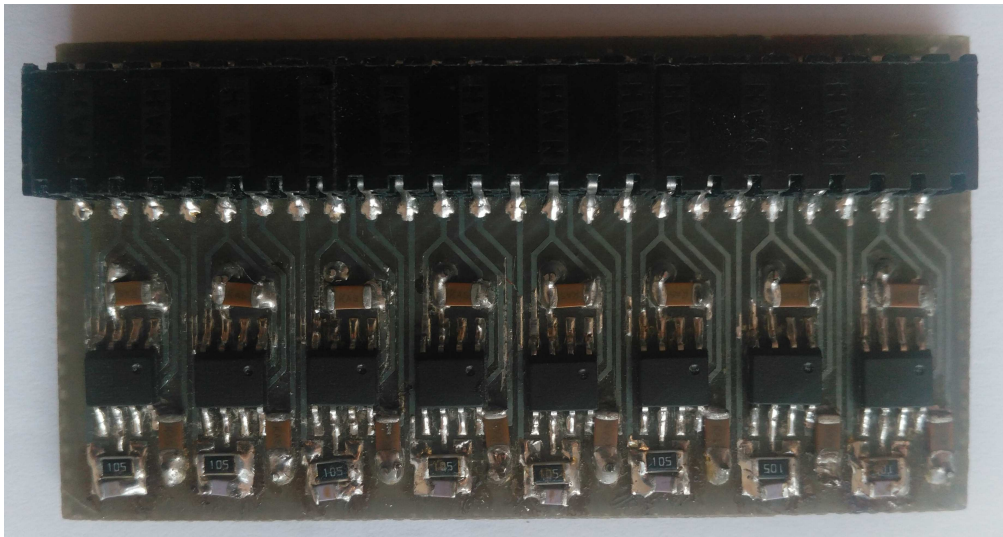


Figure 6.4 ‘Home made’ PCB module of 8 pre-amplifiers based around the OPA655U. Reverse side of printed circuit board is a continuous ground plane.

The feedback resistor R1 dictates the transimpedance gain over the operating frequency; in this case R1 has a value of 1 M Ω . Capacitor C1 in parallel with R1 provides a filter with a roll-off of 6dB/octave after 100 kHz (see noise reduction below). The OPA655U has a unity gain bandwidth of 400 MHz and so consequently the pre-amplifier gain is determined by C1 and R1. Figure 6.5 shows the amplifier gain between 10 kHz and 120 kHz. At 50 kHz, the PEM frequency of ω , the gain is 950 k Ω , at 100 kHz, 2ω , the gain is 847 k Ω . This difference in gain at, ω and 2ω , needs to be taken into account when comparing the real (2ω) and imaginary (ω) RAS values. After the pre-amp the signal is far less sensitive to interference, which means the photo-diode head can be mounted remotely from the rest of the electronics. At this stage the signal is divided into two paths, the DC path is connected to an ADC card in the PC to measure the r or 'DC' value of each channel, the other, 'AC' path goes to the Δr or AC section.

6.2.4 Noise filtering

Without filtering at the pre-amplifier stage a multiplex design suffers from a lower signal-to-noise than a non-multiplexed system because there is less time for each channel to integrate the signal and average out the high frequency noise. In a 16 channel multiplexed system, such as this, the signal would be sampled 16 times less than a true parallel system, giving a 4 times inferior signal-to-noise. In this design by using a high sampling rate, of 8 MHz per channel, much greater than the maximum signal of 100 kHz, the input can be filtered *before* the multiplexing, thereby reducing the noise at the sampling frequency. The gain of the pre-amplifier is equal to the impedance of R1 in parallel with C1, so the noise reduction can be calculated

$$G = \frac{R(1/2\pi fC)}{R + (1/2\pi fC)} \quad (6.2)$$

where G is the transimpedance gain of the pre-amplifier in Ω , R is the resistance of R1, C is the capacitance of C1 and f is the frequency.

For f at 100 kHz, G = 847 k Ω

For f at 8 MHz, G = 20k Ω

Hence the filter reduces noise by factor of $847/20 = 42$

Noise can still be generated by the multiplexing itself however; by the switching of the multiplexor and cross talk between channels.

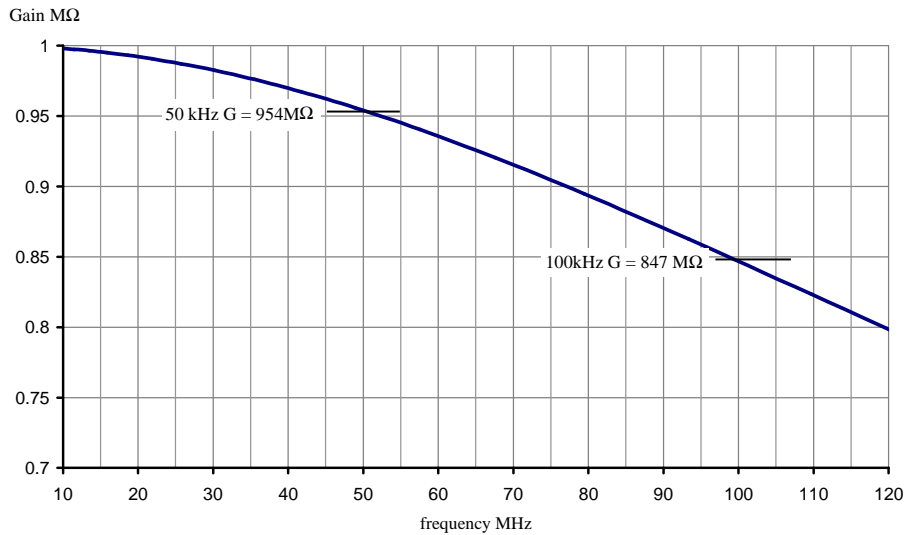


Figure 6.5 Gain of photodiode transimpedance pre amplifier, with the gains for 50 kHz and 100 kHz shown. The filter is useful in reducing the noise input to the multiplexer.

6.2.5 DC (r) section

For low anisotropy samples the DC level does not change significantly with time so that a slow but accurate 16 bit DAC (PCI-6033E) is used for this purpose. The 16 bit accuracy allows for a large signal range, which can be set by software. Because of this, potentiometers are not required to individually set the range, as required for the AC section.

6.2.6 AC (Δr) section

The Δr AC section consists of a set of potentiometers so that each channel can have a different amplification. This is important in order for each channel to have the optimum range for the ADC. The signal level of both r and Δr paths can vary over the spectrum, especially at short wavelengths where the lamp output, detector sensitivity and optics all contribute to a weaker signal. For the Δr path the fast ADC output is only 8 bits wide, so limiting its dynamic range. Signals can easily saturate the ADC if they are too high or get comparable to digitisation noise if too low. After

the potentiometers the signals are amplified by AC coupled amplifiers and fed into the analogue multiplexer. The AC coupled amplifiers are built around the Analog Devices AD847 operational surface mount amplifier. They are configured as voltage amplifiers with a gain of 1000. The multiplexer (CD74HCT4067) is driven by the control unit which, in sync with the PEM, selects the input to be passed to the ADC. The multiplexer is addressed from the counter in the timing unit (see figure 6.5). The PC interface handles the control lines to clock the data into a digital I/O card in the PC. Because each channel has a different amplification a calibration scheme is used and is described below.

6.2.7 PC interface

The PC interface provides buffering and handshaking protocols between the ADC and the PC digital I/O. Data is clocked *into* the PC synchronously, but no data is clocked until the first sample of the first channel. This enables the PC to correctly bin the data into the correct channel location. The PC thus initiates the transfer of data but the instrument clocks the data *in* after the start of the next PEM cycle.

6.2.8 Timing unit (AC path)

The timing unit synchronises the multiplex addressing, ADC conversion timing and interface clocking with the PEM frequency of 50 kHz. The multiplexer address is driven by a synchronous counter that is part of the frequency multiplier phase locked to the PEM frequency (see figure 6.6). Because 16 channels need to be sampled 16 times over a PEM period, the PEM frequency needs to be multiplied by a factor of 256. The frequency multiplication is achieved using a Texas instruments CD74HCT7046A phase lock loop as shown in figure 6.5. A photograph of the PCB layout of the timing unit is shown in figure 6.7.

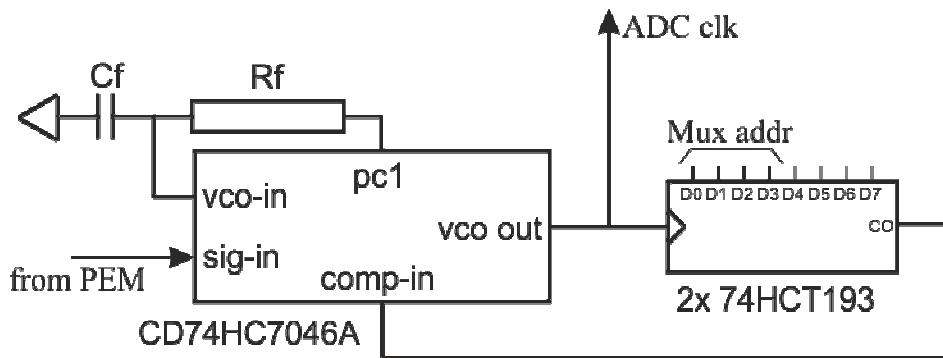


Figure 6.6 System diagram of showing main components of Timing Unit for ADC clock and multiplex synchronisation circuit.

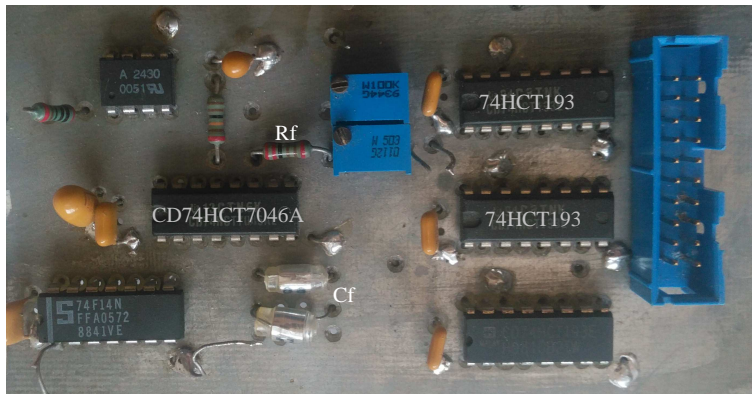


Figure 6.7 PCB layout of the timing unit

6.2.9 Multiplexer

The CD74HCT4067 CMOS analogue multiplexer [53] allows 16 AC inputs to share the same ADC by switching quickly between each input (see figure 6.2). This is done sequentially by driving the multiplexer address from the frequency multiplier counter, shown in figure 6.5. The ADC clock timing is arranged so that the multiplexer is stable when the ADC conversion takes place. Using a multiplexer, as opposed to a multi ADC approach, has both advantages and disadvantages. Amongst the advantages are: reduced cost and component count and a common ADC that makes channels more uniform. Amongst the disadvantages are switching noise, less integration time for ADC, which leads to lower conversion accuracy and as a consequence less dynamic range. Another consequence is that each channel is not sampled exactly at the same time and thus a phase shift across the spectrum occurs that needs to be taken into account.

6.2.10 AC calibration procedure

Because the gain of each AC channel is adjustable, using the potentiometers, as explained above, it is necessary to calibrate each channel to reconstruct an accurate spectrum. A calibration test LED is provided to do this, see figure 6.2. The LED was modulated in synch with the PEM and had a wide beam angle to fairly uniformly illuminate the detector, as could be checked by monitoring the DC, so that the different gains in the AC channels could be determined and corrected for in the software. A flat AC response across the spectrum was thus obtained.

6.2.11 PEM retardation

In common with the multi-channel lock-in design by Kaspari *et al* [49] the Liverpool Fast RAS cannot provide a uniform angular retardation across the spectrum, due to the wavelength dependence of the PEM. As shown in chapter 2 section 2.4 the output of the RAS instrument is dependent on the Bessel functions, J_1 and J_2 , relating respectively to the ωt and $2\omega t$ components of the detector output. J_1 and J_2 are a function of the maximum retardation, R , over a PEM cycle for the wavelength in question. In a standard Aspnes PEM RAS instrument the PEM controller can set each wavelength to the same retardation so that J_1 and J_2 are constant across the spectrum. J_1 and J_2 can be computed from the equation 3.59.

The PEM controller can set the retardation at any particular wavelength to achieve either a maximum for J_1 or J_2 , for all the other wavelengths the respective J value will be lower, and will need to be calculated. It is desirable to set the weakest part of the spectrum, usually the smallest wavelength, to the maximum value for J_1 or J_2 , or a combination of both, depending on the experimental requirements.

6.2.12 Determination of retardation over spectral range

For a PEM set for a retardation angle R_0 (radians), at a wavelength, λ_0 (metres), the estimated retardation R at other wavelengths needs to be determined. If we consider the retardation as a time difference, Δt between the propagated light of the ‘fast’ and ‘slow’ axes of the PEM, then after the PEM,

$$\Delta t = \frac{d}{c} \Delta n \quad (6.3)$$

where d is the thickness of the PEM element, c is the speed of light and Δn is the difference in refractive index between the ‘fast’ and ‘slow’ axes of the PEM. The retardation, R , expressed in radians is thus:

$$R = 2\pi \frac{c}{\lambda} \Delta t \quad (6.4)$$

using equation 6.3 equation 6.4 becomes:

$$R = 2\pi \frac{d}{\lambda} \Delta n . \quad (6.5)$$

The difference in refractive index, due to the birefringence of the PEM, is not independent of wavelength [54]. The stress-optical coefficient, C , relates the refractive index to the applied stress, σ , on the PEM element, thus:

$$\Delta n = C \sigma \quad (6.6)$$

hence equation 6.5 becomes

$$R = 2\pi \frac{d}{\lambda} C \sigma \quad (6.7)$$

d and σ are considered constant with respect to wavelength thus

$$R = k \frac{C}{\lambda} \quad (6.8)$$

where k is constant of proportionality

Thus if the retardation is fixed at wavelength λ_0 to R_0 radians, with a stress-optical coefficient of C_0 , the value the retardation, R , at another wavelength λ is thus

$$R(\lambda) = \frac{C(\lambda)\lambda_0}{C_0\lambda} R_0 \quad (6.9)$$

The stress-optical coefficient values $C(\lambda)$ for fused silica (the material of the PEM element) were obtained by the least squares interpolation of data referenced by N K Sinha [54]. Figure 6.8 shows how the retardation varies with wavelength, with and without using the stress-optical coefficients. Figure 6.8 shows how the Bessel functions J_1 and J_2 change with wavelength.

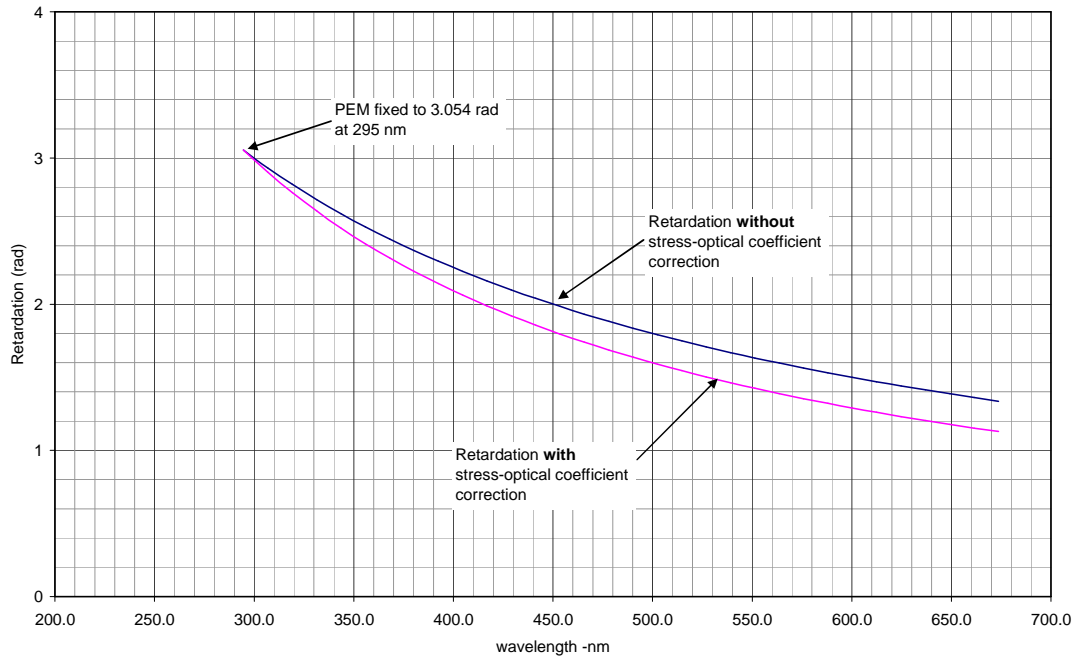


Figure 6.8. More accurate determination of retardation over the spectrum with a fixed PEM setting.

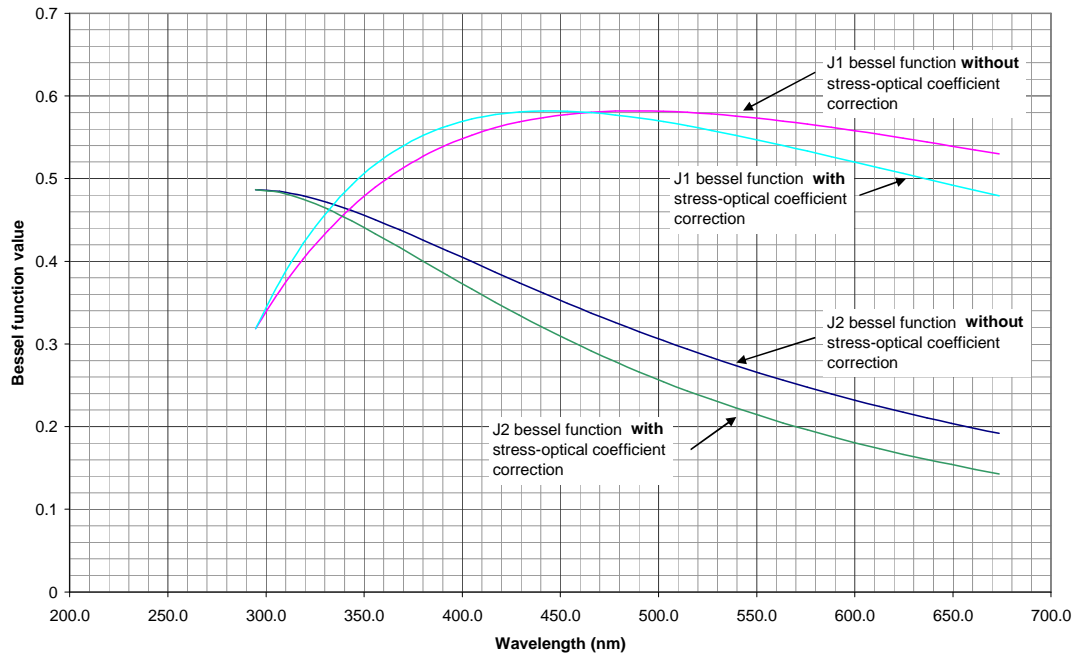


Figure 6.9. Resulting J_1 and J_2 Bessel functions derived from the retardance as shown in figure 6.7.

Since implementing the stress-optical coefficients into determining the retardation, for a parallel capture of the RAS spectrum, it was found that C. G. Hu *et al* have published a paper covering this issue [55].

6.2.13 Wavelength Calibration

This is done using a series of optical filters over the spectrum, with the peak detected on the DC. A least squares fit is carried out to give an accurate wavelength value corresponding to each photodiode element.

6.2.14 Electronic test and calibration

The DC card, with the aid of the calibration LED, is used to calibrate the AC signal. The calibration LED is supplied with a DC current on which is superimposed a known AC modulation. A red LED is chosen as this is a region that the photo-diode array is sensitive to, although other colours could also be used. With the photo-diode screened against ambient light the LED is shone onto it. The computer measures the light distribution across the photo-diode array with the DC ADC. A calibration factor is applied to each AC channel so that the AC channels have the same distribution shape as the DC channels. By varying the AC and DC currents into the

calibration LED the channels can be checked for non-linearities, a correction can be made in software to correct this.

6.3 Experimental use of the FRASv1 16 channel fast RAS instrument

The 16 channel fast RAS described in this chapter was used to monitor the electrolytic deposition/growth and removal of copper on a Au(110) surface, as described by Harrison *et al* [52]. The growth stage was done over a period of 500 s whereas the removal only takes about 15 seconds. Hence the removal stage is the more onerous test of the instrument. The data was averaged over a period of 50 ms and with a PEM frequency of 50 kHz (period 20 μ s) this means a total of 2500 PEM cycles were averaged for each data point for each channel. Figure 6.10 shows the interpolated spectra obtained for 16 channels during the rapid electrochemical removal of copper on the surface. For clarity only spectra taken at intervals of 0.9 s are shown. Figure 6.11 shows the removal of copper as a function of time for the spectral energies; 1.58, 1.88, 2.07 and 2.76 eV. This indicates the noise level obtained at the spectral interval of 50 ms.

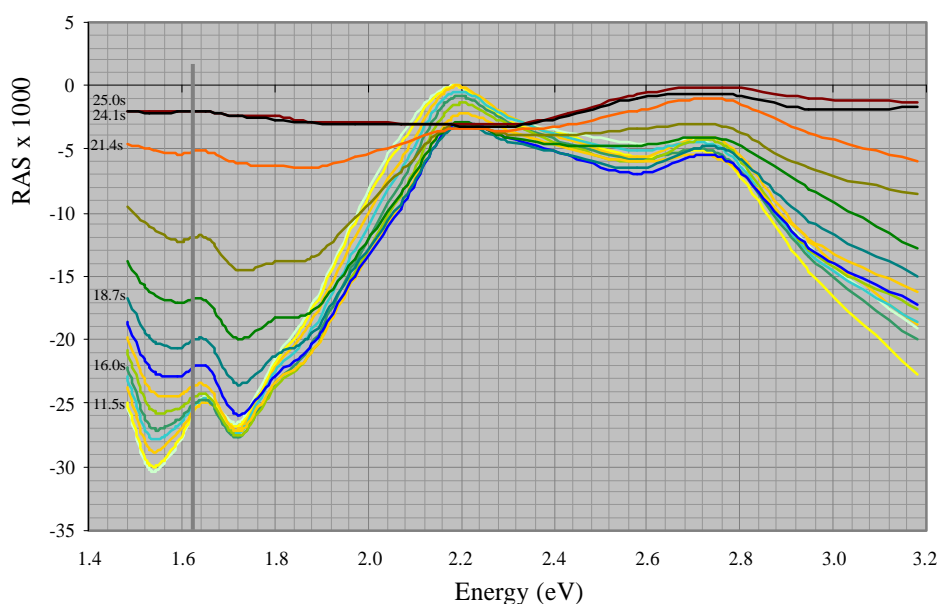


Figure 6.10 Reflection anisotropy spectra for the third rapid removal of Cu from Au(110). Spectra were averaged over 0.05 s, only data at intervals of 0.9 s are shown. Plot is interpolated over 16 channels.

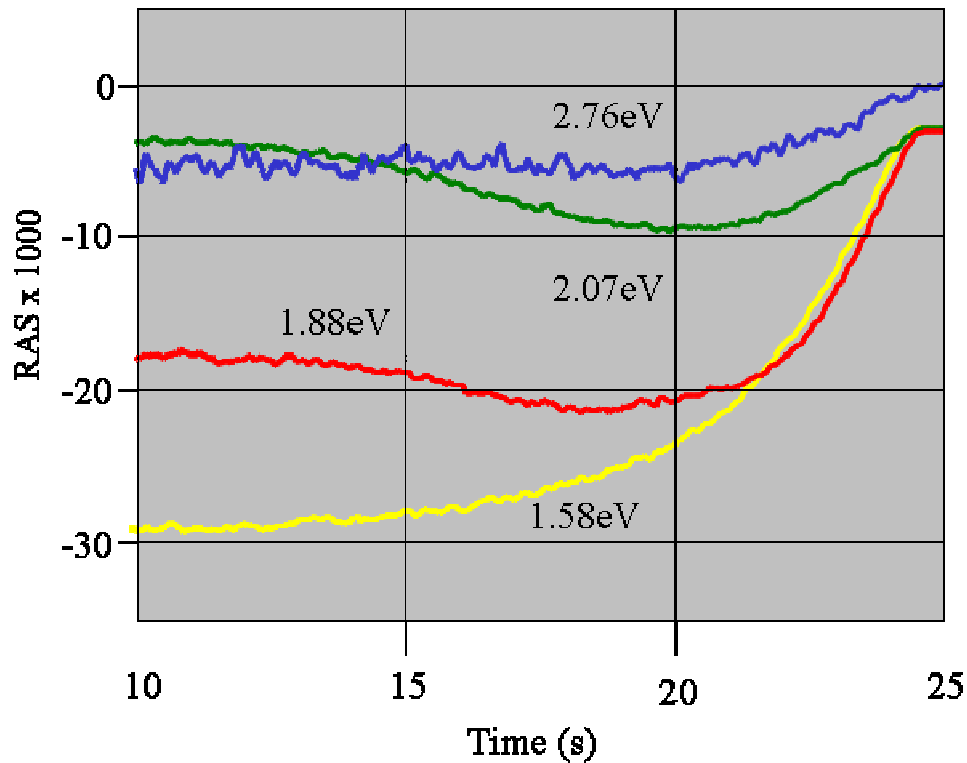


Figure 6.11 Time dependence of the RA signal during the rapid electrolytic removal of Cu from Au(110).

6.4 FRASv2 32 channel enhanced UV upgrade

The 16 channel FRASv1 instrument was limited to a spectral range below approximately 3.2 eV, this was due to the photodiode detector array (IPL10220NW16) lacking sensitivity beyond this point. It was also decided to increase the spectral resolution by upgrading to 32 channels. In order to accomplish this a new detector array was used. To readout 32 channels the 16 channel readout design was converted, see section 6.4.2 below.

6.4.1 Enhanced photodiode array

To extend to range of the instrument beyond 3.2 eV and provide 32 channels a Hamamatsu S4114-35Q 35 [56] element photodiode was used. This array has a quartz window for better UV response and has 35 channels. Figure 6.12 shows the response of the detector taken from the Hamamatsu S4114-35Q 35 data sheet.

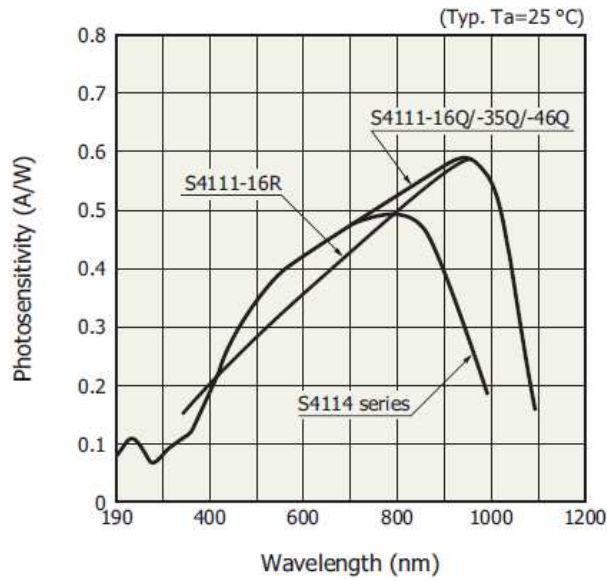


Figure 6.12 Spectral response of Hamamatsu S4114-35Q photodiode, as taken from data sheet [56].

6.4.2 Read-out electronics

To scan 32 channels of the photodiode array could be done by designing a 32 channel multiplexed read-out into a single flash ADC. The ADC used in the 16 channel device would be fast enough to handle 32 channels each sampled 16 times over a PEM cycle; resulting in a 26.6 MHz sampling rate or 78 ns period. The CD74HCT4067 multiplexer can be configured to allow two multiplexers to be operated as a single 32 channel multiplexer but it cannot operate at the 26.6 MHz speed required for a 32 channel operation. In order to avoid the need for further development it was decided to ‘double-up’ the 16 bit version and use two separate multiplexers and two ADCs, one multiplexer/ADC would thus handle the even numbered photodiode channels and the other multiplexor/ADC would handle the even numbered. The system diagram in figure 6.13 illustrates how this was done. Differences in the characteristics of the two channels can be calibrated out if needed, using the AC calibration procedure.

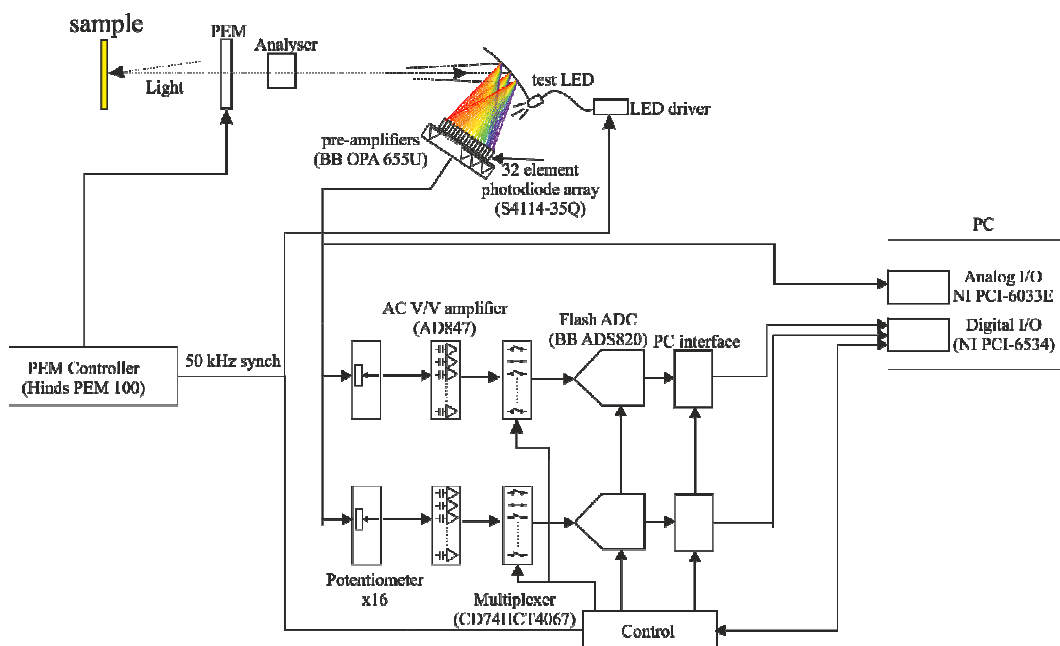


Figure 6.13 System diagram of 32 channel FRASv2 instrument. This is based on a doubling up of the 16 bit design which uses two separate multiplexers and two ADCs.

6.5 Experimental use of the Liverpool FRASv2 32 instrument

The ability of RAS to probe solid/liquid interfaces allows redox chemistry and dynamic properties to be studied. The 32 channel FRASv2 instrument was used to monitor these dynamics in which cytochrome P450 protein was deposited onto a Au(110) surface within an electrochemical cell [16]. Establishing the conditions under which a monolayer of cytochrome P450 reductase forms on the Au(110)/electrolyte interface is an important first step in the study of the dynamic behaviour of this protein using RAS.

Figure 6.14 shows the changes in RAS as a function of time at (a) 2.02 eV, (b) 2.25 eV, (c) 2.53 eV, (d) 2.66 eV, (e) 2.73 eV, and (f) 3.06 eV measured in the fast RAS instrument during the adsorption of P499C full-length CPR onto the Au(110) at -0.652 V in $0.1\text{M NaH}_2\text{PO}_4\text{-K}_2\text{HPO}_4$ (pH 7.2).

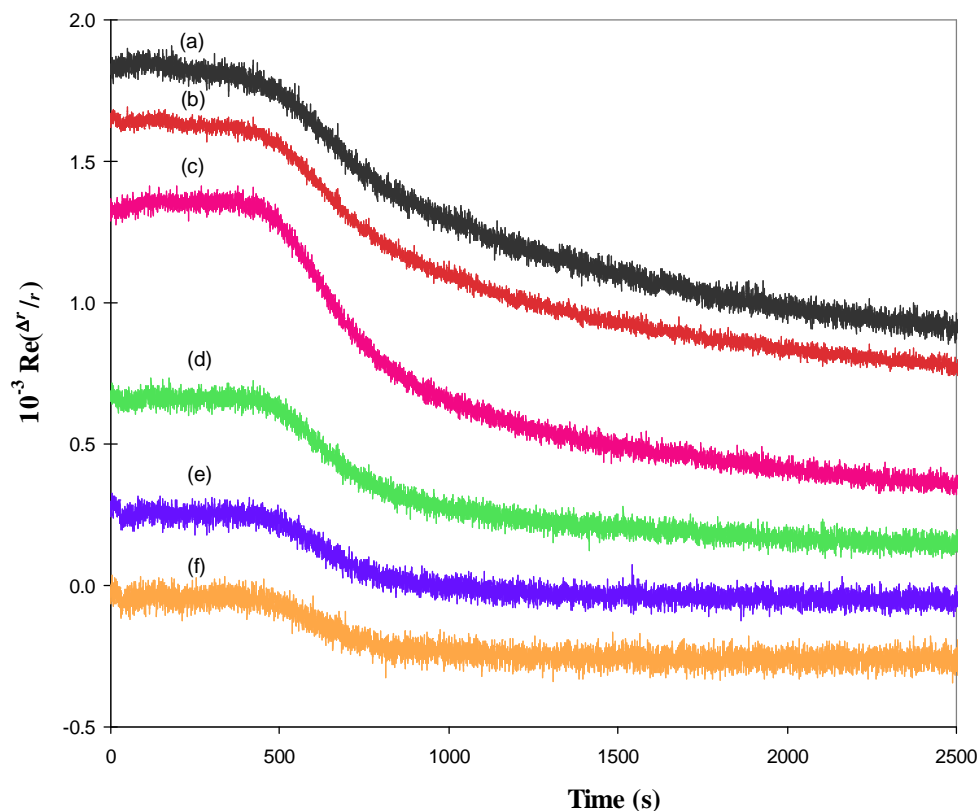


Figure 6.14 RAS as a function of time at (a) 2.02 eV, (b) 2.25 eV, (c) 2.53 eV, (d) 2.66 eV, (e) 2.73 eV, and (f) 3.06 eV measured in the fast RAS instrument during the adsorption of P499C full-length CPR onto the Au(110) at -0.652 V in 0.1M $\text{NaH}_2\text{PO}_4\text{-K}_2\text{HPO}_4$ (pH 7.2). All the graphs correspond to the same intensity scale but are separated by arbitrary amounts on the vertical axis to prevent overlap.

6.6 Summary

This chapter has described a novel RAS instrument design, in both 16 channel (FRASv1) and 32 channel (FRASv2) variants, that is capable of recording spectra much faster than a standard RAS instrument. The speed increase comes from the fact that channels are read in parallel, and there is no dead time while advancing a monochromator.

There are areas for improvement however; in dynamic range, timing and data processing. With the existing instrument it is possible for the AC signal to exceed the range of the ADC or to fail to have the resolution required due to digitisation noise on low level signals. The timing unit worked well but requires careful setup to ensure that the timing is stable. In some cases a lapse of synchronisation could result

the data being allocated to the wrong channel. As regards the data processing the current design does not have the data acquisition necessary to record and store data at the same time, which impacts on the ability to signal average over the whole time available. These are the the main aspects that are addressed in the FRASv3 design.

Chapter 7: Improved 32 channel fast RAS version 3 (FRASv3)

7.1 Review of FRASv1 and FRASv2 instruments	132
7.2 Dynamic range	132
7.3 Synchronisation stability	134
7.3.1 Synchronisation using linear interpolation	136
7.3.2 Synchronisation using binning	137
7.4 Data acquisition	138
7.4.1 Input set-up	139
7.4.2 Sample clock configuration	140
7.4.3 Time stamping each sample clock pulse	141
7.5 Data processing	143
7.6 Noise reduction by averaging	143
7.7 Noise reduction by fitting exponentials	144
7.7.1 Equation of total fit to step change	149
7.8 Experimental application of the FRASv3 instrument	149
7.8.1 Au(110) response to potential switch from 0.3 V to 0.6 V	150
7.8.2 Au(110) response to potential switch from 0.3 V to -0.6 V	152
7.8.3 Summary of experimental application	153

7.1 Review of FRASv1 and FRASv2 instruments

The multiplexed 16 channel (FRASv1) and 32 channel (FRASv2) Fast RAS instruments described in the previous chapter suffered from three main drawbacks in the following areas:

- **Dynamic range.** The 8 bit analogue to digital conversion restricts the dynamic range. The potentiometers used to improve dynamic range necessitated adjustment and calibration which was time consuming, see section 6.2.6.
- **Synchronisation stability.** Any instability in the signal sampling, caused by limitations of the timing unit (figure 6.6) will result in noise in the acquired data. A lapse of synchronisation can also result the data being allocated to the wrong channel.
- **Data acquisition.** The inability of the data acquisition in the FRASv1 and FRASv2 to directly stream data to the hard drive results in dead time when the program switches from acquiring data to processing it and/or storing it.

The development challenge of FRASv3 is to address these areas.

7.2 Dynamic range

In an effort to improve the accuracy and dynamic range of the multiplexed FRASv1 and FRASv2 designs, an option could be to increase the number of bits on the ADC, but this could lead to longer conversion times. Longer conversion times would restrict the degree of multiplexing that could be done and may make it infeasible as the multiplexing itself adds to the component count. To offset against these difficulties more high specification components and a more complex design would be required, which again adds to the cost of the design and build. A full multiplexed system where all 32 channels were sampled 16 times over the PEM cycle of 20 μ s, would result in a conversion rate of 25.6 MHz and thus a data rate of 51.2 Mbyte/sec. Although this is within the scope of state-of-the-art multiplexers and 16 bit ADCs, the high bandwidth necessary through the multiplexer and ADC would not make it easy to achieve the low noise levels that would be demanded to maintain

16 bit accuracy or dynamic range. Hence it was felt that for 16 bit accuracy a non multiplexed design would be simpler and give better results than a multiplexed one.

The data acquisition for the FRASv3 instrument was based on a National Instruments PXIe-1073 chassis used with two PXIe-6368 multifunction boards each with 16 separate 16 bit ADCs and a single PXIe-6363 board which has 32 inputs multiplexed to a single 16 bit ADC. Details on the chassis and boards can be found on the National instruments website [57]. Figure 7.1 shows how this was incorporated with the front end electronics of the FRASv2 design shown in chapter 6.

In common with other RAS instruments designed for use with low anisotropic samples, the ‘DC’ is regarded (as the name suggests) as being constant relative to the ‘AC’ signal (*i.e.* the ‘DC’ is not a function of ω see equation 3.60), and thus can be measured on a timescale longer than the PEM cycle period. For this reason the ‘DC’ is read using the slower, and cheaper, multiplexed PXIe-6363 board. Whilst the ‘AC’ signal is digitised using the PXIe-6368 board. (Should an application arise where the ‘DC’ channel needed to be read accurately then this could be done using the same PXIe-6368 boards as the AC for the ‘DC’. This would add considerably to the cost of the instrument.)

The peak output level of the ‘DC’ across the spectrum is typically around 1 volt, thus with the full scale input set to a 0 to 2 volt range, the ‘DC’ can be measured by the 16 bit PXIe6363 to a resolution of 30 μ V, without signal averaging. With the 1 M Ω gain of the photodiode pre-amplifiers this corresponds to a resolution in the photodiode of 30 pA. The Burr Brown OPA655U operational amplifier that forms the basis of the photodiode pre-amplifier (see section 6.2.3) has an input offset error of +/- 125 pA.

Each of the 32 ‘AC’ channels is amplified by a factor of 1000, by the ac coupled amplifiers, based on the AD847 operational amplifiers, before being input to the two PXIe-6368 boards. Each PXIe-6368 has 16 individual 16 bit ADCs, so two are required to deal with the full 32 channels from the photodiode. Typically the

maximum RMS value of the signal across the spectrum is less than a volt, the full scale input range would typically be set to the -5 V to +5 V range. Thus the resolution per least significant bit of the PXIe-6368 would be approximately 153 μ V. As this is after the AC amplification this corresponds to a photodiode current of less than 0.2 pA. The photodiode array, Hamamatsu S4114-35Q [56] is quoted as having a dark current of 600 pA so this suggests the digitisation noise would be much less than thermal noise from the photodiode.

The input impedance of both the PXIe-6363 and the PXIe-6368 are >10 G Ω in parallel with 100 pF thus the loading on the photodiode pre amp is negligible.

To connect the ‘AC’ amplifiers to the PXIe electronics six NI SCB-68A connector blocks were used, four on the two PXIe-6363s and two on the single PXIe-6368. These connector blocks allow easy and adaptable connections from the pre-amps and the ‘AC’ amplifiers to the PXIe-1073 assembly.

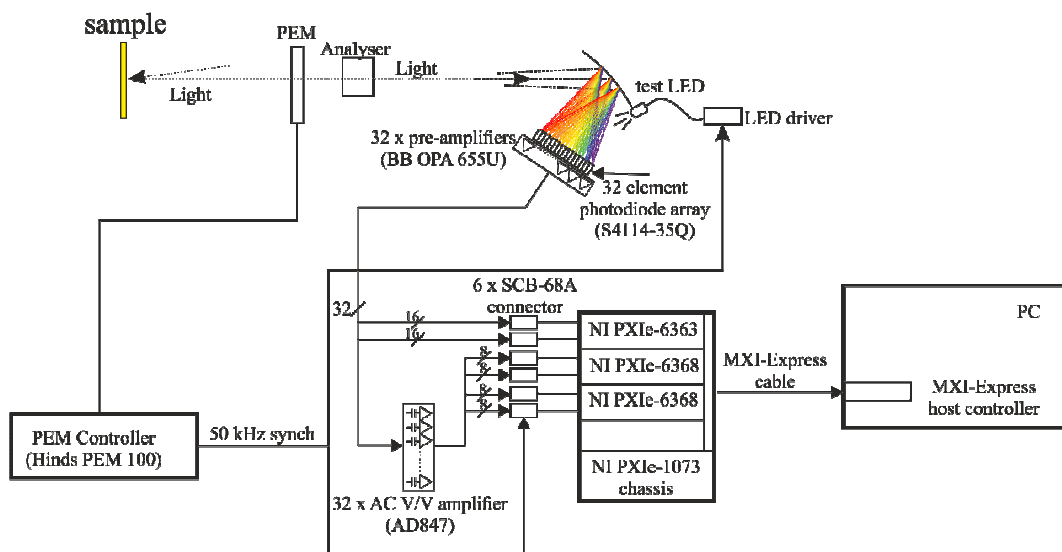


Figure 7.1 System diagram of FRASv3 the photodiode array, pre-amplifiers and AC amplifiers from the FRASv2 32 are used.

7.3 Synchronisation stability

Figure 7.2 shows a typical RAS waveform (without noise) from a photodiode pre-amplifier. In the FRASv1 and FRASv2 designs the signal is sampled 16 times over, and in sync with, the PEM reference signal. Thus the signal is sampled at even

intervals Δt , and at constant phase to the PEM. This is useful as it allows easy signal averaging by summing corresponding sample points over a number of cycles. It has the disadvantage that timing jitter may result due to the phase locked loop constantly adjusting to maintain its output oscillator in lock with the PEM reference (see section 6.2.8). A lapse in phase lock may also cause the data to be assigned to the wrong channels.

Figure 7.3 shows the sampling points for the FRASv3 instrument. In this design, rather than using a fixed sampling clock that is synchronised with the PEM, an unsynchronised sample clock is used where the sample time is measured relative to the PEM reference signal.

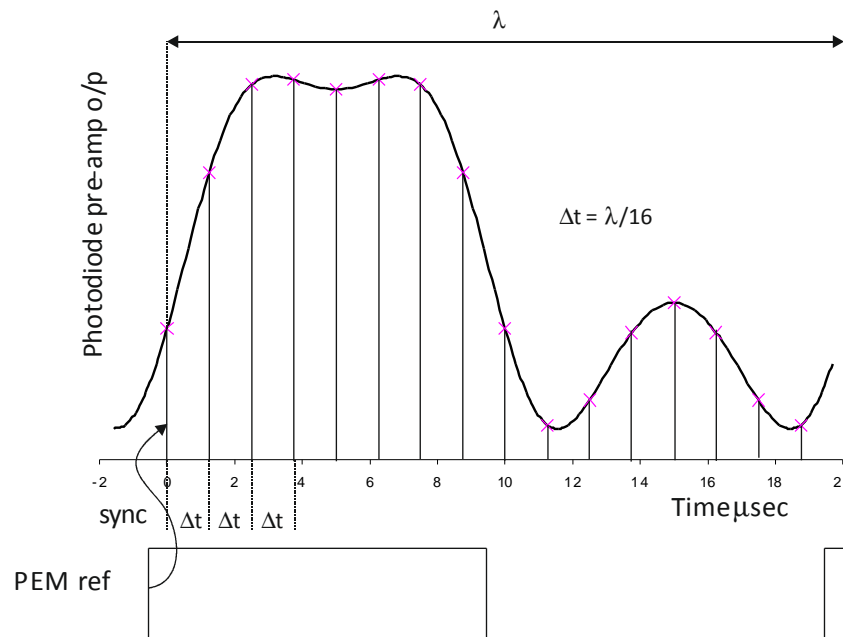


Figure 7.2 Synchronous sampling as used in the FRASv1 and FRASv2 designs.

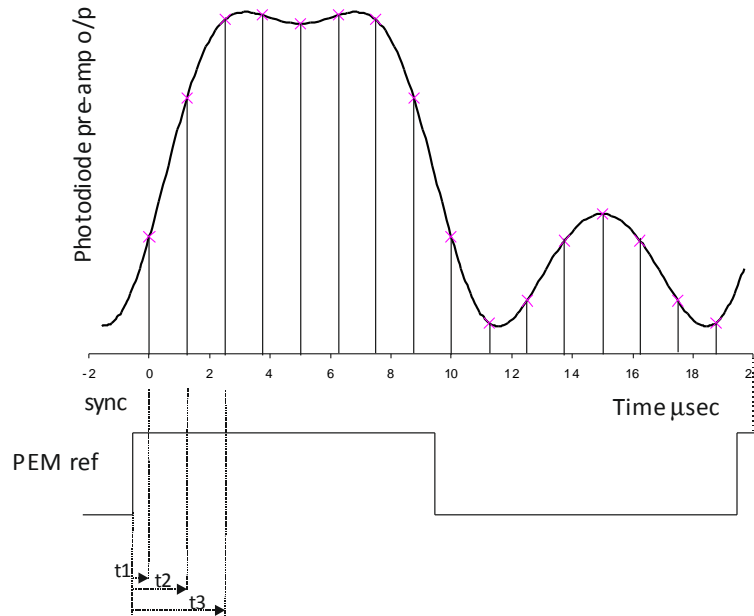


Figure 7.3 Asynchronous sampling as used in the FRASv3 design. Each sample strobe is time stamped from the rising edge of the PEM reference.

The NI PXIe-6368 and PXIe-6363 multifunction boards have timing control circuits that are accurate to 10 ns (based on an internal 100 MHz clock), allowing the possibility of time stamping every signal sample relative to the PEM reference, see figure 7.3. This means that the sampling clock and the PEM reference are no longer synchronised by the hardware, however pseudo synchronisation can be achieved in software. Two different methods were used an ‘interpolation’ method and a ‘binning’ method, both are described below.

7.3.1 Synchronisation using linear interpolation

Simple linear interpolation can be used to generate pseudo synchronised sampling and this can be carried out in real time or by post processing the saved data later. Post processing the data also allows the possibility of more accurate interpolation without the constraints of real time demands. Figure 7.4 illustrates the linear interpolation.

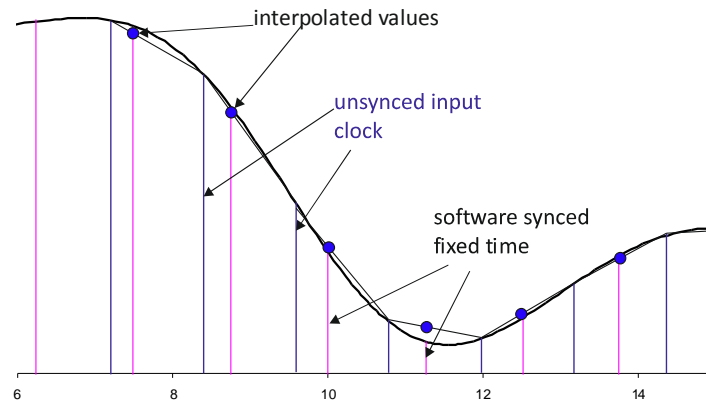


Figure 7.4 Interpolating to obtain signal values at synchronised fixed time values (pink lines) from the unsynchronised input clock (blue lines). Black trace represents the real signal. The blue dots are the interpolated values.

7.3.2 Synchronisation using binning

If the signal is to be averaged over a number of PEM cycles then the sampling can be overlaid and an average taken of the signal that occurs within phase boundaries that correspond to ‘bins’ across the PEM cycle, this is illustrated in figure 7.5.

The binning method of software synchronisation is suited to cases where a significant degree of signal averaging is needed; this means a large number of data samples will be spread over the whole of each bin. For example assuming a 50 kHz PEM (20 μ s period), and a requirement for 10 ms time resolution, then 500 samples (10 ms/20 μ s) could be averaged within each bin. This results in a fairly accurate but very fast method of software synchronisation and is particularly suited to real time processing.

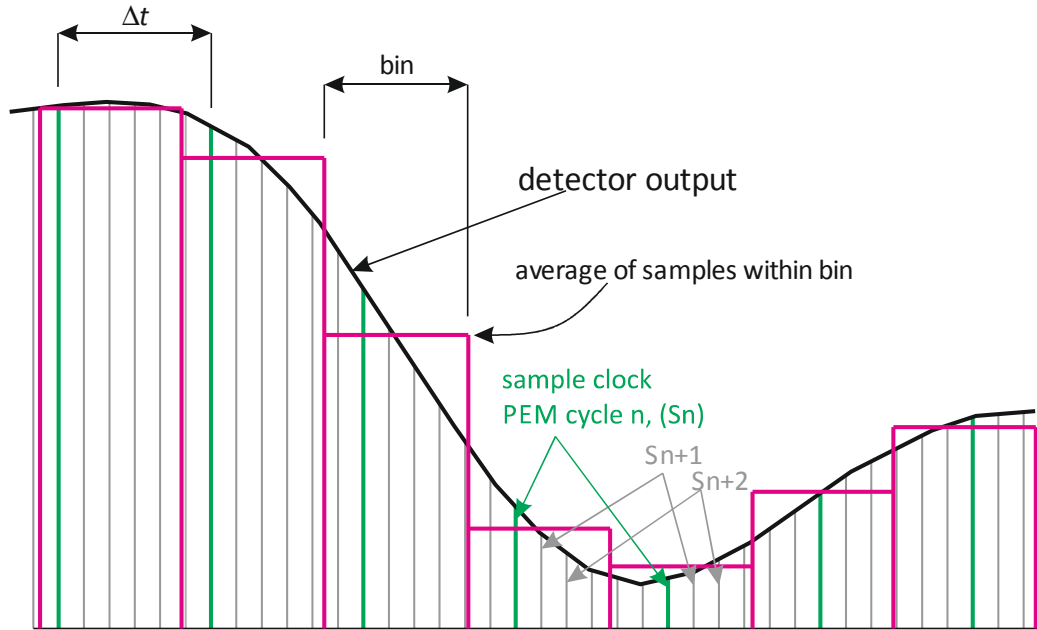


Figure 7.5 Illustration of software sample synchronisation using binning. Note how the sample interval Δt is slightly longer than the bin interval so that over multiple PEM cycles an even spread of samples is taken.

7.4 Data acquisition

National Instruments Labview software [42] was used for the data acquisition, control, processing and storage of the data for the FRASv3 instrument. In Labview parlance a programme subroutine is called a VI (virtual instrument), the DAQmx VIs, in combination with compatible data acquisition cards, provide a set of hardware drivers that allow un-interrupted high speed data streaming onto a hard drive. The two PXIe-6363 cards used for the ‘AC’ waveform capture could run at over 1 MHz resulting in a data transfer rate of 64 Mbyte/sec for the 32 16 bit ADCs. This combination of hardware and software eliminates dead time and provides maximum signal-to-noise to be achieved.

The full Labview code used in the FRASv3 instrument is large and would require extensive documentation to explain fully so here just the main parts that are particularly relevant to the operation of this instrument are explained. The user interface and other programming details have been omitted, as they are fairly routine to general Labview code.

7.4.1 Input set-up

Figure 7.6 shows the setup part of the Labview program to initialise the AC and DC channels. Above the 'create virtual channel' label are the DAQmx create channels VIs that set the type and range of the inputs. The top two VIs setup the AC channels inputs on the PXIe-6368 board, the lower VI setup the DC channels inputs. The AC channels are set to 'Differential' mode, which configures the inputs as shown in figure 7.7(a). Differential inputs provide good noise immunity as common mode noise is rejected at the balanced inputs of the on-board amplifiers. The 'DC' channels are set to 'Non-Referenced Single-Ended' (NRSE) mode, which configures the inputs as shown in figure 7.7(b), this is necessary as there is not enough pin-outs to allow 'Differential' mode for 32 channel operation.

Both AC and DC channels are set to voltage mode, with the ranges set using variables which can be changed from software. The physical channels to which the VIs are assigned are addresses using identifier codes. As an example; `PXI1Slot3/ai0:PXI1Slot3/ai15` is the id code for an analogue input range sourced from PXI chassis no. 1, slot 3, analogue input channel, 0 to 15 (this happens to be the PXIe 6368 card in slot 3).

The VIs over the 'set input clock' label in figure 7.6 set the sampling rate, number of samples and the clock source. Both the AC channels have the same clock source (from slot 4) whereas the DC channels are driven from a clock source on slot 2 that is synchronized to 1/40 of the AC clock rate.

The VIs above the 'start task' label, enable the data acquisition to start, subject to the input clock. (Until the clock is activated no data is clocked in.) The Slot 4 PXIe-6368 is enabled last (using the sequence structure) and its error channel is used to pass on program flow to the clock generation VIs. This way all data acquisition channels are ready before the input clock is started.

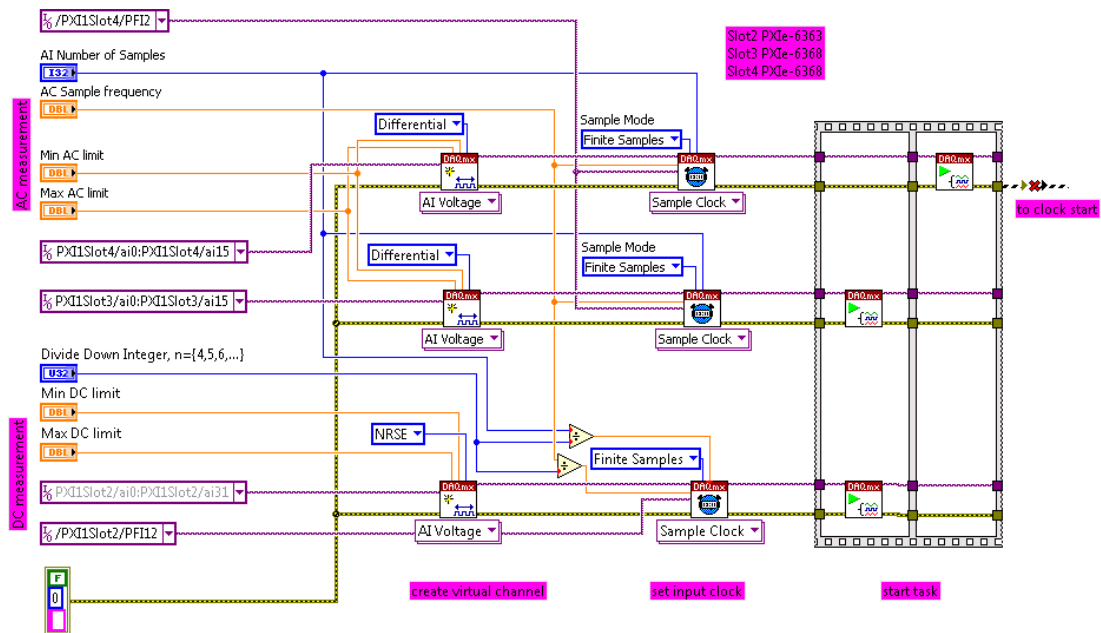


Figure 7.6 The different input configurations selected by the software for the analogue voltage inputs. Only two channels are shown of the 32 for the PXIe6363 or the 16 for the PXIe-6368.

7.4.2 Sample clock configuration

In the FRASv3 design, as mentioned above, a non-synchronised sampling clock is used. This is made possible by the counter timer features available on all three of the PXI boards used. Here is shown how the counter timers are configured to generate the pulses at the right frequency and to record the time delay (or phase) between the rising edge of the PEM reference signal and each sampling clock pulse. Figure 7.8 shows the Labview code used to setup the sample clock. Above the ‘configure counter’ label slot4 counter 0 (PXI1Slot4/ctr0) is assigned by the ‘CO Pulse Freq’ VI as the counter to do this, the DAQmx channel VI sets pin PFI2 from slot 4 as the output pin for the clock, the variable ‘frequency’ above the set parameters label sets the clock frequency. Depending on the application the experiment can be set to record a finite number of clock pulses or free run until stopped by the user. This is done on the timing VI, above the ‘set number of pulses’ label. When the ‘start pulses VI’ is reached, the data is streamed directly into memory or hard drive.

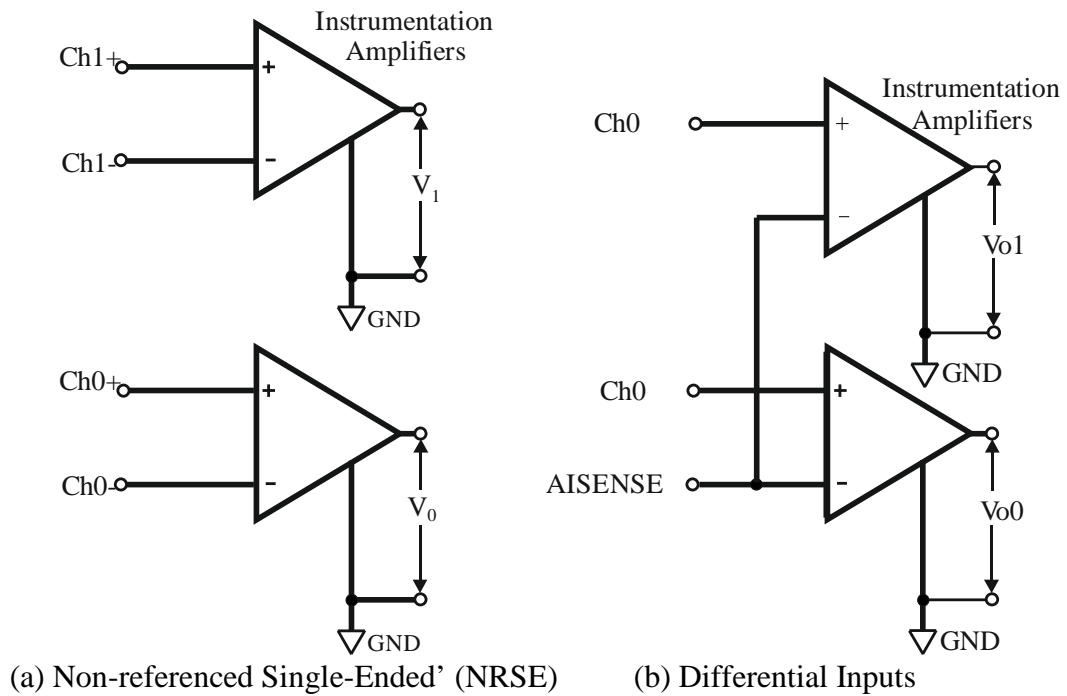


Figure 7.7 Labview software to set up DACmx VI data channels. The top two rows of VIs setup the AC channels with the bottom row setting up the DC channels.

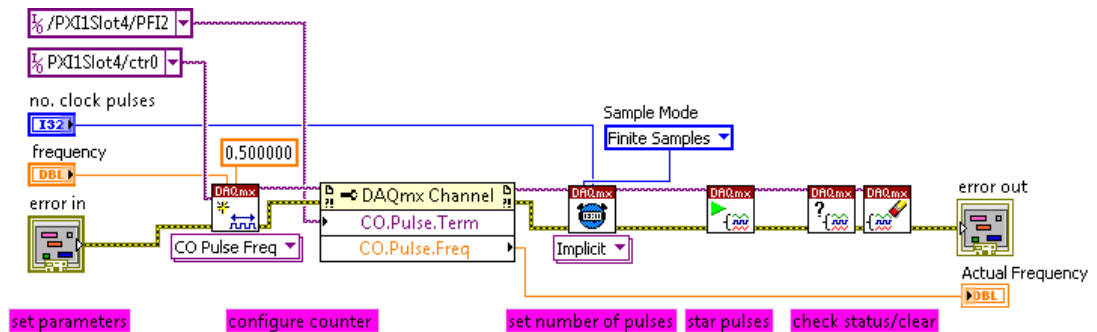


Figure 7.8 Sampling clock configuration. Counter PXI1Slot4/ctr0 is used to set the sample clock frequency. Connector pin PXI1Slot4/PFI2 is used as the counter output.

7.4.3 Time stamping each sample clock pulse

To record the time at each sample clock (relative to rising edge of the PEM reference) counter, PXI1Slot4/ctr1, is used. This is driven by the 100 MHz on-board timebase, thereby giving the counter a 10 ns resolution. The counter is reset by the rising edge of the PEM, via a user defined input pin, PFI7. The counter output is

sampled by the sample clock (PFI2), which also clocks the AC data. In this way every sample clock has a time stamp from the last PEM rising edge.

The setup code is shown in figure 7.9 which has comments added with a pink background. Above the ‘input variables and constants’ comment are all the inputs to this section of code. Above the ‘select hardware counter’ comment, is the VI that selects counter 1 in slot 4 and configures it to count rising edges. Above ‘configure DAQmx Channel’ is the ‘DAQmx Channel’ VI, this adds further configuration options to the counter channel, such as counting from the 100 MHz timebase and resetting on the PEM rising edge (PFI7 on slot 4). The next VI in the chain assigns a file in which to stream (or log in Labview parlance) the counter data into. The ‘Sample Clock’ VI uses PFI2, the sample clock to log the counter 1 value into the DAQmx channel and onto disk. A nominal AC frequency is set, which in is used in this mode so the VI can set buffer sizes.

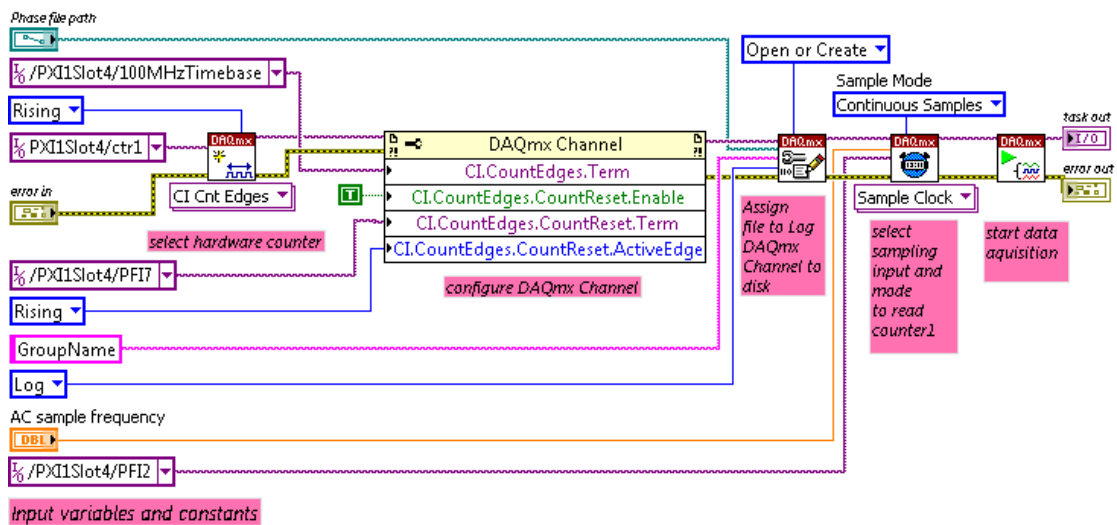


Figure 7.9 Pulses from the 100 MHz timebase are counted and the count at each sampling clock is registered and streamed via DAQmx Channel onto disk. The counter is reset on each rising edge of PEM reference so that the saved file contains the timing of each sample from the last rising edge of the PEM reference.

When the VI above ‘start data acquisition’ comment is executed the DAQmx channel is primed and will clock counter 1 data when the sample clock is run. As the sample clock also clocks the AC channels and, via a divide counter, the DC

channels, all the data is synchronised. The 'task out' can be used to run other tasks associated with this DAQmx channel such as the monitoring and display of data.

7.5 Data processing

Data processing may be done in real time and/or later after the raw data is stored. The availability of cheap high capacity hard drives usually means the latter is done even if some processing is done in real time. If the instrument is to be used for real time monitoring then real time processing has to be done. After the data is captured it is interpolated as described above, in order for easy signal averaging. After averaging the fundamental and second harmonic frequency components are determined. This may be done in real time or offline, depending on the application and/or the available computing resources available.

Depending on the application, the amount of time the instrument is run and the available storage space, the software may take different forms. If an experiment is run for a limited time, there is adequate data storage space and the results are not required in real time, then streaming all data to disk is the best option as this allows maximum flexibility in analysing the data without losing information. In this case only low CPU power, but large storage space maybe required, depending on how long the experiment is run. If storage space is not available for the length of time the instrument is run, then online signal averaging could be used at the cost of temporal resolution. If the results are required in real time then faster processing may be required, this would require a combination of higher specification computer hardware and less accurate but faster algorithms.

7.6 Noise reduction by averaging

The high performance of the PXIe system with the Labview DAQmx allows for continuous streaming of data. This means there is maximum opportunity to use averaging to reduce the noise level. The first consideration in the noise reduction is to establish the temporal resolution that is required in the analysis. For example if 1 ms resolution is required with a 50 kHz PEM (20 μ s period) then this would restrict averaging to under 50 PEM cycles. This averaging may wholly or partly be done with the software synchronisation if 'binning' is used, otherwise it can be done later

by signal averaging simply by overlaying and averaging multiple waveforms, as shown in figure 7.10.

If too much signal averaging is done then the temporal resolution suffers, an example of this is shown figure 7.11, here the blue trace shows a typical output from a FRASv3 instrument channel. The sample, a Au(110) crystal, was part of an electrochemical cell that was subject to a voltage step. The sudden change in the surface atoms causes an optical change that is picked up on the FRASv3 instrument. Signal averaging 500 PEM cycles, gives the output a temporal resolution of 10 ms. This is shown in the blue trace in figure 7.11. This shows the output still has a high level of noise. By using further signal averaging of 200 points, this reduces the 10 ms resolution to 2 seconds, this is shown in the green trace in figure 7.11. The noise is dramatically reduced (by square root of 200) but at a cost of temporal resolution that may be unacceptable.

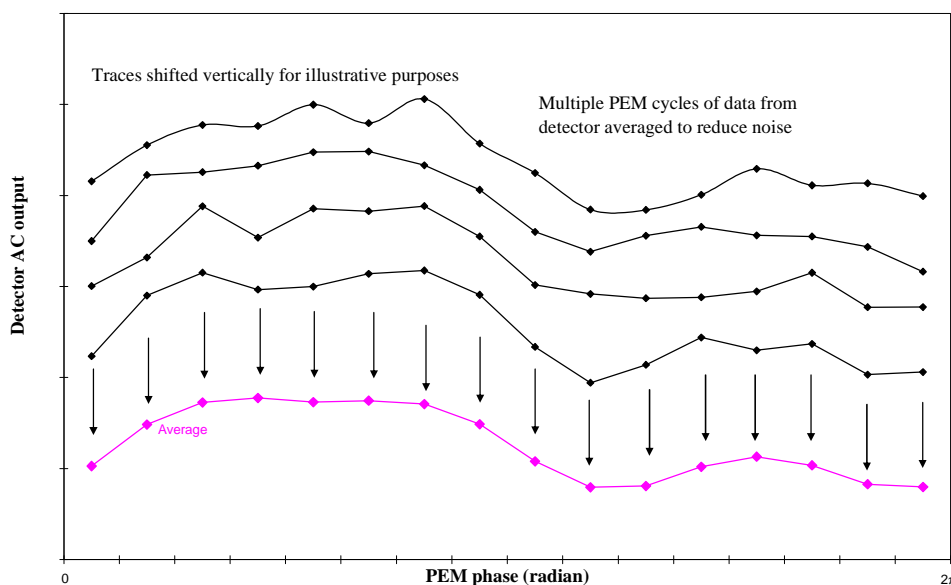


Figure 7.10 This is to illustrate how, after software synchronisation, the data taken over multiple cycles can be averaged to reduce the noise.

7.7 Noise reduction by fitting exponentials

To provide better signal-to-noise without loss in temporal resolution, when, for example the sample is subject to a sudden change, as in the case of a voltage step applied in an electrochemical cell, a method of fitting a series of exponential

transients is explored. This method is not applicable to all cases, but in many cases the RAS signal can be approximated with a series of exponential transients.

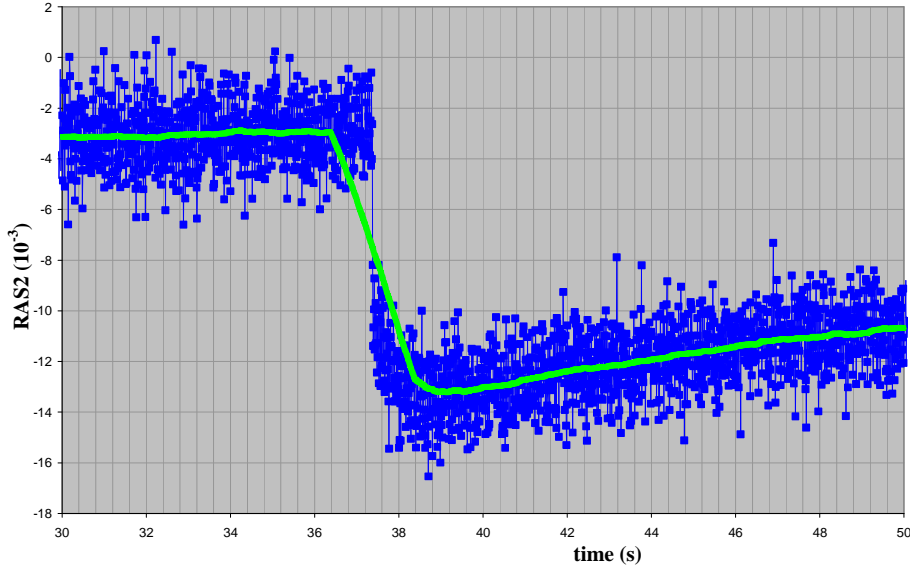


Figure 7.11 A typical output from a single RAS channel (blue), shows how high averaging (green) reduces noise but at the cost of temporal resolution.

The period before the sample is subject to change, the RAS output is assumed to be quiescent, apart from being subject to random noise. At this stage any amount of signal averaging does not have an adverse effect. Once a change is initiated, say by applying a step voltage to the sample in an electrochemical cell, then this can be precisely marked, either electronically through the data acquisition system, or by monitoring the output of all channels and using the channels with the highest sensitivity to the change to time stamp the step point for all channels. The fit uses the method of least squares to fit an equation of the form:

$$f(x) = Ae^{bx} \quad (7.1)$$

where $f(x)$ is the fit to the experimental data $F(x)$. A and b are constants that are found by an iterative process in which they are varied until equation 7.2 is a minimum, *i.e.*:

$$\sum_{i=0}^n [f(x_i) - F(x_i)]^2 = \text{minimum} \quad (7.2)$$

Figure 7.12 shows the RAS signal used in figure 7.11 with the quiescent, or pedestal value shown in yellow. This is done by simple averaging over a suitable number of samples prior to the step. The pedestal value for each channel is stored and subtracted from the RAS data before the first exponential is calculated.

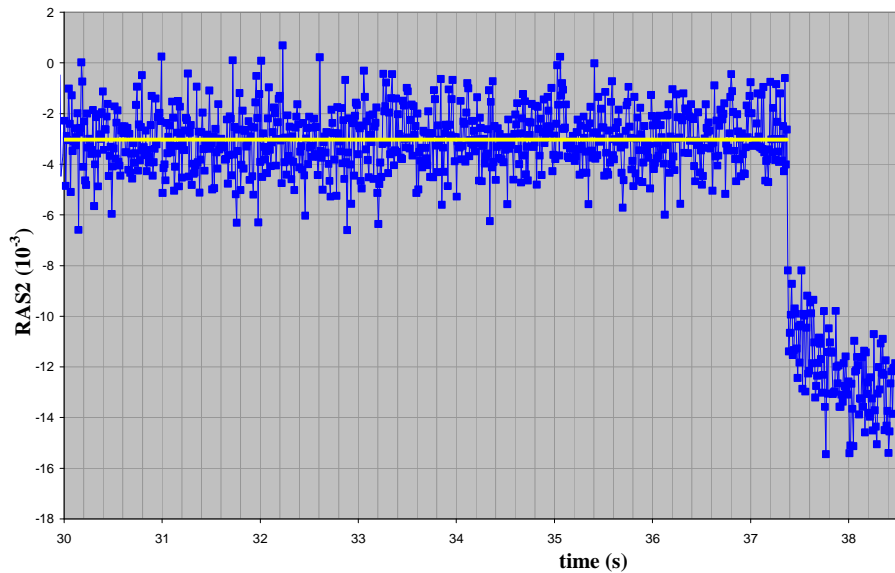


Figure 7.12 The quiescent or pedestal value (yellow) is calculated by averaging a number of sample values (blue) before the step point.

Figure 7.13 Shows the RAS output data (blue) near the step point after the pedestal has been removed. The first exponential fit is applied to the RAS data, where the last data point before the step is treated as $t = \text{zero}$ for the fit. The purpose of this first fit is to capture the very fast initial transient of the step.

The next stage in the process is to subtract the first exponential, the results of which are shown in figure 7.13. The remaining data is now ready for the second exponential fit, shown in yellow on figure 7.14.

This process is continued until, ideally, the remaining data averages out at zero. In this example 3 exponentials are fitted. Figure 7.15 shows the third exponential fit.

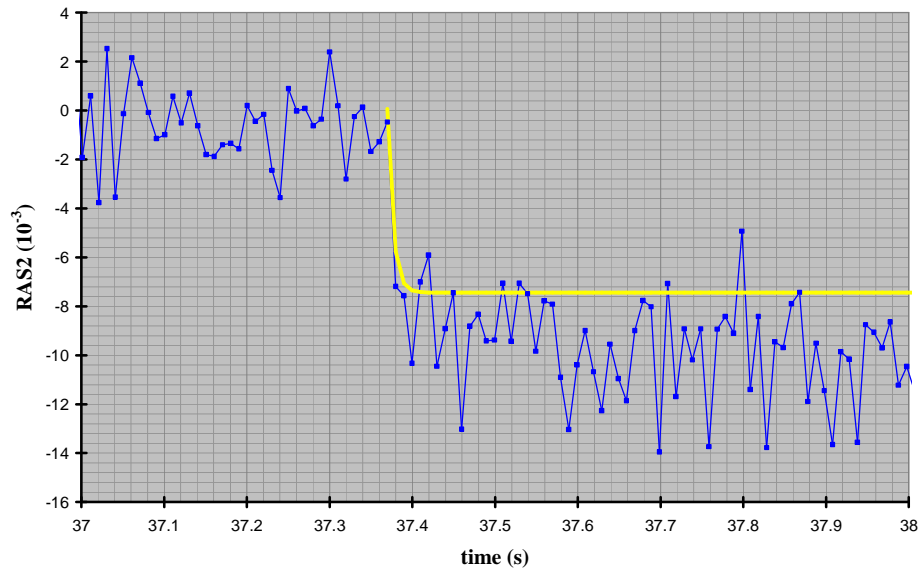


Figure 7.13 After subtracting the pedestal value from the RAS data (blue) the first exponential (yellow) is fitted to capture the initial fast transient of the step.

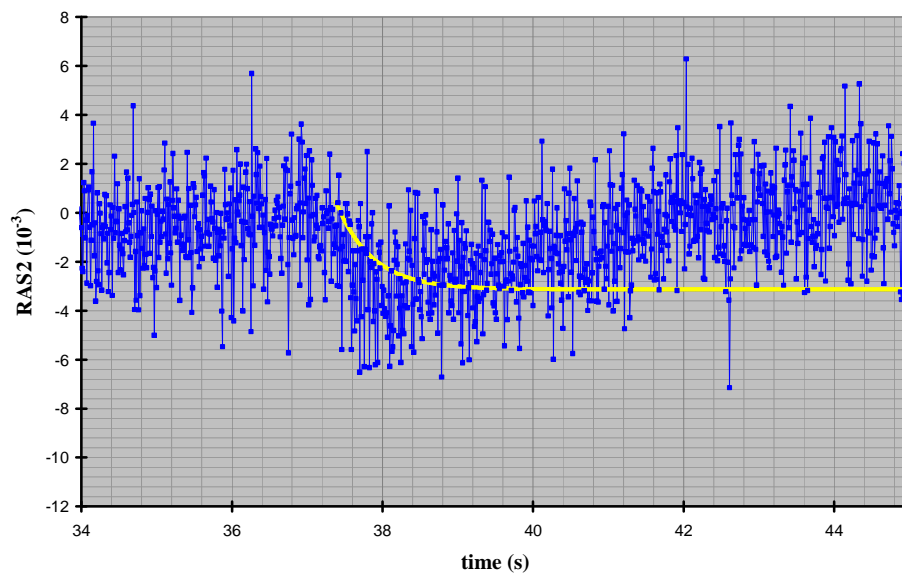


Figure 7.14 Having subtracted the first transient the second exponential is fitted. Note the longer time constant.

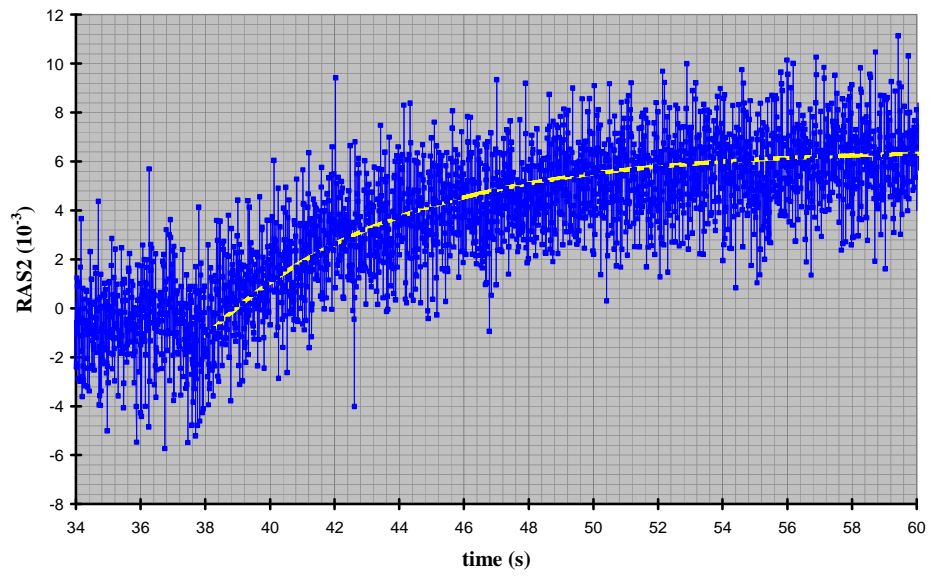


Figure 7.15 The final third exponent is fitted (yellow).

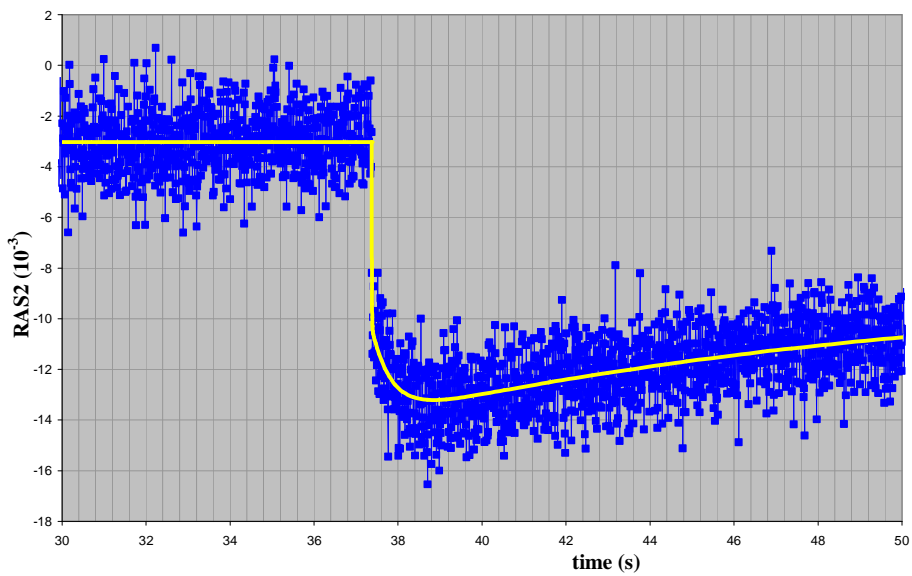


Figure 7.16 The final fit (yellow) overlaid on original RAS data (blue).

7.7.1 Equation of total fit to step change

The final fit to the original data is shown in Figure 7.16. This fit is described by the following equations:

$$\text{For } -\infty < t < t_s \quad f_{RAS} = ped \quad (7.3)$$

$$\text{For } t \geq t_s \quad f_{RAS} = \sum_n (A_n \exp((t - t_s)/T_n) + C_n) + ped \quad (7.4)$$

where; n is the index of the exponential fit, A_n is the amplitude of exponent n , T_n is time constant of exponent n , C_n is level shift of constant n , t_s is the time at start of step, ped = value of f_{RAS} before t_s .

Thus for each step the RAS response can be reduced to a few fit parameters and the FRAS channel energy. For the example fit above, taken at an energy of 2.95 eV, the fit parameters are:

$$A_0 = 7.505 \times 10^{-3}$$

$$T_0 = -0.00667 \text{ s}$$

$$A_1 = 3.579 \times 10^{-3}$$

$$T_1 = -2.095 \text{ s}$$

$$A_2 = -0.1894 \times 10^{-3}$$

$$T_2 = -13.655 \text{ s}$$

$$C = -5.6125 \times 10^{-3}$$

$$ped = -3.02665 \times 10^{-3}$$

$$t_s = 37.37 \text{ s}$$

7.8 Experimental application of the FRASv3 instrument

The FRASv3 instrument was used on an experiment by Harrison *et al* [58] in which rapid changes in the RAS profile were observed for Au(110) in an electrochemical cell under H₂SO₄ electrolyte as the applied potential was switched between 0.3 V and 0.6 V. This is a potential range in which the Au(110) surface is not reconstructed and is below the potential range of surface oxidation. The reversible spectral changes

occurred in less than 10 ms and were, attributed to the replacement of adsorbed anions by an oxygenated species.

As part of the same experiment, but not yet published, the potential was changed to -0.6 V, after the second 0.3 V. Unlike the 0.3 V to 0.6 V transition, switching to -0.6 V does cause the surface to reconstruct and is known to create a surface on the Au(110) that has (1×3) arrangement [47]. As this change involves a reorganisation of the surface atoms it is not as fast or reversible as the 0.3 to 0.6 V change.

7.8.1 Au(110) response to potential switch from 0.3 V to 0.6 V

The kinetic change at 3.05 eV (stated as 3.1 eV in paper) in the RAS spectrum, when the electrochemical potential was changed from 0.3 V to 0.6 V, is illustrated in figure 7.17. The graph shows the data, integrated over 10 ms steps displayed in blue, along with a single exponent exponential. Figure 7.18 shows a similar graph to 7.17 but at 3.38 eV. The respective time constants for 3.05 and 3.38 eV are 6.8 ms and 7.3 ms. With a step interval of only 10 ms these time constants cannot be considered accurate, but they do underline the fact that the transitions are fast and stable, and can be fitted to one exponential function.

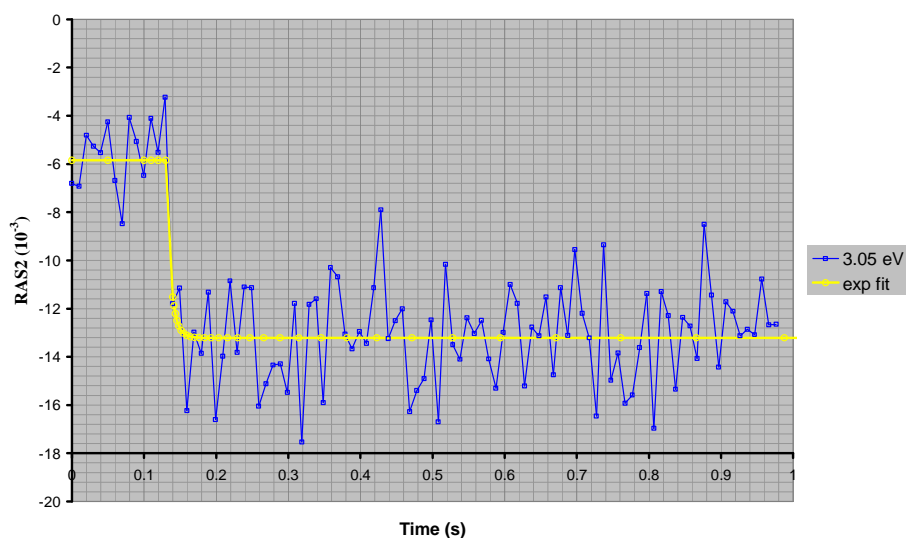


Figure 7.17 Change in RAS2 at 3.1 eV when applied potential was change from 0.3 V to 0.6 V. Blue trace is the data from FRASv3 instrument, the yellow trace is the single exponent exponential fit which has a time constant of 6.8 ms.

The resulting spectra for the 3 potentials 0.3 V, 0.6 V and 0.3 V are shown in figure 7.19 and also included is the response from the standard monochromator RAS instrument for the 0.6 V potential. The latter shows both instruments have a good agreement up to about 4 eV, after which both instruments suffer from low signal levels in which offsets and nonlinearities can introduce errors.

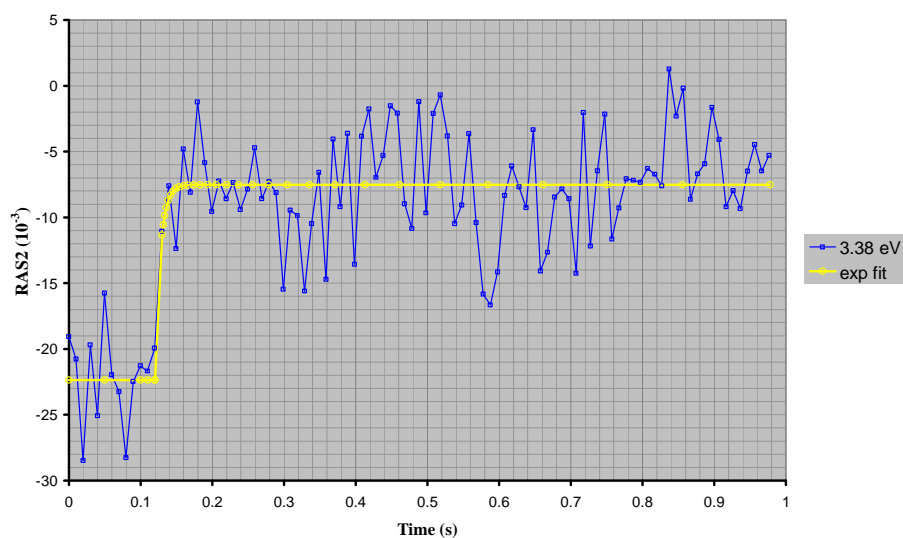


Figure 7.18 Change in RAS2 at 3.38 eV when applied potential was change from 0.3 V to 0.6 V. Blue trace is the data from FRASv3 instrument, yellow trace is the single exponential fit which has a time constant of 7.3 ms.

The blue trace in figure 7.19 shows the RAS spectrum at a potential of 0.3 V; when 0.6 V is applied there is a very quick jump to the spectrum shown in green; then when the voltage is returned to 0.3 V there is an equally fast transition to the pink trace. The initial and final 0.3 V spectra are seen to be almost identical, as RAS is a very sensitive probe of the surface it indicates that the surface returns to the same state. The speed of this reversibility indicates that the surface Au(110) atoms have not undergone any reconstruction as this would take more time and/or would not be reversible. It is concluded in the paper by Harrison *et al* [58] that OH anions are attracted to the surface when the potential is increased to 0.6 V and are repelled again when the potential returns to 0.3 V.

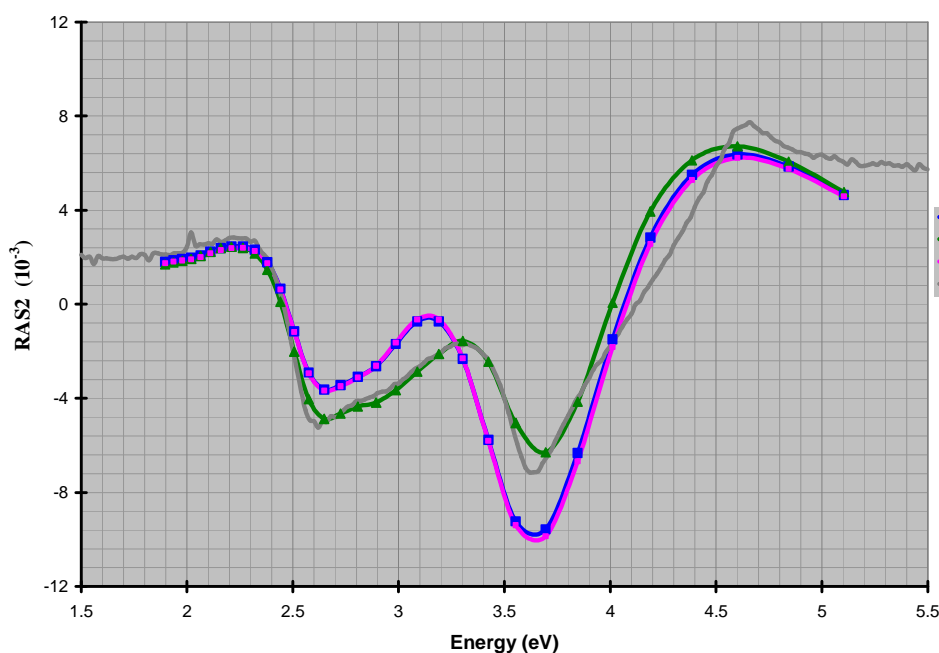


Figure 7.19 RAS2 spectra of Au(110) in an electrochemical cell with electrolyte H_2SO_4 . The blue trace shows the initial potential of 0.3 V, the potential is switched to 0.6 V, shown by the green trace. The pink trace shows the spectrum after the potential is switched back to 0.3 V. The grey trace is the initial spectrum recorded on a standard (slow) RAS instrument.

7.8.2 Au(110) response to potential switch from 0.3 V to -0.6 V

As part of the same experiment conducted by Harrison *et al* but not yet published the potential was changed to -0.6 V, after the second 0.3 V. This is known to create a surface on the Au(110) that has (1×3) arrangement [47].

Using the same principles explained above, a family of spectra was produced to follow the progression of the RAS spectra. This is shown in Figure 7.20 in which the spectra are displayed on a logarithmic time base. A further advantage of fitting the RAS data to mathematical functions is that the spectra can be displayed at any time value, not necessarily at the ones recorded.

Figure 7.20 shows the RAS2 spectral transition from Au(110)-(1×1) to Au(110)-(1×3). The black line shows the spectrum before the -0.6 V was applied, the red line shows the spectrum of the fast step (at $t = 10$ ms), whilst the green lines show how

the spectra evolve as the surface changes. The insert graphs show the \log_{10} time response at three selected energies.

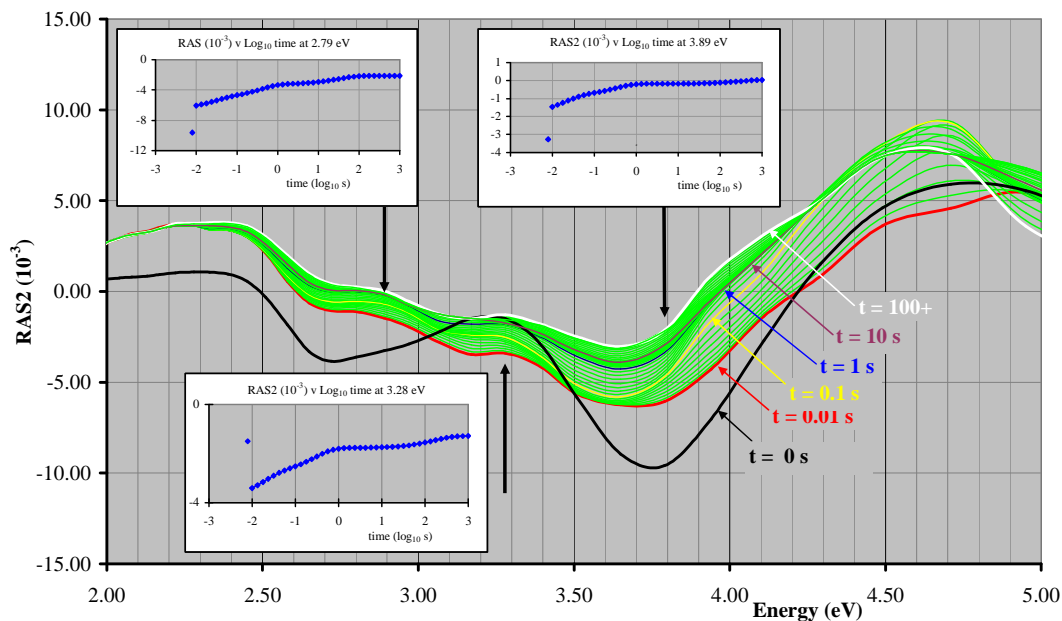


Figure 7.20 Family of *RAS2* spectra plotted on a logarithmic time base indicating dynamics of surface changes in Au(110) as the electrochemical potentials change from 0.3 V to -0.6 V, invoking the surface arrangement to change from a (1×1) to a (1×2) structure. Inserts show temporal response at the indicated energies.

7.8.3 Summary of experimental application

Using the FRASv3 instrument Harrison *et al* [58] were able to show that changes in the *RAS2* profile of the Au(110)/H₂SO₄ interface, as the potential is switched between 0.3 V and 0.6 V, are reversible and on a timescale of less than 10 ms. This excludes the possibility that the processes observed are due to surface roughening, rather that they are due to fast process associated with OH adsorption. The fact that changes are observed on a timescale of less than 10 ms establish the FRAS instrument as a powerful tool for monitoring the dynamics of processes occurring at electrochemical interfaces.

The study of the Au(110)-(1×1) to Au(110)-(1×3) shows that the FRASv3 instrument is capable of displaying the spectra of a dynamic surface over orders of magnitude of time response, in this case ms to 100 s of seconds. Further analysis of

this data may help to understand the progression of this reorganisation. Being able to obtain full spectral response with high temporal resolution may enable known RAS signatures to be used to infer the surface reorganisation that is happening over short, as well as extended, time periods.

Chapter 8: Conclusion and further developments

8.1 RAS theory, instrumentation and analysis	156
8.2 Chapter 4 Simulation of PEM-based RAS instrument	157
8.3 Displaying ADRAS data	157
8.4 Development of a Fast RAS instrument	158
8.5 Improved 32 channel fast RAS version 3 (FRASv3)	158
8.6 Combined rotation and Fast ADRAS	159
8.7 Future work - CD instrument	159
8.7.1 Calibration	160

8.1 RAS theory, instrumentation and analysis

In chapter 3 the theoretical RAS values and the calculated output of the PEM-based RAS instrument, were expressed in terms of the sample parameters a , b , c , d and the sample orientation, θ . This enabled the output of the RAS instrument to be directly compared to the theoretical RAS values. This showed that with the sample at, the standard $\theta = \pi/4$ orientation, the $RAS1$ and $RAS2$ outputs of the PEM-based RAS instrument agree with $\text{Re}(\Delta r/r)$ and $\text{Im}(\Delta r/r)$ provided $a \cong c$ and $b \cong d$. However the real value of this analysis is that it provides a model which can predict the output of the RAS instrument in situations where the sample has a high anisotropy and where the sample orientation is not at the standard $\theta = \pi/4$ rad. This will allow the correct interpretation of the experimental data in these circumstances.

In the analysis of the definition of RAS it was shown that the real part, $\text{Re}(\Delta r/r)$, was found to be approximately equal, as expected, to the difference of the reflectance in x and y directions divided by the sum of the reflectance in x and y (see equation 3.29). Perhaps not so obvious is the finding that the imaginary part of the RAS definition, $\text{Im}(\Delta r/r)$, was approximately equal to the phase difference between the Fresnel reflection coefficients, φ_{Δ} , see equation 3.32, figure 3.2 and figure 4.6. By using $\text{Re}(\Delta r/r)$ and $\text{Im}(\Delta r/r)$ it may be possible to determine the anisotropy in the complex dielectric constant of the surface using equation 3.81.

The discovery of a 4θ term in the $ADRAS2$ rotation waveform has prompted some interest, for example Farrell *et al* [44] and Lane *et al* [59]. From the description of the $ADRAS2$ output as shown in equation 3.80 we can see that the coefficient of the $-\sin(4\theta)$ term is $|\Delta r|^2/|r|^2$, as we get the $\text{Im}(\Delta r/r)$ and $\text{Re}(\Delta r/r)$ from the standard RAS instrument, then $|\Delta r|^2/|r|^2$ does not provide any more information. So the major benefit in the ADRAS technique is the ability to establish the orientation of the anisotropy and not to identify 4θ components in the rotation waveform.

The detector output of the Aspnes PEM-based RAS instrument is described by equation 3.60, where it is expressed in terms of the sample parameters (a , b , c , d), the rotation angle θ and the Bessel functions (J_0 , J_1 , J_2 ... J_n), which are derived from the

PEM maximum retardation (A). It is worth noting that equation 3.60 is not an approximation but the exact detector output of an ideal Aspnes PEM-based RAS instrument under sample rotation. But it is interesting to note that even an ideal RAS instrument does not give exact values for $\text{Re}(\Delta r/r)$ and $\text{Im}(\Delta r/r)$ when the anisotropy is large. This can be seen by comparing figures 4.8 and 4.9 which shows $RAS2$ and $\text{Re}(\Delta r/r)$ respectively and also figures 4.10 and 4.11 which show $RAS1$ and $\text{Im}(\Delta r/r)$ respectively. Following these calculations it should be possible to calibrate the RAS instrument to give exact $\text{Re}(\Delta r/r)$ and $\text{Im}(\Delta r/r)$ values even under high anisotropy.

8.2 Chapter 4 Simulation of PEM-based RAS instrument

In chapter 4 the RAS simulation was used to verify that the analysis in chapter 3 was done correctly and to explore how the outputs of the RAS instrument behaved under different sample reflections. It was found that the simulation agreed exactly with the analysis, indicating that both were done correctly.

The simulation is capable of much more than to verify the analysis. The azimuthal angle of all the components can be varied. All four complex Jones matrix elements of each optical stage can be varied, including non-diagonalisable matrices. Noise can be added and dynamics studied. A further extension to the simulation could be to include un-polarised light, this would enable imperfect optics to be modelled and thus indicate the most appropriate components to use in terms of cost versus accuracy. To deal with un-polarised light the Jones matrix formalisation could be replaced using Stokes vectors and Mueller calculus [2].

8.3 Displaying ADRAS data

Chapter 5 explored ways of presenting ADRAS data that could reveal sample features that may otherwise not be noticed. This took previously published work by Farrell *et al* [44] and Weightman *et al* [45], and displayed them on an Argand-type diagram so that loci of the spectra could be displayed on a 2D plane. This work illustrated the point that anisotropy changes orientation as the spectrum wavelength is changed. This could be used to highlight dipoles acting away from the normal anisotropy direction.

By adding an offset angle to the rotation angle, the most appropriate orientation can be found to portray the data as orthogonal spectra. By doing this, the spectrum that is orthogonal to the dominant spectrum reveals details about dipole components acting away from the dominant anisotropy direction. The *ADRAS2* for the Ag(110) shown in figure 5.11 is a good illustration of this. The initial focus of interest was the 4θ component in the rotational waveform which could only be seen where the 2θ *ADRAS* was near zero. However as figure 5.11 shows there is information hidden from the standard RAS that is brought out by using orthogonal spectra.

Unfortunately *ADRAS1* data was not available for this study. The processing of both *ADRAS1* and *ADRAS2* data in future work would provide an interesting insight particularly if plotted as described in chapter 5.

8.4 Development of a Fast RAS instrument

Chapter 6 introduces the first and second versions of the Fast RAS. The design of these first two FRAS instruments was based on using a multi-channel detector and a multiplexing technique, 16:1 for FRASv1 and 32:2 for FRASv2, into a fast analogue to digital converter(s) (ADC). The attraction with this design is the possibility of making a small cost-effective instrument. However with multiple ADCs now available, for example the LTC2324-16 from Analog Devices [60] which has 4 independent 16 bit 2Msps (2×10^6 samples/s) ADCs on a single integrated circuit package, a non-multiplexed approach would probably now not be the preferred option for most applications.

8.5 Improved 32 channel fast RAS version 3 (FRASv3)

In terms of accuracy dynamic range, stability and digitisation noise the FRASv3 instrument was superior to FRASv1 and FRASv2. Although it was more expensive this was principally due to the use of general-purpose data acquisition cards in a standard electronics crate. A commercial unit that was custom-build would have a low unit price after development costs. The combination of suitable software and hardware is vital for a high specification instrument, something that FRASv1 and FRASv2 lacked. Whilst compiled computer languages such as C, C++ Java etc can

do this just as well as National Instruments (NI) LabView, LabView is an off-the-shelf solution specifically optimized for this role.

Combining this instrument with better exponential fitting of switching data gave detailed spectra in intervals down to 10 ms. Figure 7.20 demonstrates the quality and speed that is achievable.

8.6 Combined rotation and Fast ADRAS

A further natural development from this study is to operate a fast rotating sample combined with a fast RAS instrument, such a fast ADRAS instrument may prove useful in detecting the change in orientation of dipoles before the anisotropy is swamped by large changes caused by the movement of surface atoms. The study of conformational change in macromolecules could be one area of study.

By using a stepper motor the sample could be rotated under computer control, allowing if necessary averaging over multiple rotations. The system would need to be setup carefully to avoid the reflected signal précing, and thus not staying stationary on the detector. However given that a small amount of précing would produce only a rotation waveform component of 1θ , this could be filtered out. The speed at which these changes could be followed would depend on the sample rotation that could be reached. Based on the data used in this study a rotation period of 100 ms would seem realistic, so that full ADRAS data could be achievable at a 20 Hz rate (ADRAS data has a 2θ rotational symmetry).

8.7 Future work - CD instrument

The components of a RAS instrument are similar to a circular dichroism instrument (CD) [61], except CD is carried out in transmission through a material, usually liquid. This led to a design by P. Harrison and T. Farrell being submitted for a patent by the University of Liverpool [62], and remains an active area of research and is currently being funded by a BBSRC Pathfinder Award [63]

A simplified diagram is shown in Figure 8.1 of the main optical components of a CD instrument. As can be seen it comprises of the same basic components as a RAS

instrument, but for CD the components are set out in a line with the light passing through the sample in transmission.

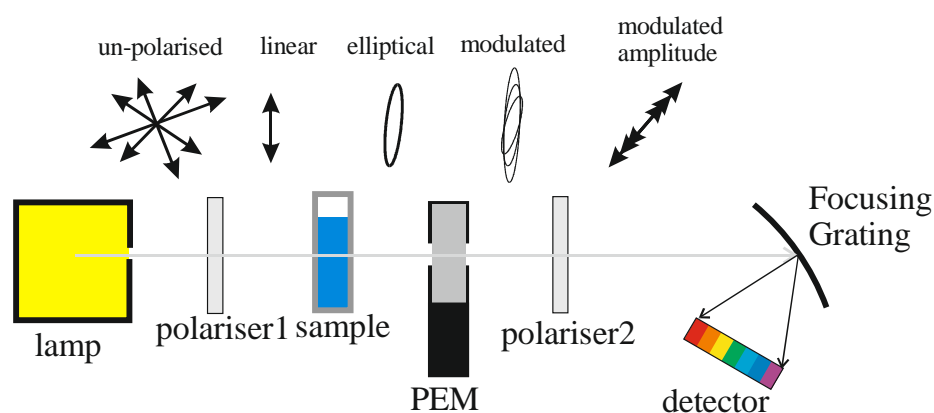


Figure 8.1 Illustration of the components used in a CD instrument

CD uses circular-polarised light rather than the linear-polarised light used in RAS. Circular polarised light has two components; right-handed and left-handed circularly polarised. A CD spectrum shows the difference between these two types with respect to wavelength. Biological systems and relevant chemicals are often made up with molecules that absorb one of these types more than the other. A CD spectrum of light that has passed through a sample can give vital information on its molecular composition.

Generally responses in CD are much slower than surface reactions, as molecules have to move around to react. However one possible application for a fast CD instrument is in the drugs industry where millions of samples have to be screened. A fast CD instrument would be capable of doing this screening orders of magnitude faster than a conventional CD instrument.

8.7.1 Calibration

In normal CD instruments there are standard compounds [64] that can be used to calibrate for both wavelength and ellipticity (mdeg). 1S-(+)-10-camphorsulphonic acid (CSA) was chosen, as it is the industry standard. A 0.6mg/ml of CSA gives an ellipticity of +202 mdeg at 290.5 nm and -420 mdeg at 192.5 nm with the ratio of the absolute signals at 192.5 nm and 290.5 nm being 2.05 or greater.

To see the second peak (at 192.5 nm) in the CSA spectra, a ten times dilution of the CSA solutions were prepared. An examination of Figure 8.2b suggests a possibility that there is a peak at the lower energy of the spectrum however, due to the lack of light below 200 nm it is not possible to make out the peak completely at 190 nm and it is definitely not the correct intensity.

Work is currently being done to develop the instrument to extend the spectral range further into the UV.

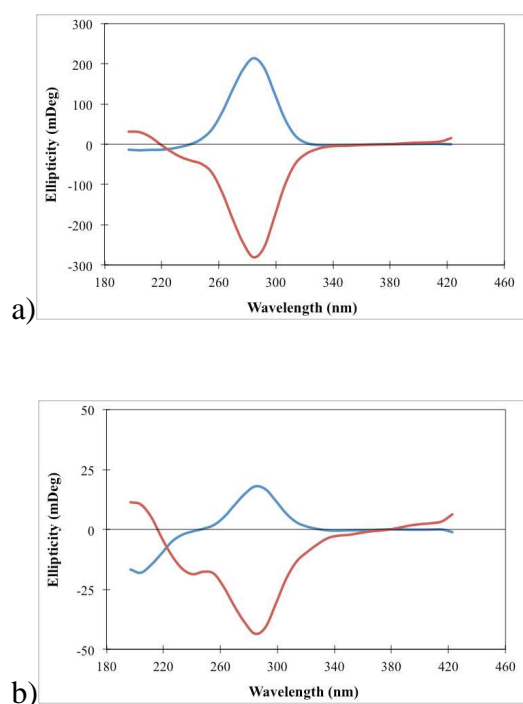


Figure 8.2a CD spectra of (blue) 0.57 mg/ml of 1S-(+)-10-camphorsulphonic acid and (red) 0.7 mg/ml of 1R-(+)-10-camphorsulphonic acid. **Figure 8.2b** CD spectra of (blue) 0.057 mg/ml of 1S-(+)-10-camphorsulphonic acid and (red) 0.2 mg/ml of 1R-(+)-10-camphorsulphonic acid.

Publications by the author

Involving work directly or indirectly related to the work on this thesis

- [1] C. I. Smith, P. Harrison, C. A. Lucas, Y. Grunder, S. D. Barrett, and P. Weightman, 'The stability of the Au(1 1 0)-(1 × 3) surface reconstruction in electrochemical environments', *J. Phys. Condens. Matter*, vol. 28, no. 1, p. 015005, Jan. 2016.
- [2] P. Harrison, C. I. Smith, Y. Grunder, C. A. Lucas, S. D. Barrett, and P. Weightman, 'Anion replacement at Au(110)/electrolyte interfaces', *Phys. Chem. Chem. Phys.*, vol. 18, no. 35, pp. 24396–24400, 2016.
- [3] P. Weightman, P. Harrison, C. A. Lucas, Y. Grunder, and C. I. Smith, 'The reflection anisotropy spectroscopy of the Au(1 1 0) surface structures in liquid environments', *J. Phys. Condens. Matter*, vol. 27, no. 47, p. 475005, Dec. 2015.
- [4] C. I. Smith, J. H. Convery, P. Harrison, B. Khara, N. S. Scrutton, and P. Weightman, 'Conformational change in cytochrome P450 reductase adsorbed at a Au(110)—phosphate buffer interface induced by interaction with nicotinamide adenine dinucleotide phosphate', *Phys. Rev. E*, vol. 90, no. 2, Aug. 2014.
- [5] P. Weightman, C. I. Smith, J. H. Convery, P. Harrison, B. Khara, and N. S. Scrutton, 'Conformational change induced by electron transfer in a monolayer of cytochrome P450 reductase adsorbed at the Au(110)—phosphate buffer interface', *Phys. Rev. E*, vol. 88, no. 3, Sep. 2013.
- [6] C. I. Smith, P. Harrison, T. Farrell, and P. Weightman, 'The nature and stability of the Au(110)/electrochemical interface produced by flame annealing', *J. Phys. Condens. Matter*, vol. 24, no. 48, p. 482002, Dec. 2012.
- [7] J. H. Convery *et al.*, 'Controlling the formation of a monolayer of cytochrome P450 reductase onto Au surfaces', *Phys. Rev. E*, vol. 86, no. 1, Jul. 2012.
- [8] P. Harrison and T. Farrell, 'Dichroism measurement device', GB201118080D0, 20-Oct-2011.
- [9] C. I. Smith *et al.*, 'Detection of DNA hybridisation on a functionalised diamond surface using reflection anisotropy spectroscopy', *EPL Europhys. Lett.*, vol. 85, no. 1, p. 18006, Jan. 2009.
- [10] C. P. Mansley, T. Farrell, C. I. Smith, P. Harrison, A. Bowfield, and P. Weightman, 'A new UV reflection anisotropy spectrometer and its application to the Au(1 1 0)/electrolyte surface', *J. Phys. Appl. Phys.*, vol. 42, no. 11, p. 115303, Jun. 2009.

- [11] T. Farrell, P. Harrison, C. I. Smith, D. S. Martin, and P. Weightman, 'Azimuthal dependent reflection anisotropy spectroscopy of Ag(110) near the plasmon resonance energy', *Appl. Phys. Lett.*, vol. 93, no. 19, p. 191102, Nov. 2008.
- [12] P. Harrison, T. Farrell, A. Maunder, C. I. Smith, and P. Weightman, 'A rapid reflectance anisotropy spectrometer', *Meas. Sci. Technol.*, vol. 12, no. 12, pp. 2185–2191, Dec. 2001.

References

- [1] J. R. Ferraro, K. Nakamoto, and C. W. Brown, *Introductory Raman spectroscopy*. Amsterdam; Boston: Academic Press, 2003.
- [2] R. M. A. Azzam and N. M. Bashara, *Ellipsometry and polarized light*. North-Holland, 1987.
- [3] Schasfoort, R. B. M., *Handbook of Surface Plasmon Resonance*. 2017.
- [4] P. Weightman, D. S. Martin, R. J. Cole, and T. Farrell, 'Reflection anisotropy spectroscopy', *Rep. Prog. Phys.*, vol. 68, no. 6, pp. 1251–1341, Jun. 2005.
- [5] P. Weightman, C. I. Smith, D. S. Martin, C. A. Lucas, R. J. Nichols, and S. D. Barrett, 'Comment on "Monitoring the Transitions of the Charge-Induced Reconstruction of Au(110) by Reflection Anisotropy Spectroscopy"', *Phys. Rev. Lett.*, vol. 92, no. 19, May 2004.
- [6] A. Ichimiya and P. I. Cohen, *Reflection High-Energy Electron Diffraction*. Cambridge University Press, 2004.
- [7] 'How Metal Organic Chemical Vapor Phase Deposition (MOCVD) Works', *AZoM.com*, 28-Nov-2014. [Online]. Available: <https://www.azom.com/article.aspx?ArticleID=11585>. [Accessed: 11-Sep-2018].
- [8] 'Chemical Vapour Deposition (CVD) - An Introduction', *AZoM.com*, 31-Jul-2002. [Online]. Available: <https://www.azom.com/article.aspx?ArticleID=1552>. [Accessed: 11-Sep-2018].
- [9] V. Mazine, Y. Borensztein, L. Cagnon, and P. Allongue, 'Optical Reflectance Anisotropy Spectroscopy of the Au(110) Surface in Electrochemical Environment', *Phys. Status Solidi A*, vol. 175, no. 1, pp. 311–316, Sep. 1999.
- [10] B. Sheridan *et al.*, 'Reflection Anisotropy Spectroscopy: A New Probe for the Solid-Liquid Interface', *Phys. Rev. Lett.*, vol. 85, no. 21, pp. 4618–4621, Nov. 2000.
- [11] V. Mazine and Y. Borensztein, 'Monitoring the Transitions of the Charge-Induced Reconstruction of Au(110) by Reflectance Anisotropy Spectroscopy', *Phys. Rev. Lett.*, vol. 88, no. 14, Mar. 2002.
- [12] C. I. Smith, P. Harrison, T. Farrell, and P. Weightman, 'The nature and stability of the Au(110)/electrochemical interface produced by flame annealing', *J. Phys. Condens. Matter*, vol. 24, no. 48, p. 482002, Dec. 2012.
- [13] G. E. Isted, D. S. Martin, L. Marnell, and P. Weightman, 'The preparation of smooth Au(110) and Cu(110) surfaces for biomolecular adsorption', *Surf. Sci.*, vol. 566–568, pp. 35–39, Sep. 2004.
- [14] H. L. Messiha, C. I. Smith, N. S. Scrutton, and P. Weightman, 'Evidence for protein conformational change at a Au(110)/protein interface', *EPL Europhys. Lett.*, vol. 83, no. 1, p. 18004, Jul. 2008.
- [15] P. Weightman, C. I. Smith, J. H. Convery, P. Harrison, B. Khara, and N. S. Scrutton, 'Conformational change induced by electron transfer in a monolayer of cytochrome P450 reductase adsorbed at the Au(110)–phosphate buffer interface', *Phys. Rev. E*, vol. 88, no. 3, Sep. 2013.
- [16] J. H. Convery *et al.*, 'Controlling the formation of a monolayer of cytochrome P450 reductase onto Au surfaces', *Phys. Rev. E*, vol. 86, no. 1, Jul. 2012.
- [17] C. Smith, J. H. Convery, B. Khara, N. Scrutton, and P. Weightman, 'The influence of the structure of the Au(110) surface on the ordering of a monolayer

- of cytochrome P450 reductase at the Au(110)/phosphate buffer interface', *Phys. Status Solidi B*, vol. 251, Mar. 2014.
- [18] C. Smith, J. H. Convery, B. Khara, N. Scrutton, and P. Weightman, 'Ordered multilayers of cytochrome P450 reductase adsorbed at Au(110)/phosphate buffer interfaces', *Phys. Status Solidi B*, vol. 252, Aug. 2014.
- [19] C. Smith, J. H. Convery, P. Harrison, B. Khara, N. Scrutton, and P. Weightman, 'Conformational change in cytochrome P450 reductase adsorbed at a Au(110) - Phosphate buffer interface induced by interaction with nicotinamide adenine dinucleotide phosphate', *Phys. Rev. E Stat. Nonlin. Soft Matter Phys.*, vol. 90, p. 022708, Aug. 2014.
- [20] V. L. Berkovits and D. Paget, 'Reflectance anisotropy spectroscopy: a new method for semiconductor surface chemistry investigation', *Thin Solid Films*, vol. 233, no. 1–2, pp. 9–13, Oct. 1993.
- [21] D. E. Aspnes, 'Above-bandgap optical anisotropies in cubic semiconductors: A visible–near ultraviolet probe of surfaces', *J. Vac. Sci. Technol. B Microelectron. Nanometer Struct.*, vol. 3, no. 5, p. 1498, Sep. 1985.
- [22] E. Hecht, *Optics*, 5 edition. Boston: Pearson, 2015.
- [23] D. E. Aspnes, 'Above-bandgap optical anisotropies in cubic semiconductors: A visible–near ultraviolet probe of surfaces', *J. Vac. Sci. Technol. B Microelectron. Nanometer Struct.*, vol. 3, no. 5, p. 1498, Sep. 1985.
- [24] D. E. Aspnes, J. P. Harbison, A. A. Studna, and L. T. Florez, 'Reflectance - difference spectroscopy system for real - time measurements of crystal growth', *Appl. Phys. Lett.*, vol. 52, no. 12, pp. 957–959, Mar. 1988.
- [25] D. E. Aspnes, J. P. Harbison, A. A. Studna, and L. T. Florez, 'Application of reflectance difference spectroscopy to molecular - beam epitaxy growth of GaAs and AlAs', *J. Vac. Sci. Technol. Vac. Surf. Films*, vol. 6, no. 3, pp. 1327–1332, May 1988.
- [26] Hamamatsu Photonics, 'Xenon & mercury-xenon lamps | Hamamatsu Photonics'. [Online]. Available: https://www.hamamatsu.com/eu/en/product/light-and-radiation-sources/lamp/xenon-lamp_mercury-xenon-lamp/index.html. [Accessed: 25-Aug-2018].
- [27] P. Weightman, D. S. Martin, R. J. Cole, and T. Farrell, 'Reflection anisotropy spectroscopy', *Rep. Prog. Phys.*, vol. 68, no. 6, pp. 1251–1341, Jun. 2005.
- [28] Hinds Instruments, 'PEM-100 Controller – Hinds Instruments'. [Online]. Available: <https://www.hindsinstruments.com/products/photoelastic-modulators/pem-100-controller/>. [Accessed: 25-Aug-2018].
- [29] 'Scientific - HORIBA'. [Online]. Available: https://www.horiba.com/en_en/products/by-segment/scientific/. [Accessed: 08-Feb-2019].
- [30] Hamamatsu Photonics, 'Photomultiplier tubes (PMTs)', 24-Aug-2018. [Online]. Available: <https://www.hamamatsu.com/eu/en/product/optical-sensors/pmt/index.html>. [Accessed: 24-Aug-2018].
- [31] Hamamatsu Photonics, 'Wide dynamic range PMT', 24-Aug-2018. [Online]. Available: https://www.hamamatsu.com/eu/en/product/type/H13126_C12918%20series/index.html. [Accessed: 24-Aug-2018].
- [32] Hinds Instruments, 'PEM Technical Overview– Hinds Instruments'. [Online]. Available: <https://www.hindsinstruments.com/products/photoelastic-modulators/pem-100-controller/>. [Accessed: 06-Feb-2018].

- [33] Ametek Scientific Instruments, '5210 Dual Phase Analog Lock-in Amplifier | Signal Recovery'. [Online]. Available: <https://www.ameteksi.com/products/lock-in-amplifiers/5210-dual-phase-analog-lock-in-amplifier>. [Accessed: 25-Aug-2018].
- [34] D. E. Aspnes, J. P. Harbison, A. A. Studna, and L. T. Florez, 'Reflectance - difference spectroscopy system for real - time measurements of crystal growth', *Appl. Phys. Lett.*, vol. 52, no. 12, pp. 957–959, Mar. 1988.
- [35] B. F. Macdonald, J. S. Law, and R. J. Cole, 'Azimuth-dependent reflection anisotropy spectroscopy', *J. Appl. Phys.*, vol. 93, no. 6, pp. 3320–3327, Mar. 2003.
- [36] B. F. Macdonald and R. J. Cole, 'Separation of optical anisotropies by angular dependent reflection anisotropy spectroscopy', *Appl. Phys. Lett.*, vol. 80, no. 19, pp. 3527–3529, May 2002.
- [37] I. U. of P. and A. Chemistry, 'IUPAC Gold Book - Beer–Lambert law (or Beer–Lambert–Bouguer law)'. [Online]. Available: <http://goldbook.iupac.org/html/B/B00626.html>. [Accessed: 04-Jun-2018].
- [38] P. B. Johnson and R. W. Christy, 'Optical Constants of the Noble Metals', *Phys. Rev. B*, vol. 6, no. 12, pp. 4370–4379, Dec. 1972.
- [39] I. A. Stegun and P. M. Morse, *Handbook of Mathematical Functions with Formulas, Graphs, and Mathematical Tables*, Corrected edition; Corrected edition. National Bureau of Standards, 1964.
- [40] Dennis Ritchie and Brian Kernighan, *The C Programming Language (2nd ed.)*. 1988.
- [41] 'Lock-in Amplifiers', *Zurich Instruments*, 27-Apr-2017. [Online]. Available: <https://www.zhinst.com/products/lock-in-amplifiers>. [Accessed: 01-Sep-2018].
- [42] National Instruments, 'What is LabVIEW? - National Instruments', *What is LabView?* [Online]. Available: <http://www.ni.com/en-gb/shop/labview.html>. [Accessed: 10-Aug-2018].
- [43] 'IEEE Standard for Floating-Point Arithmetic', *IEEE Std 754-2008*, pp. 1–70, Aug. 2008.
- [44] T. Farrell, P. Harrison, C. I. Smith, D. S. Martin, and P. Weightman, 'Azimuthal dependent reflection anisotropy spectroscopy of Ag(110) near the plasmon resonance energy', *Appl. Phys. Lett.*, vol. 93, no. 19, p. 191102, Nov. 2008.
- [45] P. Weightman, P. Harrison, C. A. Lucas, Y. Grunder, and C. I. Smith, 'The reflection anisotropy spectroscopy of the Au(1 1 0) surface structures in liquid environments', *J. Phys. Condens. Matter*, vol. 27, no. 47, p. 475005, Dec. 2015.
- [46] D. S. Martin *et al.*, 'Optical reflectance anisotropy of Ag(110): Evidence for contributions from surface-modified bulk band transitions', *Phys. Rev. B*, vol. 76, no. 11, Sep. 2007.
- [47] C. I. Smith, A. Bowfield, N. J. Almond, C. P. Mansley, J. H. Convery, and P. Weightman, 'Spectral signatures of the surface reconstructions of Au(110)/electrolyte interfaces', *J. Phys. Condens. Matter*, vol. 22, no. 39, p. 392001, Oct. 2010.
- [48] O. Núñez-Olvera *et al.*, 'A rapid reflectance-difference spectrometer for real-time semiconductor growth monitoring with sub-second time resolution', *Rev. Sci. Instrum.*, vol. 83, no. 10, p. 103109, Oct. 2012.
- [49] C. Kaspari, M. Pristovsek, and W. Richter, 'A fast reflectance anisotropy spectrometer for in situ growth monitoring', *Phys. Status Solidi B*, vol. 242, no. 13, pp. 2561–2569, Nov. 2005.

- [50] Signal Recovery, '7210 Multichannel Lock-in Amplifier', <https://www.ameteki.com/products/lock-in-amplifiers/7210-multichannel-lock-in-amplifier>, 09-Aug-2018. [Online]. Available: <https://www.ameteki.com/products/lock-in-amplifiers/7210-multichannel-lock-in-amplifier>. [Accessed: 09-Aug-2018].
- [51] C. G. Hu *et al.*, 'A rotating-compensator based reflectance difference spectrometer for fast spectroscopic measurements', *Rev. Sci. Instrum.*, vol. 81, no. 4, p. 043108, Apr. 2010.
- [52] P. Harrison, T. Farrell, A. Maunder, C. I. Smith, and P. Weightman, 'A rapid reflectance anisotropy spectrometer', *Meas. Sci. Technol.*, vol. 12, no. 12, pp. 2185–2191, Dec. 2001.
- [53] Texas Instruments, 'CD74HC4067 data sheet', <http://www.ti.com/product/CD74HC4067/technicaldocuments>, 09-Aug-2018. [Online]. Available: <http://www.ti.com/product/CD74HC4067/technicaldocuments>. [Accessed: 09-Aug-2018].
- [54] N K Sinha, 'Normalised dispersion of birefringence of quartz and stress optical coefficient of fused silica and plate glass', *Phys. Chem. Glas.*, vol. 19, no. 4, pp. 69–71, Aug. 1978.
- [55] C. G. Hu *et al.*, 'Retardation correction for photoelastic modulator-based multichannel reflectance difference spectroscopy', *J. Opt. Soc. Am. -Opt. Image Sci. Vis.*, vol. 25, no. 6, pp. 1240–1245, Jun. 2008.
- [56] Hamamatsu Photonics K.K., 'S4114-35Q data sheet', https://www.hamamatsu.com/resources/pdf/ssd/s4111-16r_etc_kmpd1002e.pdf, 09-Aug-2018. .
- [57] National Instruments, 'PXI Systems - National Instruments', *PXI Systems*. [Online]. Available: <http://www.ni.com/en-gb/shop/pxi.html>. [Accessed: 10-Aug-2018].
- [58] P. Harrison, C. I. Smith, Y. Gründer, C. A. Lucas, S. D. Barrett, and P. Weightman, 'Anion replacement at Au(110)/electrolyte interfaces', *Phys. Chem. Chem. Phys.*, vol. 18, no. 35, pp. 24396–24400, 2016.
- [59] P. D. Lane, G. E. Isted, D. S. Roseburgh, and R. J. Cole, 'Azimuth dependent reflection anisotropy of oriented thin films', *Appl. Phys. Lett.*, vol. 95, no. 14, p. 141907, Oct. 2009.
- [60] 'LTC2324-16 Datasheet and Product Info | Analog Devices'. [Online]. Available: <http://www.analog.com/en/products/ltc2324-16.html>. [Accessed: 05-Sep-2018].
- [61] A. F. Drake, 'Polarisation modulation-the measurement of linear and circular dichroism', *J. Phys. [E]*, vol. 19, no. 3, p. 170, 1986.
- [62] P. Harrison and T. Farrell, 'Dichroism measurement device', GB201118080D0, 20-Oct-2011.
- [63] 'Follow-on Funding Pathfinder'. [Online]. Available: <https://bbsrc.ukri.org/innovation/maximising-impact/follow-on-pathfinder/>. [Accessed: 10-Sep-2018].
- [64] S. M. Kelly, T. J. Jess, and N. C. Price, 'How to study proteins by circular dichroism', *Biochim. Biophys. Acta BBA - Proteins Proteomics*, vol. 1751, no. 2, pp. 119–139, Aug. 2005.